Measurement of the Two-Photon Exchange Contribution to Lepton-Proton Scattering with OLYMPUS

by

Lauren Ice

A Dissertation Presented in Partial Fulfillment
of the Requirements for the Degree
Doctor of Philosophy

Approved November 2016 by the
Graduate Supervisory Committee:

Ricardo Alarcón, Chair
Michael Dugger
Richard Lebed
Barry Ritchie

ARIZONA STATE UNIVERSITY

December 2016

ABSTRACT

The OLYMPUS experiment measured the two-photon exchange contribution to elastic electron-proton scattering, over a range of four-momentum transfer from $0.6 < Q^2 < 2.2$ (GeV/c)^2. The motivation for the experiment stemmed from measurements of the electric-to-magnetic form factor ratio of the proton $\mu G_E/G_M$ extracted from polarization observables in polarized electron-proton scattering. Polarized electron-proton scattering experiments have revealed a significant decrease in $\mu G_E/G_M$ at large Q^2, in contrast to previous measurements from unpolarized electron-proton scattering. The commonly accepted hypothesis is that the discrepancy in the form factor ratio is due to neglected higher-order terms in the elastic electron-proton scattering cross section, in particular the two-photon exchange amplitude. The goal of OLYMPUS was to measure the two-photon exchange contribution by measuring the positron-proton to electron-proton elastic scattering cross section ratio, $\sigma_{e^+p}/\sigma_{e^-p}$. The two-photon exchange contribution is correlated to the deviation of the cross section ratio from unity.

In 2012, the OLYMPUS experiment collected over 4 fb^{-1} of e^+p and e^-p scattering data using electron and positron beams incident on a hydrogen gas target. The scattered leptons and protons were measured exclusively with a large acceptance spectrometer. OLYMPUS observed a slight rise in $\sigma_{e^+p}/\sigma_{e^-p}$ of at most 1-2% over a Q^2 range of $0.6 < Q^2 < 2.2$ (GeV/c)^2. This work discusses the motivations, experiment, analysis method, and the preliminary results for the cross section ratio as measured by OLYMPUS.

To my parents:

For always encouraging me to be curious about the universe.

ACKNOWLEDGMENTS

I have sincere gratitude for my graduate advisor Professor Ricardo Alarcón for his continuous support, guidance, and patience. He provided numerous opportunities for me to learn and grow as a scientist and has always been encouraging and supportive. I would also like to thank my committee members – Professor Richard Lebed, Professor Barry Ritchie, and Dr Michael Dugger – for all their support throughout my graduate school career as well as their careful revision of, and insightful comments on this document.

I would like to acknowledge the entire OLYMPUS collaboration. The goal of this experiment was achieved with the tireless efforts of over 70 people, including scientists, engineers, technicians, accelerator staff, and students. Their hard work made this experiment possible and I have learned so much from my collaborators.

I would like to thank Professor Richard Milner, Professor Robert Redwine, Dr Douglas Hasell, and Dr Jan Bernauer for their guidance helping to direct my research and providing me the opportunity to learn from their expertise. I would also like to thank them for the numerous invitations and support for my trips to Cambridge.

I am immensely grateful to the other graduate students on the OLYMPUS experiment – Rebecca Russell, Axel Schmidt, Brian Henderson, and Colton O'Connor – for their friendship and support through every step of the experiment. They were wonderful to work with and so much of what have learned in graduate school can be attributed to them. I think fondly of the times spent in Germany building the detector and taking data, and all of the times they made me feel welcome at MIT.

There are so many people who supported and encouraged me at ASU throughout graduate school. I would like to thank my labmates at ASU for being an audience for my ideas and providing advice during our meetings. I would like to thank my classmates and close friends who have provided encouragement and some much needed

breaks from research over the years.

I am extremely grateful to my parents Peggy and Larry, and to my sister Jessica for their unwavering support and love over the years. My family has always encouraged me to be curious about the natural world and provided moral support so that I could continue my education. The past several years of my graduate education, I have had the support and love of my partner, Owen. He has taken care of me when I was stressed or worried, was a sounding board for my ideas, and was a continuous source of encouragement.

Last, I would like to thank the funding agencies which have allowed me to pursue and achieve this degree: The National Science Foundation (award 1306547) and the Science Foundation Arizona Graduate Research Fellowship.

TABLE OF CONTENTS

Page

LIST OF TABLES viii

LIST OF FIGURES ix

CHAPTER

1 INTRODUCTION 1

2 THEORETICAL FOUNDATIONS 4

2.1 Form Factors from Elastic Electron-Proton Scattering 5

2.1.1 Unpolarized Cross Section Data 9

2.1.2 Polarization Measurements 12

2.1.3 Form Factor Data from Polarization Measurements 14

2.2 Form Factor Discrepancy and Higher-Order Contributions 15

2.2.1 Measuring the Hard Two-Photon Contribution 19

3 EXPERIMENTAL SETUP 23

3.0.1 OLYMPUS Coordinate System 24

3.1 Lepton Accelerator 25

3.2 Hydrogen Target 26

3.2.1 Target Cell 27

3.2.2 Collimator and Wakefield Suppressors 29

3.2.3 Scattering Chamber 29

3.3 The OLYMPUS Spectrometer 29

3.3.1 Magnet 30

3.3.2 Drift Chambers 33

3.3.3 Time-of-Flight Scintillators 35

3.4 Luminosity Monitors 37

3.4.1 The 12° Telescopes 38

CHAPTER Page

3.4.2 Møller and Bhabha Calorimeters 40
3.5 Event Trigger 41
3.6 Running 42
4 PRELIMINARY DETECTOR ANALYSIS 44
4.1 Time-of-Flight Detectors 44
4.1.1 Mean-Time Delays 46
4.1.2 Position Offsets 48
4.1.3 Speed of Light in the Scintillator 52
4.1.4 Energy Deposition 53
4.1.5 Pedestal Offsets, Gains, and Thresholds 55
4.1.6 Attenuation Length 57
4.2 Drift Chambers 58
4.2.1 Drift Chamber Timing Calibration 59
4.2.2 Time-to-Distance Calibration 61
4.3 Track Reconstruction 63
4.3.1 The Fast Track Algorithm 65
4.3.2 Pattern Matching 67
4.3.3 Elastic Arms Algorithm 69
4.4 Luminosity Analysis 77
4.4.1 Slow-Control Luminosity Estimate 79
4.4.2 12° Luminosity Telescopes 80
4.4.3 Symmetric Møller and Bhabha Calorimeters 83
5 ANALYSIS 91
5.1 Monte Carlo Simulations 92

CHAPTER Page

5.1.1 Radiative Corrections 94
5.1.2 Propagation 100
5.1.3 Digitization 101
5.2 Analysis for the Cross Section Ratio 107
5.2.1 Particle Identification 108
5.2.2 Event Selection 116
5.2.3 Background Subtraction 124
6 CROSS SECTION RATIO RESULTS 127
6.1 Results 127
6.2 Systematic Uncertainties 130
6.3 Discussion 135
7 CONCLUSION 136
REFERENCES 138
APPENDIX
A TABLE OF CROSS SECTION RESULTS 146

LIST OF TABLES

Table Page

4.1 Luminosity Determination Results and Uncertainty 78

6.1 Systematic Uncertainties Considered 131

A.1 Cross Section Ratio Results 147

LIST OF FIGURES

Figure		Page
2.1	Feynman Diagram for Mott Scattering	5
2.2	Feynman Diagram for Rosenbluth Scattering	7
2.3	Form Factor Ratio using the Rosenbluth Separation Technique	11
2.4	Form Factor Ratio from Polarized Electron-Proton Scattering	16
2.5	Form Factor Ratio Comparison	17
2.6	Theoretical Predictions of e^-p to e^+p Cross Section Ratio	21
2.7	The Q^2 and ϵ Reach of the Three Two-Photon Exchange Experiments	22
3.1	The OLYMPUS Coordinate System	25
3.2	The Target System for OLYMPUS	28
3.3	The OLYMPUS Spectrometer	31
3.4	A Drift Chamber Cell Diagram	34
3.5	A Photograph of the Time-of-Flight Paddles	36
3.6	A Diagram of the Luminosity Detectors	38
3.7	The Integrated Luminosity	43
4.1	Histogram used for ToF Mean-Time Calibration	47
4.2	The Difference Between TDC Channels for the Top and Bottom PMT on a ToF Bar	49
4.3	The Method for Finding the Hit Position Offset and Speed of Light in the Scintillator	50
4.4	ToF Position Calibration using reconstructed $\Delta\varphi$	51
4.5	The Scintillator Speed of Light Calibration	54
4.6	The Absolute PMT Gain Calibration	56
4.7	The TDC Distribution from a Single Wire	60
4.8	Drift Chamber Calibration	62

Figure Page

4.9 An Event Display Image of an Event 65
4.10 Pattern Matching an Event 68
4.11 ToF Weights in EAA 73
4.12 Symmetric Møller and Bhabha Event Calorimeter Histograms 84
4.13 Symmetric Møller and Bhabha Luminosity to the Slow-Control Luminosity Ratio 86
4.14 The Multi-Interaction Event Peak in the Left Master Histogram 88
5.1 Diagram for the Analysis Method 93
5.2 Feynman Diagrams of the First-Order Radiative Corrections 95
5.3 Feynman Diagrams for External Radiative Corrections of Order α^3 95
5.4 The Time-of-flight Efficiency from the Monte Carlo 104
5.5 Time-of-Flight Efficiency from SiPM Studies 105
5.6 Illustration of an Event 109
5.7 Calculated m^2 for All Particles 112
5.8 Lepton-Proton Overlap in m^2 Calculation 113
5.9 Energy Deposited in the ToF Detector Versus the Particle Momentum . 114
5.10 Comparison Distributions of the Momentum Verses the Time-of-Flight . 115
5.11 The t_0 Correlation as a Function of Q^2 118
5.12 The Vertex Position Correlation as a Function of Q^2 119
5.13 The φ Correlation as a Function of Q^2 120
5.14 The θ Correlation as a Function of Q^2 121
5.15 The Calculated Beam Energy using the Momentum of the Tracks 122
5.16 The Reconstructed Beam Energy from the Scattered Particles as a Function of Q^2 123

Figure Page

5.17 The φ Correlation for Various Reconstructed Beam Energy Cuts 124
5.18 The $\Delta\varphi$ Correlation Showing Background Event Subtraction 125
6.1 The Rates as a Function of Q^2 128
6.2 Cross Section Ratio Preliminary Results 129
6.3 The Cross Section Ratio as a Function of ϵ with Theory Curves 130
6.4 Yield in Left Sector to Yield in Right Sector for Data and Monte Carlo Simulation Data 132
6.5 The Cross Section Ratio Comparison Between the Left and Right Sectors 133
6.6 The Cross Section Ratio with Several Analysis Cuts 134

Chapter 1

INTRODUCTION

The pursuit to understand the internal structure of the proton has been ongoing since measurements of the magnetic moment of the proton by Stern *et al.* (1933) were found to be inconsistent with the magnetic moment of a point-like Dirac particle. Even today, a complete characterization and understanding of the complex structure of the proton has not been achieved, and many puzzles regarding the proton structure remain.

One of the unsolved problems regarding the proton structure is the discrepancy between measurements of the proton's electric-to-magnetic form factor ratio. The proton's electric and magnetic form factors are observables that characterize the charge and current distributions of the constituent quarks of the proton. These form factors are determined using electron-proton elastic scattering, which has long been an extremely important tool for understanding proton structure. Using a charged point particle, such as an electron, as a probe, Quantum Electrodynamics (QED) can be used to extract information about electromagnetic distributions inside the proton. Because QED can accurately describe electromagnetic phenomena to a small fraction of the size of the proton, the electron serves as an excellent tool for studying proton structure. Two methods have been used to extract these form factors: extracting the form factors from measurements of the unpolarized electron-proton scattering, and measuring polarization observables in polarized electron-proton scattering. A significant discrepancy exists in the resulting form factor measurements between the two experimental methods.

This discrepancy is thought to stem from neglected higher-order terms in the cross

section ratio, primarily the contribution of the the two-photon exchange process. In QED, interactions are propagated by virtual photons that couple to the electromagnetic currents of electrically charged particles. The coupling between the charged particles and the virtual photons is defined by the fine structure constant $\alpha \approx 1/137$. Because α is small, the amplitudes for QED interactions can be calculated perturbatively. In calculations of the electromagnetic form factors using electron-proton scattering, the perturbative expansion of the scattering amplitude was truncated after the one-photon exchange amplitude and the first-order radiative corrections. The next order, or hard two-photon exchange amplitude, is significantly reduced because of the factor of α^2 in the amplitude and was assumed to be negligible. However, the hard two-photon exchange amplitude cannot be calculated directly with QED and is dependent on the proton's internal structure. An experimental measurement of the two-photon exchange amplitude would provide the information necessary to determine whether the form factor measurement discrepancy is a result of neglected higher-order terms.

The two-photon exchange contribution to electron-proton scattering can be determined by comparing the measured cross section for elastic electron-proton scattering to the cross section for positron-proton scattering. In the cross section calculation for lepton-proton scattering there exists an interference term between the one- and two-photon exchange amplitudes which is proportional to the charge of the lepton cubed. This interference term is proportional to α^3 and is therefore accessible with a precision measurment comparing the electron-proton and positron-proton scattering cross sections.

As a method to determine the two-photon exchange contribution to electron-proton scattering, OLYMPUS measured the positron-proton to electron-proton elastic scattering cross section ratio over a four-momentum transfer squared range from

$0.6 < Q^2 < 2.2$ $(\mathrm{GeV/c})^2$. The data for the cross section ratio were taken during 2012 on the electron and positron storage ring, DORIS III, at DESY Laboratory in Hamburg, Germany. The lepton beams were incident on a hydrogen gas target and the cross section ratio was measured with the OLYMPUS detector system. The analysis to extract the cross section ratio involved a sophisticated track reconstruction algorithm. A Monte Carlo simulation was used to understand the acceptance function of the detector and to include the effect of radiative corrections on the cross section ratio. This thesis will discuss the motivations, the experimental method and the preliminary results of the OLYMPUS experiment.

Chapter 2

THEORETICAL FOUNDATIONS

The electromagnetic form factors are central to an understanding of nucleon structure and characterize the electromagnetic distributions within a nucleon. In the one-photon exchange limit (also called the Born approximation) the form factors describe the deviation of the charge and magnetic moment distributions for the nucleon from those for a structureless spin-1/2 Dirac particle. The form factors are crucial in understanding nucleon and hadronic structure, nucleon-nucleon interactions, and Quantum Chromodynamics (QCD) in the non-perturbative region.

The proton form factors, historically, were inferred from unpolarized elastic electron-proton scattering cross section measurements. Advances in producing and stabilizing highly polarized lepton beams, polarized targets, and polarimetry in the 1990s allowed for the form factors to be extracted from polarization observables, via polarized elastic electron-proton scattering. However, these two methods produced different results for the proton form factors, with the discrepancy growing at large four-momentum transfer squared Q^2.

A likely cause for this discrepancy comes from a distortion in the measured proton form factors stemming from neglected higher-order terms in the electron-proton scattering cross section. The two-photon exchange amplitude cannot be fully calculated, without approximation, independent of a model for the structure of the proton. Therefore, to confirm this hypothesis, the next term in the cross section (the two-photon exchange amplitude) needs to be measured experimentally.

The amplitude for two-photon exchange in electron-proton scattering is accessible by comparing the cross sections for elastic electron-proton scattering and positron-

proton scattering as a function of four-momentum transfer squared, which the OLYMPUS experiment has done.

This chapter will first review the derivation and theoretical interpretations of the nucleon form factors, followed by a discussion of the methods by which the form factors are experimentally measured. Next, the formalism for the two-photon exchange amplitude is presented and the ability for that contribution to resolve the form factor discrepancy is discussed. Last, the measurement of the cross section ratio, and results from previous measurements of this observable, will be presented.

2.1 Form Factors from Elastic Electron-Proton Scattering

The first-order approximation of elastic electron-proton scattering is the exchange of a single virtual photon between the electromagnetic currents produced by the electron and proton target. In the simplest form, the proton is taken to be an infinitely massive point source, which simplifies the interaction to the response of the electron to the static Coulomb potential. A diagram of an electron interacting with a Coulomb potential is shown in Figure 2.1.

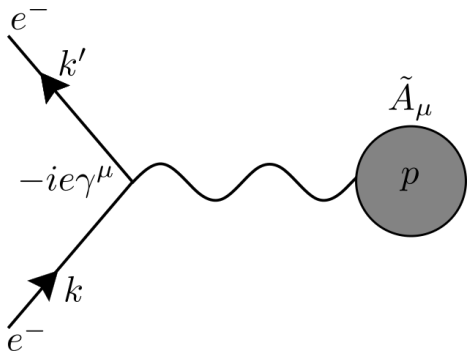

Figure 2.1: Diagram of the Coulomb interaction between an electron and an infinitely-massive point-like proton.

In Figure 2.1 the initial and final four-momentum vectors of the electron are given as $k = (E, \mathbf{k})$ and $k' = (E', \mathbf{k}')$, where E and E' are the initial and final electron

energies, and $\mathbf{k}$ and $\mathbf{k}'$ are the initial and final electron three-momentum vectors. The four-momentum transfer, carried by the virtual photon from the field to the electron, is $q = k - k'$, and $\tilde{A}_\mu(q)$ is defined as the four-dimensional Fourier transform of a static Coulomb potential. The transition current, j^ν, for the electron is

$$j^\nu = -e\bar{u}(k')\gamma^\nu u(k), \tag{2.1}$$

where $\bar{u}(k')$ and $u(k)$ are the Dirac spinors for k and k', γ^μ are the Dirac matrices, and $-e$ is the charge of the electron. The invariant scattering amplitude then can be written as

$$i\mathcal{M} = -ie\bar{u}(k')\gamma^\mu u(k)\tilde{A}_\mu(q). \tag{2.2}$$

Summing over spin states to get the spin-average amplitude of (2.1), the differential cross section for an electron interacting with a point source Coulomb potential is

$$\left(\frac{d\sigma}{d\Omega}\right)_{Mott} = \left(\frac{e^2}{2E}\right)^2 \left(\frac{\cos^2(\theta/2)}{\sin^4(\theta/2)}\right), \tag{2.3}$$

where θ is the angle by which the electron is scattered relative to its initial momentum. Equation (2.3) is known as the Mott scattering cross section, the relativistic cross section for a spin-1/2 lepton scattering from a spinless, infinitely massive, point charge proton.

In the late 1940s Rose (1948) postulated that the structure (size and shape) of the proton could be measured with lepton scattering by observing deviations from the Mott scattering cross section. Rosenbluth (1950) is credited for producing the first scattering formula to account for the effective charge and effective magnetic moment of the proton. The first step to generalize the proton vertex is to relax the spinless and point-like assumptions for the proton by taking $\gamma^\mu \to \Gamma^\mu$, where the total coupling of the electromagnetic field distributions of the proton's internal structure is present in

Γ^μ. The transition current for the proton is

$$J^\mu = e\bar{N}(p')\Gamma^\mu N(p), \tag{2.4}$$

where $\bar{N}(p')$ and $N(p)$ are the Dirac spinors for the initial and final state of the proton. This generalizes the scattering amplitude, written by (Foldy, 1952) as

$$-i\mathcal{M} = \frac{ig_{\mu\nu}}{q^2}\left[ie\bar{u}(k')\gamma^\mu u(k)\right]\left[-ie\bar{N}(p')\Gamma^\mu(p,p')N(p)\right], \tag{2.5}$$

where $-ig_{\mu\nu}/q^2$ is the photon propagator. The Feynman diagram for this scattering amplitude is represented in Figure 2.2.

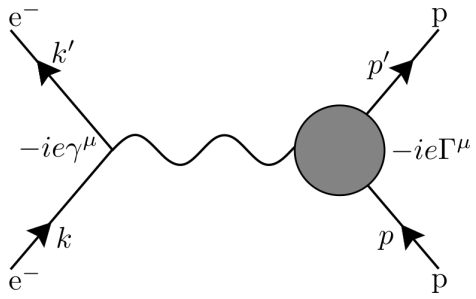

Figure 2.2: Diagram of the elastic scattering between a proton and a proton in the one-photon exchange limit.

Lorentz invariance limits Γ^μ to be a function of p^μ, p'^μ, and γ^μ, and the Ward identity, which enforces gauge symmetry, limits the structure of Γ^μ to be

$$\Gamma^\mu = A\gamma^\mu + B(p'^\mu + p^\mu), \tag{2.6}$$

where the coefficients A and B are unknown functions of Q^2. Rearranging (2.6) using the Gordon identity, and rewriting A and B as $F_1(Q^2)$, and $F_2(Q^2)$, $\Gamma^\mu(Q^2)$, may be written as

$$\Gamma^\mu(Q^2) = \gamma^\mu F_1(Q^2) + \frac{i\sigma^{\mu\nu}q_\nu}{2m}F_2(Q^2). \tag{2.7}$$

The $(p'^{\mu} + p)$ term is replaced by $\sigma^{\mu\nu} q_{\nu}$, where the tensor $\sigma^{\mu\nu} = \frac{i}{2}[\gamma^{\mu}, \gamma^{\nu}]$. $F_1(Q^2)$ and $F_2(Q^2)$ are called the proton form factors and were first introduced by Foldy (1952). Equation (2.7) splits the vertex into two parts: the deviation of the form factor from a point charge is encompassed by the Dirac form factor $F_1(Q^2)$, and the deviation from a point anomalous magnetic moment is encompassed by the Pauli form factor $F_2(Q^2)$. Substituting Equation (2.7) into Equation (2.5), the one-photon exchange cross section for elastic electron-proton scattering becomes

$$\left(\frac{d\sigma}{d\Omega}\right)_{Ros} = \left(\frac{d\sigma}{d\Omega}\right)_{Mott} \frac{E'}{E} \left\{ F_1^2(Q^2) + \tau \left[F_2^2(Q^2) + 2\left(F_1(Q^2) + F_2(Q^2)\right)^2 \tan^2\left(\frac{\theta}{2}\right) \right] \right\}, \tag{2.8}$$

where $\tau = Q^2/4m_p^2$ and m_p is the mass of the proton. The factor $\frac{E'}{E}$ comes from the recoil of the no-longer infinitely massive proton, and is equivalent to $(1+\tau)^{-1}$. While Rosenbluth (1950) originally calculated the differential cross section in terms of the effective charge and effective magnetic moment of the proton, Equation (2.8) is equivalent. This is the full equation of the spin-averaged differential cross section for elastic electron-proton scattering in the one-photon approximation, and is commonly referred to as the Rosenbluth Formula.

Linear combinations of F_1 and F_2 can be rearranged into more physically insightful forms. Yennie *et al.* (1957) and Ernst *et al.* (1960) rearranged the form factors into F_{ch} (which measures distribution of charge) and F_{mag} (which measures the distribution of magnetization). Similar to F_{ch} and F_{mag} are G_{Ep} and G_{Mp}, the Sachs form factors, which were first calculated by Hand *et al.* (1963), and are written in terms of F_1 and F_2 as

$$G_{Ep}(Q^2) = F_1(Q^2) + \tau F_2(Q^2) \tag{2.9}$$

and

$$G_{Mp}(Q^2) = F_1(Q^2) + F_2(Q^2). \tag{2.10}$$

The Rosenbluth formula, written in terms of G_{Ep} and G_{Mp} is then

$$\left(\frac{d\sigma}{d\Omega}\right)_{Rosenbluth} = \left(\frac{d\sigma}{d\Omega}\right)_{Mott} \frac{G_{Ep}^2(Q^2) + \tau/\epsilon G_{Mp}^2(Q^2)}{(1+\tau)}, \tag{2.11}$$

where ϵ is the virtual photon longitudinal polarization and is calculated as

$$\epsilon = \frac{1}{1 + 2(1+\tau)\tan^2\theta/2}. \tag{2.12}$$

There has been work, most recently by Kelly (2002), towards relating G_{Ep} and G_{Mp} to the physical distributions of the charge and magnetism in the proton; however such a relationship cannot be established in a nucleon model-independent way. Mathematically, there exists a reference frame where G_{Ep} and G_{Mp} can be related to the spatial charge and current distributions of the proton via a Fourier transform. This reference frame is called the Breit frame, and in this frame the scattered electron does not transfer energy to the proton, though the electron does transfer momentum. Within this framework, a different Breit frame exists for every value of Q^2. At the four-momentum transfer value, where the Breit frame is moving relativistic to the lab frame, it becomes impossible to convert this back into the lab frame without a model for the nucleon.

2.1.1 Unpolarized Cross Section Data

With Equation (2.11), the form factors G_{Ep} and G_{Mp} can be determined from unpolarized cross section data using a method called the Rosenbluth separation technique. With this technique, the scattering cross section is measured at several scattering angles θ and beam energies E for a fixed four-momentum transfer Q^2. Rearranging Equation (2.11), a reduced cross section can be defined that allows for the form factors to be easily extracted:

$$\left(\frac{d\sigma}{d\Omega}\right)_{Reduced} = \frac{\left(\frac{d\sigma}{d\Omega}\right)_{Rosenbluth}}{\left(\frac{d\sigma}{d\Omega}\right)_{Mott}} = \frac{{G_{Ep}}^2(Q^2) + \tau {G_{Mp}}^2(Q^2)}{1+\tau} + 2\tau G_{Mp}(Q^2)^2 \tan^2(\theta/2). \tag{2.13}$$

By linearly fitting the reduced cross section as a function of $\tan^2(\theta/2)$, $\frac{{G_{Ep}}^2(Q^2)+\tau {G_{Mp}}^2(Q^2)}{1+\tau}$ is the y-intercept and $2\tau {G_{Mp}}^2(Q^2)$ is the slope. This procedure then allows for G_{Ep} and G_{Mp} to be extracted separately.

The functional form of the form factors is determined by repeating this technique over a range of Q^2. At large Q^2, accurately extracting G_{Ep} and G_{Mp} separately becomes difficult because of uncertainties in the absolute normalization of the cross section measurement. However, the normalization factors cancel when the ratio $\frac{G_{Ep}}{G_{Mp}}$ is calculated. Because of this, the electromagnetic form factor ratio $\frac{G_{Ep}}{G_{Mp}}$ is commonly determined and published.

The first form factor data extracted were F_1 and F_2 using the ellipse technique by Hofstadter *et al.* (1953a), Hofstadter *et al.* (1953b), McAllister and Hofstadter (1956), Hofstadter (1956), Hofstadter *et al.* (1958), Bumiller *et al.* (1960), and Hofstadter *et al.* (1960). In Hand *et al.* (1963), the first G_{Ep} and G_{Mp} calculations were done using preexisting data. Since the 1950s the Sachs form factors have been extracted by many experiments. A small sample of form factor data is shown in Figure 2.3, which includes data from Janssens *et al.* (1966), Berger *et al.* (1971), Bartel *et al.* (1973), Borkowski *et al.* (1974) and more recent measurements from Andivahis *et al.* (1994), Walker *et al.* (1994), Christy *et al.* (2004), and Qattan *et al.* (2005). Other data, not shown in Figure 2.3 are Coward *et al.* (1968), Litt *et al.* (1970), Price *et al.* (1971), Hanson *et al.* (1973), JJ Murphy *et al.* (1974), Simon *et al.* (1980), and Arnold *et al.* (1986).

The Rosenbluth method reveals both G_{Ep} and G_{Mp} roughly are proportional to a dipole distribution, given by

$$G_D = \left(1 + \frac{Q^2}{m_D}\right)^{-2}, \tag{2.14}$$

where $m_D = 0.71$ was determined experimentally, (Litt *et al.*, 1970). In relation to the

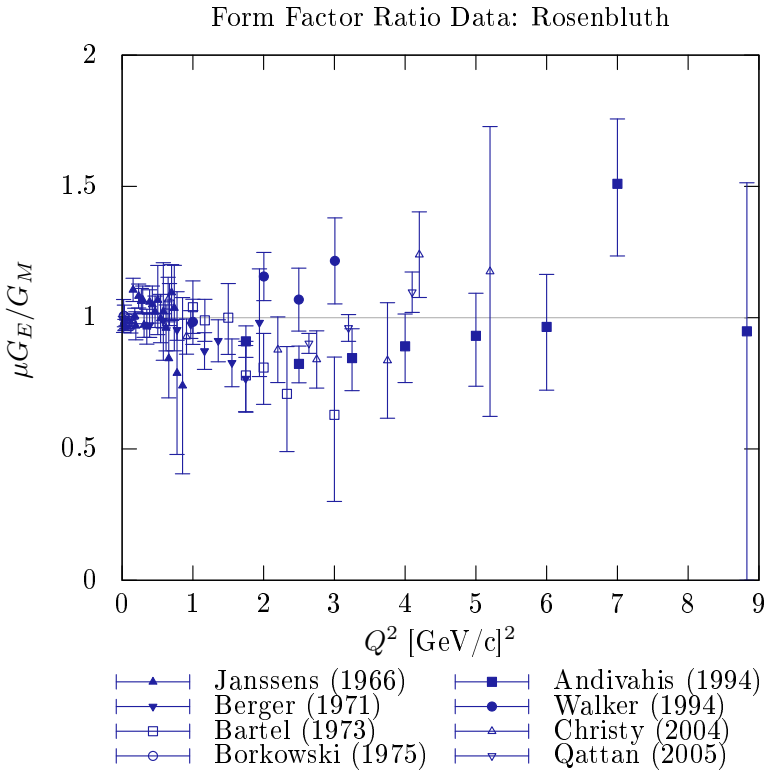

Figure 2.3: Form factor ratio, $\frac{G_{Ep}}{G_{Mp}}$, results from unpolarized electron-proton cross section as a function of Q^2. Both G_{Ep} and G_{Mp} are found to be proportional to a dipole form factor: G_D.

dipole distribution, $G_{Ep} \approx G_D$ and $G_{Mp} \approx G_D/\mu_p$, where μ_p is the magnetic moment of the proton. Modern experimental techniques, as implemented by Bosted *et al.* (1992), Sill *et al.* (1993), Walker *et al.* (1994), Andivahis *et al.* (1994), Christy *et al.* (2004), and Qattan *et al.* (2005), have allowed for the uncertainty in $\frac{G_{Ep}}{G_{Mp}}$ to decrease significantly; however at large Q^2, accurately extracting G_{Ep} remains difficult. As the four-momentum transfer increases, so does τ, reducing the size of the y-intercept and minimizing G_{Ep} contribution to the y-intercept.

2.1.2 Polarization Measurements

In the late 1990s, the advent of highly polarized lepton beams created new ways to extract proton form factor information from electron-proton scattering. The electric-to-magnetic form factor ratio of the proton can be extracted using both polarization transfer methods and by measuring the asymmetry in double-polarization experiments.

Polarization Transfer

The polarization transfer method, which is also called the recoil-proton polarization method, uses longitudinally polarized electrons scattered from an unpolarized proton target. In the one-photon-exchange approximation, the electron transfers the polarization to the recoiled proton which has only two non-zero components relative to the proton momentum in the scattering plane, P_ℓ and P_t, the parallel and the perpendicular polarization. Measuring the recoil-proton polarization lends itself to the measurement of the electromagnetic form factor ratio, since the ratio of P_t to P_ℓ is proportional to $\frac{G_{Ep}}{G_{Mp}}$.

The recoil-polarization components are functions of G_{Ep} and G_{Mp}, and are calculated by Arnold *et al.* (1981) as,

$$I_0 P_t = -2\sqrt{\tau(1+\tau)} G_{Mp} G_{Ep} \tan(\theta/2), \tag{2.15}$$

and

$$I_0 P_\ell = \frac{E+E'}{M}\sqrt{\tau(1+\tau)} {G_{Mp}}^2 \tan^2(\theta/2), \tag{2.16}$$

where I_0 is proportional to the unpolarized cross section, (2.11)

$$I_0 = {G_{Ep}}^2 + \frac{\tau}{\epsilon}{G_{Mp}}^2. \tag{2.17}$$

Combining (2.15) and (2.16), the electromagnetic form factor ratio is

$$\frac{G_{Ep}}{G_{Mp}} = -\frac{P_t}{P_\ell}\frac{(E+E')}{2M}\tan(\theta/2)\,. \tag{2.18}$$

Without separate measurements of the unpolarized cross section to recover I_0, only the ratio of G_{Ep} to G_{Mp} can be measured.

Because of the direct proportionality between $\frac{G_{Ep}}{G_{Mp}}$ and $\frac{P_t}{P_\ell}$, the form factor ratio can be extracted to better precision at large Q^2. Needing only one simultaneous measurement of P_t and P_ℓ to extract the form factor ratio at a particular four-momentum value keeps systematic uncertainties low.

Asymmetry from Polarized Lepton-Proton Scattering

The electromagnetic form factor ratio can also be obtained through measuring a beam helicity asymmetry for longitudinally-polarized electron scattered from a polarized proton target.

The polarized electron-proton elastic scattering cross section can be separated into the unpolarized cross section (2.11) and a part accounting for the polarization of the beam and target; Donnelly and Raskin (1986) and Raskin and Donnelly (1989) write this as

$$\sigma_{pol} = \Sigma + h\Delta. \tag{2.19}$$

Here Σ is the unpolarized cross section given by (2.11), h is the electron beam helicity, and Δ is the deviation from the unpolarized cross section due to the polarization. Δ is written as

$$\begin{aligned}\Delta = &-2\sigma_{Mott}\tan(\theta/2)\sqrt{\frac{\tau}{1+\tau}}\left[\tau(1+(1+\tau)\tan^2(\theta/2))\right]\\ &\times\cos(\theta^*)\,{G_{Mp}}^2 + \sin(\theta^*)\cos(\varphi^*)\,G_{Ep}G_{Mp},\end{aligned} \tag{2.20}$$

where θ^* and φ^* are the polar and azimuthal angles of the target polarization in the

laboratory frame. By switching the beam helicity, an asymmetry can be found. The physical asymmetry is

$$A_{phys} = \frac{\sigma_+ - \sigma_-}{\sigma_+ + \sigma_-} = \frac{\Delta}{\Sigma}, \tag{2.21}$$

where σ_+ and σ_- are the cross sections measured for the two beam helicities. The physical asymmetry A_{phys} relates to the measured asymmetry A_{meas} by

$$A_{meas} = P_{beam} P_{target} A_{phys}, \tag{2.22}$$

where P_{beam} and P_{target} are the beam and target polarizations. Taking $\theta^* = \pi/2$ and $\varphi^* = 0$ or π, A_{meas} reduces to

$$A_{meas} = \frac{-2\sqrt{(\tau(1+\tau))}\tan(\theta/2)\frac{G_{Ep}}{G_{Mp}}}{\left(\frac{G_{Ep}}{G_{Mp}}\right)^2 + \frac{\tau}{\epsilon}}. \tag{2.23}$$

Because G_{Ep} is much smaller than G_{Mp}, in the denominator $\left(\frac{G_{Ep}}{G_{Mp}}\right)^2 \approx 0$, $A_{meas} \propto \frac{G_{Ep}}{G_{Mp}}$.

2.1.3 Form Factor Data from Polarization Measurements

The benefits of using polarization observables to extract the proton form factors were first pointed out by Akhiezer and Rekalo (1968), Dombey (1969), and Akhiezer and Rekalo (1974), and further elaborated by Donnelly and Raskin (1986) and Arnold *et al.* (1981). Experimentally, this method was not realized until the late 1990s, when technical improvements on beam polarization abilities and stability provided sufficient luminosity for this measurement. The first group to extract the form factors using a polarization transfer technique was the MIT-Bates FPP Collaboration (Milbrath *et al.*, 1998) and (Barkhuff *et al.*, 1999), followed by the MAMI A1 Collaboration in 2001 (Pospischil *et al.*, 2001). These early measurements at

low four-momentum-transfer agreed with the Rosenbluth data. In 2000, the Hall A Collaboration at Thomas Jefferson National Accelerator Facility (Jefferson Lab) published electromagnetic form factor ratios by polarization transfer measurements with four-momentum-transfer squared from $0.5 < Q^2 < 3.5$ $(\mathrm{GeV/c})^2$ (Jones *et al.*, 2000). These data revealed a clear deviation in the form factor ratio from that found in unpolarized experiments. A new analysis of the Jefferson Lab data (Punjabi *et al.*, 2005) improved systematic uncertainties, but still showed a clear deviation from the Rosenbluth data. Jefferson Lab confirmed these findings to four-momentum-transfer squared up to 5.6 $(\mathrm{GeV/c})^2$ (Gayou *et al.*, 2002). This deviation from the Rosenbluth measurement was confirmed by Strauch *et al.* (2003), Jones *et al.* (2006), MacLachlan *et al.* (2006), Hu *et al.* (2006), and Crawford *et al.* (2007). Data after 2000 is shown in Figure 2.4.

2.2 Form Factor Discrepancy and Higher-Order Contributions

The Sachs form factor ratio, as extracted using both polarization transfer and polarization asymmetry techniques, shows a clear discrepancy with the form factors extracted with the Rosenbluth technique. A side-by-side comparison is shown in Figure 2.5, with the same data as in Figure 2.3 and Figure 2.4.

Because much of the knowledge of the structure of the nucleon stems from the form factor data, this discrepancy is cause for concern, bringing the form of G_{Ep} (and to a lesser extent, G_{Mp}) into question. In attempts to reconcile the two methods, a new analysis of the Rosenbluth data by Arrington (2003) insured a consistent analysis across the Rosenbluth form factor data and updated the radiative corrections and normalization uncertainties. Even with the new analysis, the discrepancy in the form factors persisted, even at Q^2 where the Rosenbluth yields precise results.

Guichon and Vanderhaeghen (2003) pointed out that the inconsistencies could

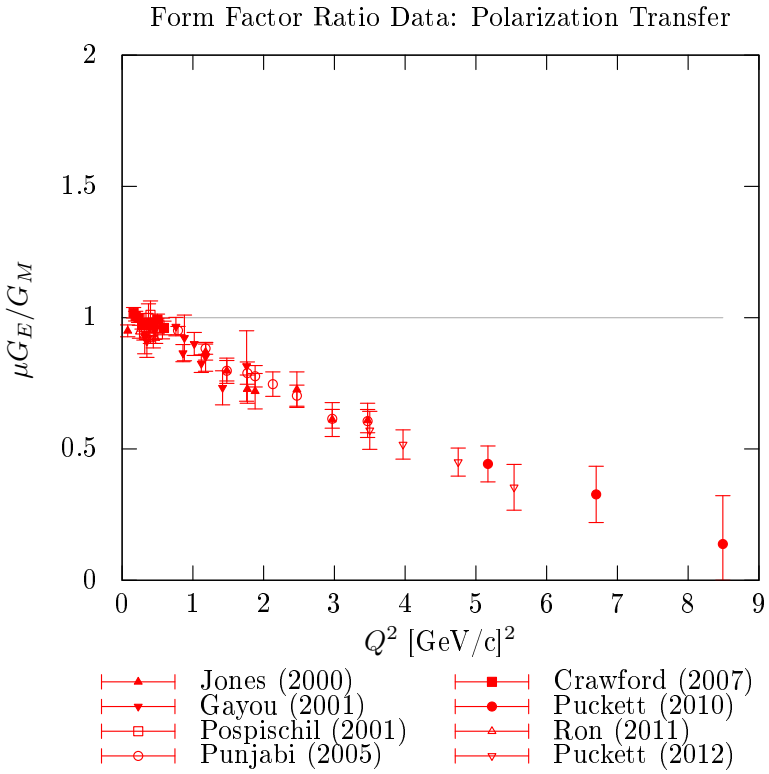

Figure 2.4: Form factor ratio $\mu_p \frac{G_{Ep}}{G_{Mp}}$ results from polarized electron-proton cross section as a function of Q^2.

be caused by neglected higher-order contributions to the elastic electron-proton scattering cross section, primarily hard two-photon exchange. Both the Rosenbluth and polarization techniques are first-order approximations, assuming only one virtual photon exchange between the electron and proton. But since the QED perturbation parameter is $\alpha \approx 1/137$, the two-photon exchange amplitude should be significantly smaller than the first-order approximation; however, this amplitude could still cause issues with the form factor extraction. The two-photon exchange contribution to the cross section affects the Rosenbluth measurements more than the polarization measurements. Because a ratio of cross sections is used to extract the form factors with the polarization techniques, the effect of the two-photon exchange amplitude largely

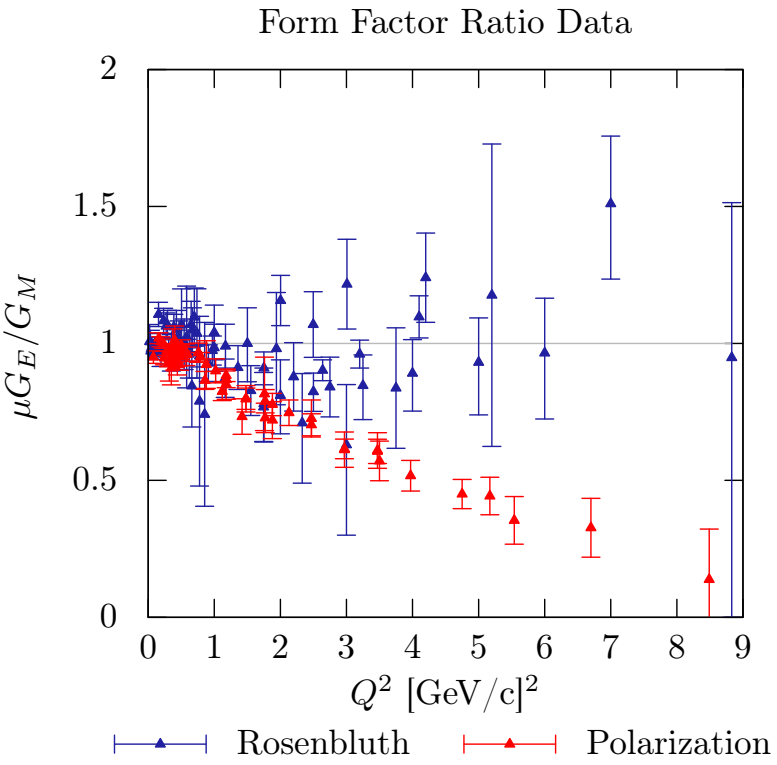

Figure 2.5: Form factor ratio, $\mu_p \frac{G_{Ep}}{G_{Mp}}$, comparing form factors extracted from Figure 2.3 (unpolarized observables) and Figure 2.4 (polarization observables).

cancels. Since the Rosenbluth technique requires cross section measurements, this cancellation does not apply. Guichon and Vanderhaeghen (2003) calculated that the two-photon exchange would affect the form factor ratio R as

$$(R_{Rosenbluth})^2 = \frac{\left|\tilde{G}_{Ep}\right|^2}{\left|\tilde{G}_{Mp}\right|^2} + 2\left(\tau + \frac{\left|\tilde{G}_{Ep}\right|}{\left|\tilde{G}_{Mp}\right|}\right) Y_{2\gamma} \tag{2.24}$$

and

$$(R_{Polarization}) = \frac{\left|\tilde{G}_{Ep}\right|}{\left|\tilde{G}_{Mp}\right|} + \left(1 - \frac{2\epsilon}{1+\epsilon}\frac{\left|\tilde{G}_{Ep}\right|}{\left|\tilde{G}_{Mp}\right|}\right) Y_{2\gamma}, \tag{2.25}$$

where $Y_{2\gamma}$ is a dimensionless parameter proportional to the size of the two-photon contribution. Equation (2.24) shows that the effect of two-photon contribution for

the Rosenbluth technique is at least as large as $2\tau Y_{2\gamma}$. Since τ is proportional to Q^2, this factor increases linearly with Q^2, and for most reasonable values of $\frac{\left|\tilde{G}_{Ep}\right|}{\left|\tilde{G}_{Mp}\right|}$, the $Y_{2\gamma}$ multiplicative value will be larger than four. For polarization techniques, $\epsilon \in (0,1)$, which limits $\frac{2\epsilon}{1+\epsilon} \in (0,1)$. For reasonable values of $\frac{\left|\tilde{G}_{Ep}\right|}{\left|\tilde{G}_{Mp}\right|}$, the two-photon multiplicative factor is small (less than 0.5) and roughly constant with Q^2. Considering this, Guichon and Vanderhaeghen (2003) postulated that with some nucleon models, the two-photon exchange amplitude could reconcile the two form factor techniques.

The standard radiative corrections applied to the form factor measurements includes the soft two-photon amplitude, but do not include the hard two-photon exchange. A soft two-photon exchange means that the amplitude is calculated by assuming that the momentum-transfer by one of the two photons exchanged between the electron and proton is zero. A full calculation of the hard two-photon exchange requires full knowledge of the structure of the proton, and therefore cannot be calculated in a model-independent way.

There are many theoretical calculations for the two-photon exchange amplitude. The results for the two-photon exchange amplitude vary significantly depending on the theoretical model used. For some of the theoretical models the two-photon exchange contribution resolves the form factor ratio discrepancy, while others do not fully reconcile the two experimental techniques. Some of the theoretical models are Blunden *et al.* (2003), Chen *et al.* (2004), Afanasev *et al.* (2005), Tomasi-Gustafsson and Gakh (2005), Blunden *et al.* (2005), Kondratyuk *et al.* (2005), Borisyuk and Kobushkin (2006), Bystritskiy *et al.* (2007), Gorchtein (2007) and Tomasi-Gustafsson *et al.* (2013) and several phenomenological models are Chen *et al.* (2007), Guttmann *et al.* (2011) and Bernauer *et al.* (2014b).

The two-photon exchange amplitude varies significantly between theories. An experimental measurement is needed to determine if the two-photon exchange amplitude

can resolve the discrepancy in the form factor ratio data.

2.2.1 Measuring the Hard Two-Photon Contribution

There are two ways to look for the two-photon exchange contribution to elastic electron-proton scattering. The first is by measuring the reduced cross section, Equation (2.13), to high precision and low ϵ. Two-photon exchange would cause deviations of the linear ϵ dependence of Equation (2.13), (Arrington, 2004). There have been several Rosenbluth experiments with large ϵ range and low uncertainties, (Borkowski *et al.*, 1974), (Andivahis *et al.*, 1994), and (Christy *et al.*, 2004). These experiments were reanalyzed by Arrington (2004) and no significant deviation from the linear trend was found. However, the paper points out, that even with the larger ϵ range, there is little data below $\epsilon = 0.4$.

Another method, first proposed by Yount and Pine (1962), uses the cross section ratio of positron-proton to electron-proton elastic scattering to determine the size of the two-photon exchange amplitude. Under the one-photon exchange assumption, the lepton-proton elastic cross section is insensitive to the charge of the lepton. When higher-order scattering amplitudes are included, an interference term of order α^3 arises between the one-photon exchange and the hard two-photon exchange amplitudes, which is dependent on the charge sign of the lepton:

$$\sigma_{e^-p} \propto |\alpha\mathcal{M}_{1\gamma} - \alpha^2\mathcal{M}_{2\gamma} + \ldots|^2 = \alpha^2|\mathcal{M}_{1\gamma}|^2 - 2\alpha^3 Re\{\mathcal{M}_{1\gamma}\mathcal{M}_{2\gamma}\} + \ldots$$
$$\sigma_{e^+p} \propto |\alpha\mathcal{M}_{1\gamma} + \alpha^2\mathcal{M}_{2\gamma} + \ldots|^2 = \alpha^2|\mathcal{M}_{1\gamma}|^2 + 2\alpha^3 Re\{\mathcal{M}_{1\gamma}\mathcal{M}_{2\gamma}\} + \ldots$$

where $\mathcal{M}_{1\gamma}$ and $\mathcal{M}_{2\gamma}$ are the scattering amplitudes for the one-photon and the two-photon exchange amplitudes, and σ_{e^+p} and σ_{e^-p} are the differential cross sections for positron-proton and electron-proton scattering, respectively. To measure the two-photon exchange amplitude, the ratio of positron-proton to electron-proton is deter-

mined as given by Mar *et al.* (1968),

$$\frac{\sigma_{e^-p}}{\sigma_{e^+p}} = 1 + \frac{4Re\{\mathcal{M}_{1\gamma}\mathcal{M}_{2\gamma}\}}{|\mathcal{M}_{1\gamma}|^2}, \tag{2.26}$$

where $Re\{\mathcal{M}\}$ represents the real part of the one and two-photon amplitudes. With this method, the two-photon exchange amplitude $\mathcal{M}_{2\gamma}$ is measured as a deviation $\frac{\sigma_{e^-p}}{\sigma_{e^+p}}$ from unity.

The cross section ratio, $\frac{\sigma_{e^+p}}{\sigma_{e^-p}}$ as been measured by several groups (Yount and Pine, 1962), (Browman *et al.*, 1964), (Browman *et al.*, 1965), (Bouquet *et al.*, 1968), and (Mar *et al.*, 1968), which revealed results consistent with unity. However, these experiments were limited to a low Q^2 range, and had large uncertainties due to low-intensity positron beams. Conceivably, a larger contribution from two-photon exchange at higher Q^2 exists and needs to be measured with good precision. As stated before, the size of the two-photon amplitude varies significantly by theory, as does the expected $\frac{\sigma_{e^-p}}{\sigma_{e^+p}}$ ratio. Figure 2.6 shows some of the expected cross section ratio results from Afanasev *et al.* (2005), Blunden *et al.* (2003), Blunden *et al.* (2005), Borisyuk and Kobushkin (2006), and Tomasi-Gustafsson *et al.* (2013), and also includes phenomenological models from Chen *et al.* (2007), Guttmann *et al.* (2011), and Bernauer *et al.* (2014b),.

The measurement of $\frac{\sigma_{e^-p}}{\sigma_{e^+p}}$, in the search for the two-photon exchange contribution, was carried out by three recent experiments. This thesis will discuss the experimental method and results for the OLYMPUS experiment. The two other recent experiments that have measured $\frac{\sigma_{e^-p}}{\sigma_{e^+p}}$ were conducted on the VEPP-3 storage ring in Novosibirsk, (Rachek *et al.*, 2015), and at the CEBAF Large Acceptance Spectrometer (CLAS) two-photon Collaboration at Jefferson Lab. (Moteabbed *et al.*, 2013), (Rimal *et al.*, 2016), and (Adikaram *et al.*, 2015). The goal among the three experiments was to have a comprehensive search over a wide Q^2 and ϵ range, validated with different

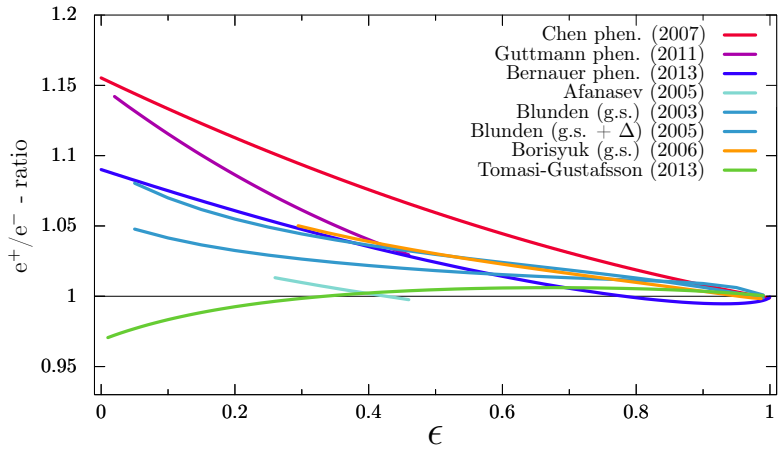

Figure 2.6: Predictions of the positron-proton to electron-proton cross section ratio, $\frac{\sigma_{e^-p}}{\sigma_{e^+p}}$ for several nucleon models and phenomenological models.

experimental methods. The reach of the three experiments is shown in Figure 2.7.

The experiment in Novosibirsk used a beam from the VEPP-3 $e^{\pm}$ storage ring incident on an internal hydrogen gas target. The measurement was made in two runs. For run-I, the beam energy was 1.6 GeV, and for the second run (run-II) the energy was 1.0 GeV. The measurement was made with a non-magnetic spectrometer with an angular range of 15° to 105° in polar angle and a wide acceptance in azimuthal angle. The measurement at small angles 7° to 15° was used for a luminosity normalization point.

The CLAS Collaboration used a different approach to produce the $e^{\pm}p$ scattering and to solve the issue of the uncertainty in the relative luminosity between data taken with the electron and positron beams. To produce the $e^{\pm}$ beams, electrons and positrons were pair produced from a photon beam incident on a gold foil. This produced a mixed e^+, e^- and photon beam, which was separated with a three-dipole magnet. The photons were stopped with a photon blocker, and the e^+ and e^- were recombined to form a single beam impinging on a liquid hydrogen target. The cross

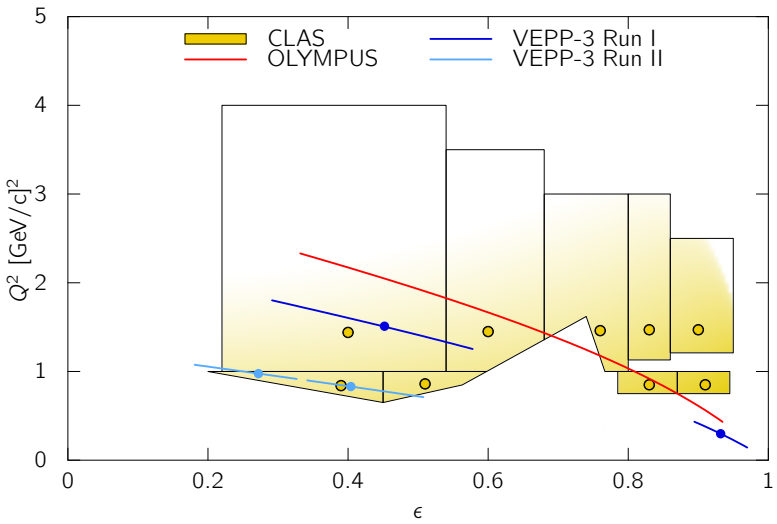

Figure 2.7: The Q^2 and ϵ reaches of the three two-photon exchange experiments. The CLAS measurement does not have a fixed beam energy, corresponding to the large spread and bin size in Q^2 and ϵ. The color variance in the CLAS reach represents the log of the event rate. The figure is courtesy of (Schmidt, 2016).

section ratio was then measured with CLAS.

The results from VEPP-3, (Rachek *et al.*, 2015), and the CLAS experiment, (Rimal *et al.*, 2016), and (Adikaram *et al.*, 2015), have been published.

Chapter 3

EXPERIMENTAL SETUP

To measure the cross section ratio, the initial lepton-proton reaction was created using 2.01 GeV electron and positron beams incident on an unpolarized hydrogen gas target. The outgoing particles were tracked using a system of detectors positioned in and around a large electromagnet. For a detailed description of the OLYMPUS detector system, see Milner *et al.* (2014).

The main goal of the OLYMPUS experiment was to measure the positron-proton to electron-proton elastic scattering cross section ratio over large Q^2 with low statistical and systematic uncertainties. To this end, the design goals for OLYMPUS were as follows:

- To make an exclusive measurement of the cross section ratio to large Q^2 required a large acceptance spectrometer. For this experiment, the spectrometer subtended a scattering angle from approximately 20° to 70°. With a beam energy of 2.01 GeV, a Q^2 range from 0.4 $(\mathrm{GeV/c})^2$ to 2.2 $(\mathrm{GeV/c})^2$ was achieved.

- To keep statistical uncertainties as low as possible required that the beam and target provided a sufficient integrated luminosity, which in turn demanded a high density of hydrogen gas in the target cell and a high beam current.

- To minimize systematic uncertainties several experimental techniques were employed:

  - A left/right symmetric detector to help understand detector efficiency related systematic uncertainties.

– Switching between positron and electron beams daily reduced time-dependent uncertainties.

– Good angular resolution isolate signal from background.

– The electron beam and positron beam relative luminosity was a large source of uncertainty in the experiment. To measure the relative luminosity, several independent methods were used. These are discussed in Section 3.4.

Focusing on the aims requirements for a precision cross section ratio measurement, this section describes the experimental setup.

3.0.1 OLYMPUS Coordinate System

The coordinate system used for OLYMPUS was a right-handed Cartesian system with the z-axis pointing downstream along the beamline, and the y-axis pointing vertically up, normal to the lab floor. This forced the positive x-axis to point horizontally left with respect to the positive z-axis (the direction of the beam). The system origin ($(x, y, z) = (0, 0, 0)$) was placed at the center of the OLYMPUS target cell. The spectrometer was symmetric about the yz-plane and a particular side was referred to as either the "left sector" (along the positive x-axis) or the "right sector" (along the negative x-axis). This coordinate system is shown in Figure 3.1.

This coordinate system was used to describe the experimental apparatus in terms of the OLYMPUS spectrometer, the target, and the beam, and was also used for the data analysis and results. Other useful parameters were the scattering angles with respect to this system. First, the scattering angle (or polar angle) θ was the angle between the initial path of a scattered particle in the lab frame and the positive z-axis; the azimuthal angle φ was the angle between the initial path of a scattered

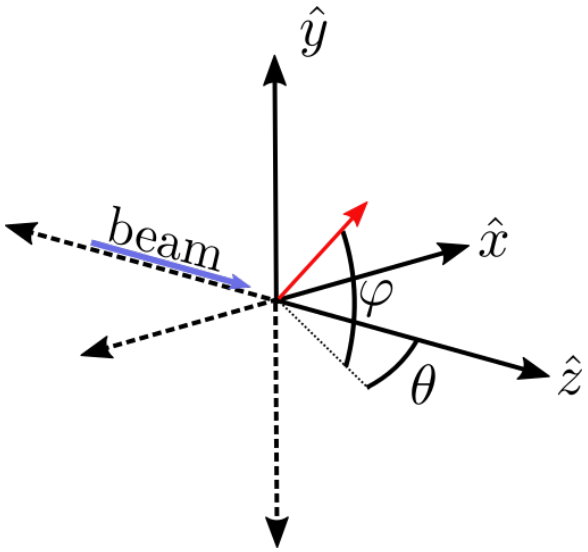

Figure 3.1: The coordinate system for OLYMPUS. The origin (0,0,0) is placed at the center of the target cell and the angles are used to describe scattered particles.

particle and the xy-plane.

3.1 Lepton Accelerator

The lepton beams were supplied by the Doppel-Ring-Speicher (DORIS III) storage ring at DESY Laboratory in Hamburg, Germany. Originally designed as a electron-electron and electron-positron collider, DORIS was the first storage ring in Germany, built in 1973. After the decommissioning of the ARGUS detector in 1993, DORIS was primarily used as a synchrotron radiation source for a wide range of experiments in chemistry, biology, and material science.

Because DORIS could store electron and positron beams at several GeV, the facility was ideal for the OLYMPUS experiment. The OLYMPUS spectrometer was placed in the former location of the ARGUS experiment, and was able to use much of the existing support structure, such as a pit with rails that allowed the detector to be moved in and out of the beam line. Also on the rails, and moved with the detector,

was a small air-conditioned hut to house electronics. Downstream of the detector, shielding was placed to block large amounts of downstream radiation. Upstream of the detector beam scrapers were used to reduce synchrotron radiation and particle backgrounds in the detector. To monitor the energy of the beam, an extra dipole magnet with a rotating coil to measure integrated field strength was added in series with the DORIS dipole magnets.

OLYMPUS ran with a beam energy of 2.01 GeV and a beam current between 58 mA and 65 mA. Because the pre-accelerators and DORIS injection kickers were able to bring the leptons up to the full 2 GeV energy, the beam was able to be refilled in what was called "top-up mode". In this mode, small pulses refilled the beam more often, which allowed for OLYMPUS to run at a higher and more stable beam current. During the brief injection of particles, the Data Acquisition (DAQ) system was automatically paused and restarted when the injection was finished. The DORIS pre-accelerators were able to switch between beam species in 10 minutes. The beam species was switched daily to avoid long time-scale systematic uncertainties.

The beam was delivered in bursts of 10 bunches, which corresponded to a bunch spacing of 96 ns. The beam horizontal beam emittance was 200 nm$\times$radians and the vertical beam emittance was 5 nm$\times$radians. The DORIS beam clock recorded when a bunch passed into the target region, and a signal from that clock was used as a common-start trigger for the electronics and as a reference time for the time-of-flight time-to-digital converters (TDCs).

3.2 Hydrogen Target

The OLYMPUS experiment used an unpolarized, internal hydrogen gas target as described in (Bernauer *et al.*, 2014a). Achieving the goal luminosity within the time and beamline restrictions required a thick target of approximately 3×10^{15} atoms/cm^2.

The target was created by pumping ultra-pure molecular hydrogen gas though a small inlet in the center of a thinly-walled aluminum target cell. The cell was a long, thin, open ended tube that was interconnected directly to the beam line. A vacuum system consisting of turbomolecular vacuum pumps and non-evaporable getters removed the gas from the cell ends to restore the vacuum of 10^{-9} Torr within the surrounding DORIS beam line. The cell was cooled to increase the gas conductance and gas density within the cell. The desired target density was achieved at a cell temperature of 75K and a hydrogen gas flow rate of 0.6 standard cubic centimeters per minute. To limit the effects of synchrotron radiation and beam halo, a tungsten collimator was placed in front of the upstream opening of the target cell. Gaps and sharp transitions between conducting materials in the target cell acted as electromagnetic cavities. The high current of the DORIS beam excited the cavities, causing wakefield heating in the target. To maintain cryogenic temperatures, wakefield suppressors (conducting transitions between the conductive materials in the target system) were added. The target cell, collimator, and wakefield suppressors were all housed in a scattering chamber. A diagram of the target system without the scattering chamber is shown in Figure 3.2.

3.2.1 Target Cell

The target cell was made of aluminum, spot-welded to form an open-ended elliptical cylinder, 27 mm by 9 mm in cross section and 60 cm long. The ellipse aspect ratio matched the DORIS beam envelope out to approximately ten standard deviations the nominal beam distribution to minimize the amount of beam halo hitting the sides of the cell. To reduce multiple scattering, the cell was made of very thin (70 μm) aluminum. The cell was wrapped in aluminized mylar thermal insulation and cooled using a cryogenic coldhead. A cryogenic temperature of $\sim$40 K could be

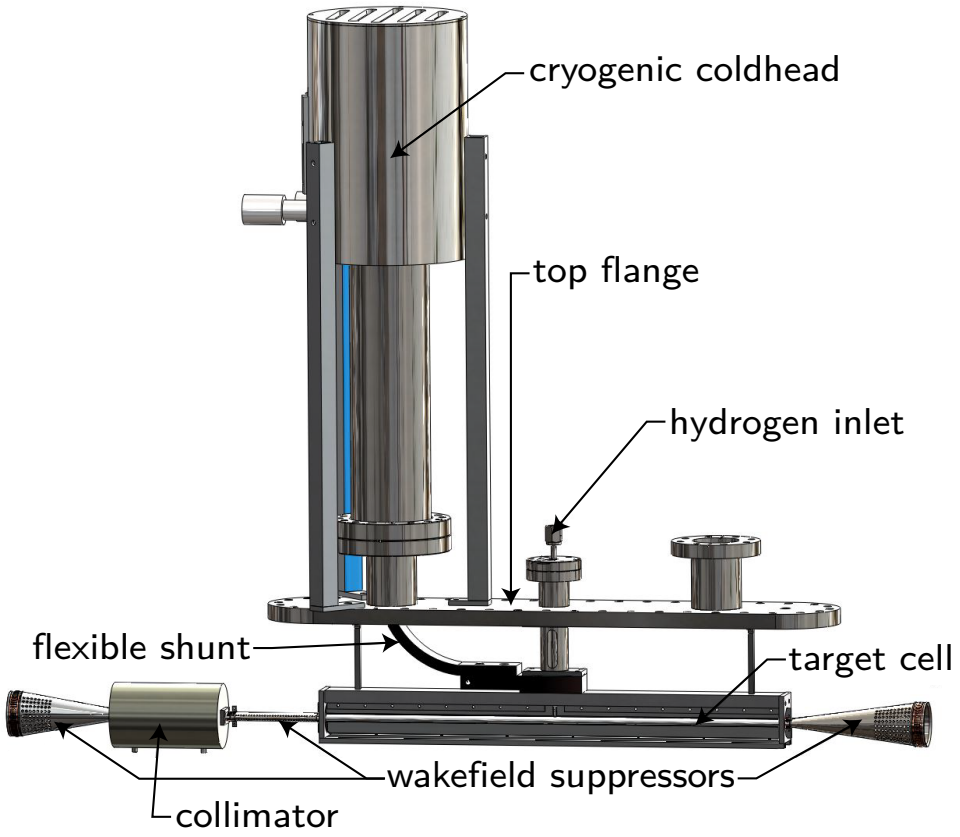

Figure 3.2: The target system for OLYMPUS without the scattering chamber.

achieved with no beam, but the normal running cryogenic temperature during data taking was 70 K.

Hydrogen gas was pumped through an inlet at the center of the cell and diffused outwards towards the ends of the cell. The vacuum pumps and getters removed the gas that diffused past the ends of the target cell, creating a triangular density function along the length of the cell. By cooling the cell, the diffusion was slowed, creating a dense gas volume.

3.2.2 Collimator and Wakefield Suppressors

To keep the target cell at cryogenic temperatures, wakefield suppressors were used to reduce wakefield heating from the beam. The wakefield suppressors were constructed out of aluminum with small holes drilled to allow for the gas escape into the scattering chamber. The upstream wakefield suppressors were coated in silver to increase electrical conductivity.

To reduce the contribution of events from beam halo particles, a 139.7 mm long by 82.55 diameter tungsten cylinder collimator was placed just upstream of the target cell.

3.2.3 Scattering Chamber

The target cell, collimator, and wakefield suppressors were all housed inside an aluminum scattering chamber. The chamber was machined out of a solid block of aluminum to ensure the chamber could hold vacuum. The chamber was 1.2 meters long, with the upstream face 254 mm high by 245 mm wide. The chamber tapered downstream to a width of 114.3 mm to increase the solid angle seen by the target cell to the downstream detectors. Ports on either end of the scattering chamber connected directly to the beamline, and the inside of the chamber was open to the beam vacuum. Relative to the beam axis, the two left and right faces had 0.25 mm thick aluminum windows spanning the entire acceptance range of the spectrometer. The thin windows reduced multiple scattering after a beam crossing.

3.3 The OLYMPUS Spectrometer

The OLYMPUS detector was a large acceptance spectrometer built around an eight-sector toroidal magnet, and was symmetric about the yz-plane. The detec-

tor reused many of the components from the Bates Large Acceptance Spectrometer Toroid (BLAST) (Hasell *et al.*, 2009) including the magnet, drift chambers, time-of-flight detectors and the support structure. For OLYMPUS, the BLAST detector components were refurbished, and the detector was upgraded with new luminosity monitoring subsystems. A detailed description of the spectrometer can be found in (Milner *et al.*, 2014). An image of the OLYMPUS spectrometer, with the top four magnet coils removed, is shown in Figure 3.3. The detector subsystems are labeled in that figure.

The main tracking detectors were two drift chambers located in the horizontal sectors of the magnet. The drift chambers defined the acceptance range to be from $\sim$25° to $\sim$75° scattering polar angle and $\sim \pm 15°$ in the azimuth. Further from the target and outside of the magnet coils were time-of-flight (ToF) scintillator paddle arrays, used primarily for triggering and particle identification. Two independent luminosity monitoring systems were added to the OLYMPUS spectrometer. At 12° polar angle, luminosity telescopes, consisting of alternating Gas Electron Multiplier (GEM) and Multi-Wire-Proportional-Chambers (MWPC) detectors, measured forward angle lepton-proton scattering; the multiple photon exchange contribution to the elastic cross section was expected to be small at forward angles. At 1.28° scattering angle, lead fluoride calorimeters measured the well-known symmetric Møller and Bhabha scattering cross sections created from the beam interacting with electrons in the hydrogen target.

3.3.1 Magnet

The OLYMPUS magnet consisted of eight copper coils in a toroidal configuration centered around the beam line. The benefit of a toroid was the minimization of the magnetic field along the beamline, as well as the small field gradient in the

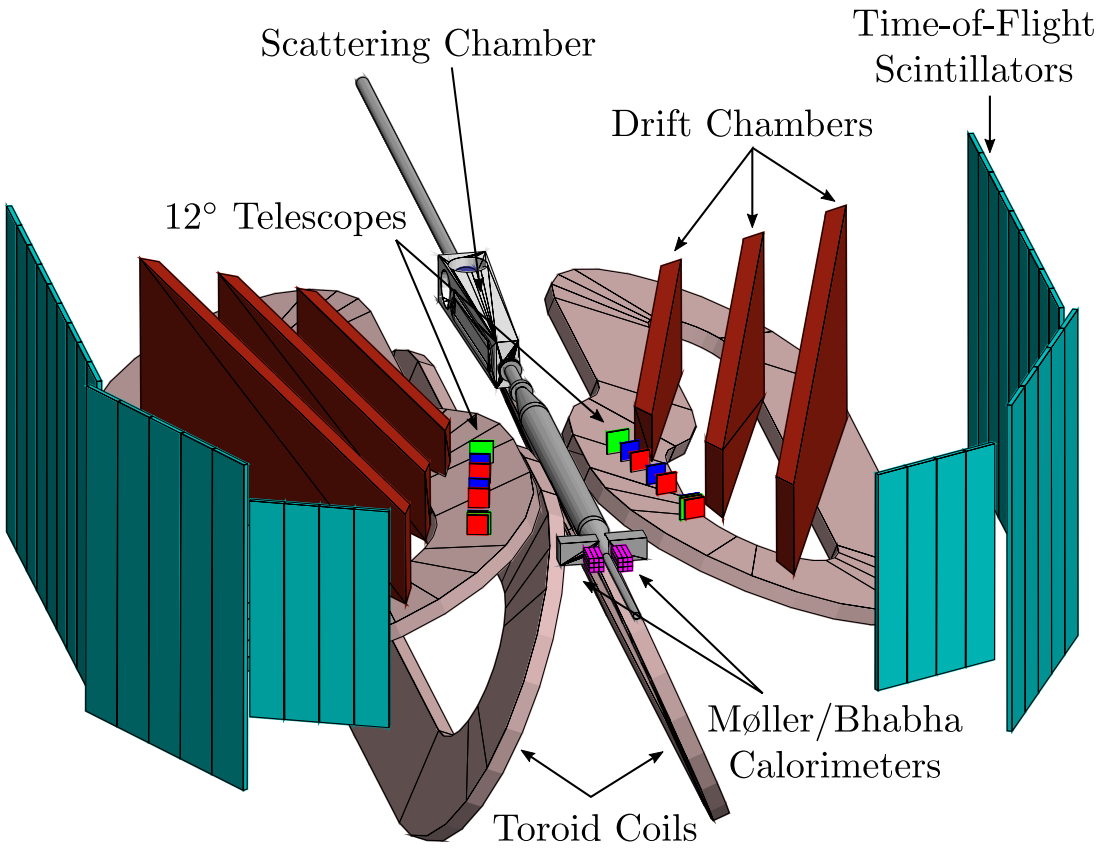

Figure 3.3: The spectrometer used for the OLYMPUS experiment. The top four sectors of the magnet have been removed to make the detector elements visible.

space between the coils. A small magnetic field along the beamline minimized beam position and beam direction interference. Each coil was built from 3.81-cm-square copper tubes arranged in two layers of 13 turns. Along the center of each tube was a 2.032 cm diameter circular hole for cooling water flow. The tubes were wrapped in fiberglass tape, and epoxy resin was used for potting.

During data taking, the current through the magnet was set at 5000 A to produce an average field strength of 0.28 T. The magnetic field bent the trajectories of charged particles, allowing their momentum to be measured, and pushed low-energy backgrounds out of the acceptance of the drift chambers. The magnetic field had to be large enough to achieve both these goals, while not decreasing drift chamber detection efficiency. These goals were achieved by supplying the magnet with 75% of the maximum current of 6730 A.

To lower systematic errors the polarity of the magnetic field was originally intended to change every four hours during beam time. Unfortunately, the magnetic field polarity that bent negatively-charged particles away from the beamline flooded the inner drift chambers with electron backgrounds, rendering the drift chamber useless in this configuration. After failed attempts to shield the inner chamber and attempts to decrease the backgrounds by increasing the magnetic field strength, this configuration was abandoned. The rest of the data were taken with the magnetic field polarity where the magnetic field bent positively-charged away from the beamline.

After the completion of data taking, the magnetic field in the tracking region was mapped using a three-dimensional Hall probe mounted on translation tables. Over 36,000 field data-points were measured in an evenly spaced grid so that the field could be interpolated between field points. A spline-based function was used to generate field values between the data points, as described by Bernauer *et al.* (2016).

3.3.2 Drift Chambers

The main tracking detectors for OLYMPUS were six drift chambers, arranged into two sectors, as shown in maroon in Figure 3.3. The sectors were placed in the two horizontal sections of the toroid, and covered $\sim 20^\circ$ to $\sim 80^\circ$ scattering angle and $\pm 15^\circ$ in the azimuth. For each sector, the drift chambers were connected via an aluminum frame into a single gas-volume, requiring particles which traversed the sector to pass through only two thin mylar windows, which minimized multiple scattering and energy loss in the windows. The gas used was an $Ar:CO_2:C_2H_6O$, (87.4:9.7:2.9) mixture produced by bubbling $Ar:CO_2$ (90:10) through liquid ethanol, (C_2H_6O).

Because the drift chambers were nested between the magnet coils, the best shape for the sectors were trapezoidal frusta, tapering closer to the beam line. The wires were strung vertically between the top and bottom faces of the chamber though a pattern of holes machined in the aluminum. A diagram of the pattern for a small section of one chamber is shown in Figure 3.4. The wires were grouped together into "cells", consisting of three sense wires (each shown as a red "x") and 36 field wires (shown as black dots). Each cell shared 18 wires, held at ground potential, with adjacent cells. The field wires, when at high voltage, created an electric field, which guided the ionization electrons toward the three sense wires in the center column. The lines of constant electron drift, when the chamber is placed in an external magnetic field, are shown as blue lines in Figure 3.4. The sense wires were set at high voltage to produce an electron cascade close to the sense wire, which was then collected to produce a signal. The sense wires were staggered by ± 0.5 mm from the center column to help resolve whether tracks had passed to the left or the right of the center plane. The cells were arranged into two rows in each chamber separated by 20 mm. The two

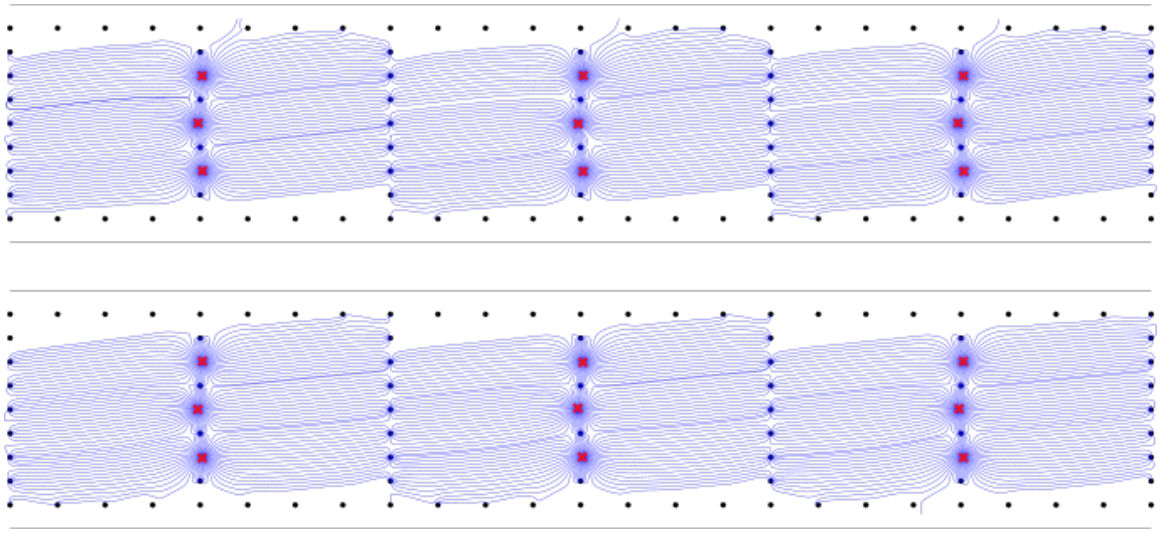

Figure 3.4: A cross section of drift chamber cells in one drift chamber (two superlayers). The cathode or field wires (black), the anode or sense wires (red) and the electron drift lines (blue) for magnetic field around 0.3 T.

rows were set at a 10° stereo angle from each other, allowing for the vertical position of the track to be reconstructed.

The large electron drift velocity of 30 mm/μs in the Ar:CO_2 gas mixture decreased the spacial resolution in the drift chambers, and made the $\pm$0.5 mm staggering ineffective in resolving the left-right ambiguity in the cells, which complicated the track reconstruction considerably.

The signals from the sense wires were decoupled from the high-voltage baseline using custom high-voltage distribution boards. The signals were then sent to amplifier/discriminator cards and Ethernet cables carried the signals to a multi-hit time-to-digital converter (TDC), which measured the signal time occurrence relative to a common stop time, produced by the ToF scintillator detectors discussed in the next section. Using the timing signals, the 3-dimensional trajectory for each charged particle passing through the gas volume could be reconstructed.

3.3.3 *Time-of-Flight Scintillators*

Covering the acceptance range of the drift chambers were 18 time-of-flight (ToF) scintillator detectors. These detectors were long paddles of plastic scintillator, connected via light guides to photo multiplier tubes (PMTs). As shown in Figure 3.3 (in dark aqua) the ToF detectors were arranged vertically into three panels per sector. Most of the scintillator paddles were $180.0 \times 26.2 \times 2.54$ cm. The most downstream panels of the ToFs however,consisted of four paddles per sector; these scintillators were closer to the beamline and therefore could be smaller ($119.4 \times 17.8 \times 2.54$ cm) and still cover the same azimuthal acceptance range. Bicron BC-408 plastic scintillator, with a polyvinyl toluene base, was used for the ToF detectors because of the short rise time of the material (≈ 0.9 ns) and long attenuation length (≈ 210 cm). The scintillator paddles were wrapped with aluminum foil and a kapton sheath. A thin layer of lead (0.30 mm - 0.60 mm) was placed inside the kapton wrapping on the target-side of the scintillator in order to stop low energy electrons. The PMTs were 9822B02 electron tubes coupled to EBA-01 bases. The light guides oriented the PMTs away from the center of the detector causing them to be perpendicular to the magnetic field. Each PMT was surrounded by μ-metal shielding to minimize the effect the magnetic fields had on the PMT. A photograph of the ToF detectors on the OLYMPUS spectrometer is shown in Figure 3.5. The photograph shows the OLYMPUS detector before being rolled onto the beamline.

Signals from the PMTs were sent through passive splitters to time-to-digital converter (TDC) and integrating amplitude-to-digital converter (ADC) modules. For all but the back-most two bars in each sector (which had leading edge discriminators) each analog PMT signal was directed into a constant-fraction-discriminator (CFD). The signal was used primarily as a trigger for the detector readout, as will be described

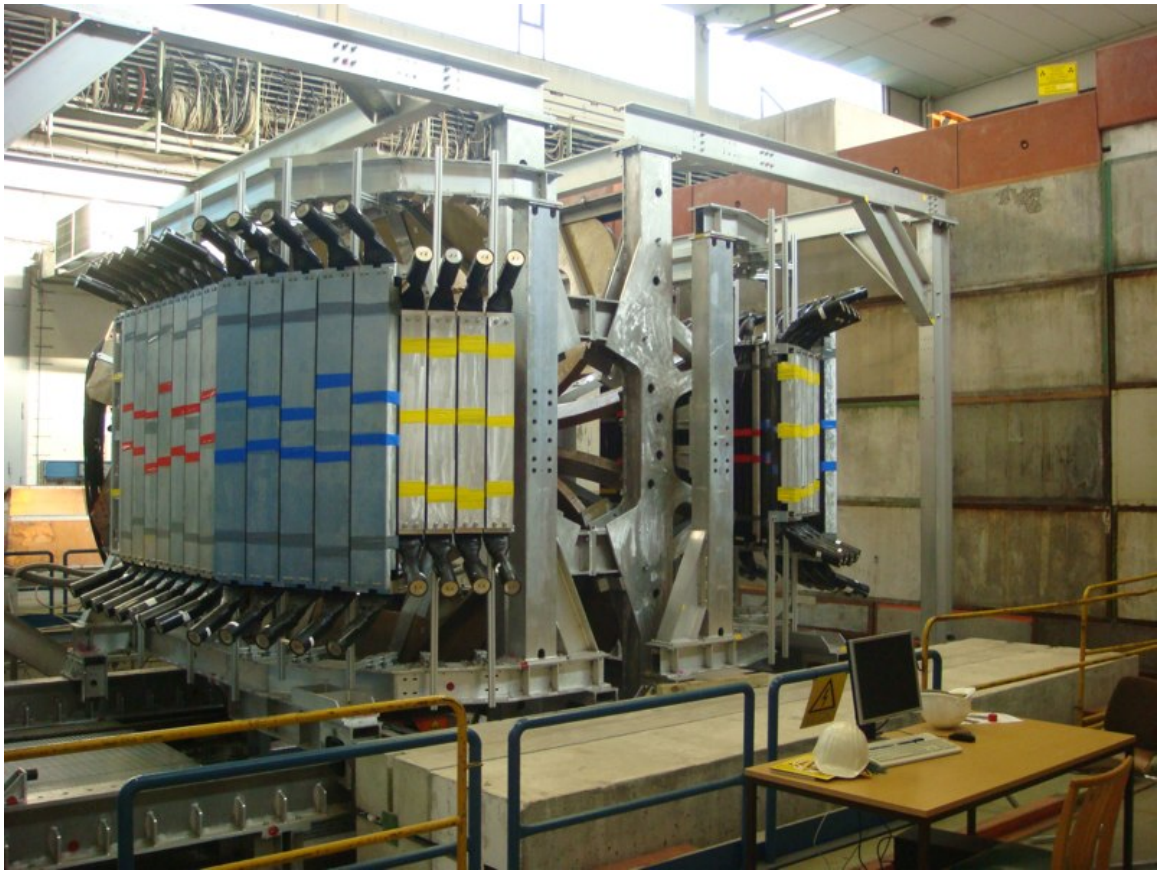

Figure 3.5: The time-of-flight paddles on the OLYMPUS spectrometer. The scintillators are behind the aluminum support structure with the yellow, blue and red tape. The PMTs were connected to the top and bottom of the scintillator paddles, tilting away from the vertical.

in section 3.5, and as a common-stop for the drift chamber TDCs. The ToF TDCs used a common-start provided by the beam bunch clock and therefore also provided a measurement of the particle flight time. This flight time for each charged particle (once calibrated) provided important information for particle identification (PID) methods, and was used to calibrate the timing offset for the drift chamber TDCs. The TDC difference between top and bottom PMTs, after calibration, provided a method to calculate the azimuthal angle of the hit. This was used as a starting estimate of the azimuthal angle in the track reconstruction, discussed in section 4.3. By integrating

the PMT pulse in the ADC, the energy deposited in the scintillator was estimated and provided additional particle ID information. The particle ID methods using ToF information are discussed in 5.2.1.

3.4 Luminosity Monitors

Since the OLYMPUS measurement was a ratio of cross sections, the relative luminosity between positron and electron beams had to be determined to high precision and accuracy. To ensure the low uncertainty in the relative luminosity measurements, three independent methods were used to monitor monitor the luminosity ratio. The least precise luminosity measurement was made by monitoring the target gas flow, the target temperature, and the beam current. With that information, the density of gas in the target was estimated and the luminosity calculated. A second method was to estimate the luminosity by measuring lepton-proton scattering at small lepton scattering angle. Since most theoretical predictions show that the two-photon exchange effect is small or negligible at small lepton scattering angles, the relative lepton-proton cross sections at low scattering angle gave an estimate for the relative luminosity. To monitor the forward angle scattering, luminosity telescopes were set up at 12° lepton scattering angle. A third method monitored the luminosity by measuring the Møller ($e^-e^- \to e^-e^-$) and Bhabha ($e + e^+ \to e^+e^+$) scattering of the beam leptons off the electrons in the hydrogen target. Measuring the rates of lepton-lepton scattering at symmetric angles provided a precise luminosity monitor. This was achieved by very forward angle 1.28° calorimeters. A diagram of the luminosity monitoring detectors with the target and beam line is shown in Figure 3.6.

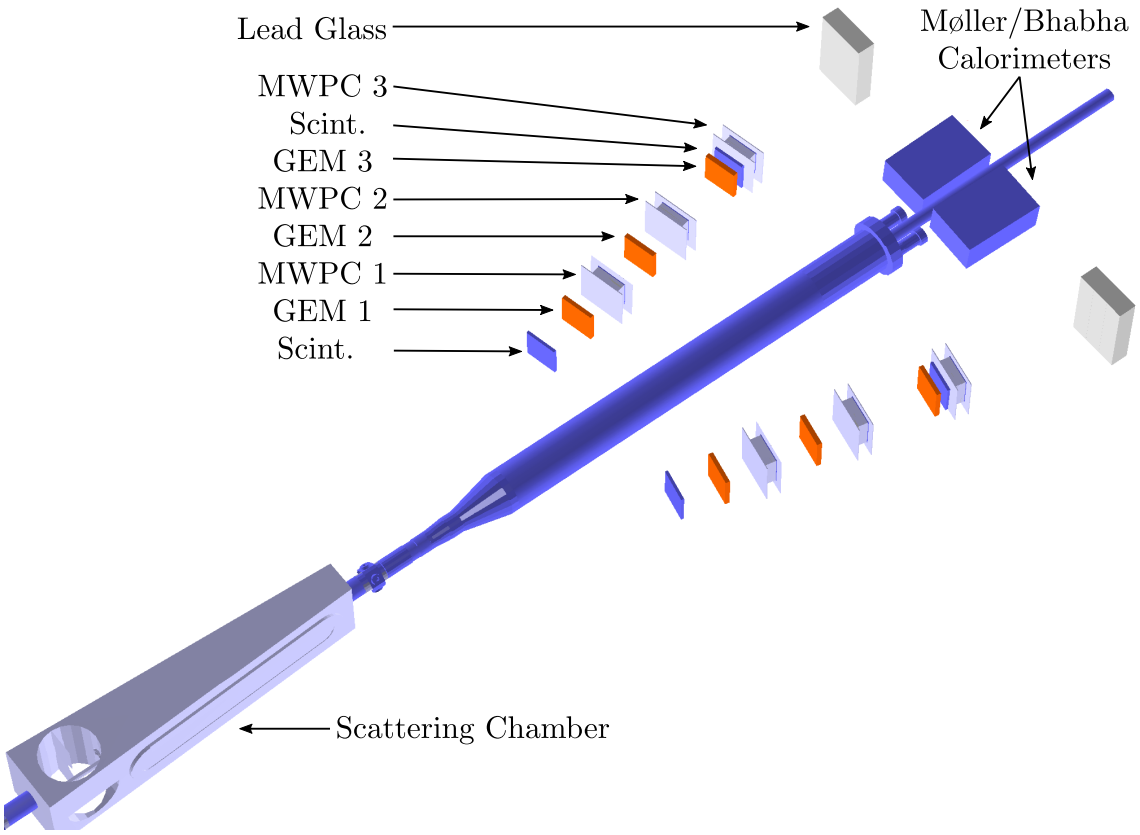

Figure 3.6: A diagram of the luminosity telescopes at 12° and the symmetric Møller and Bhabha calorimeters.

3.4.1 The 12° Telescopes

A 12° lepton scattering angle corresponds to approximately $Q^2 = 0.17$ (GeV/c)^2, where most theoretical predictions expect the two-photon exchange to be small or negligible. With this assumption, the luminosity can be monitored by counting the rates of forward lepton scattering for positron beam and electron beam. This was done with two telescopes of alternating GEM and MWPC detectors, as shown in Figure 3.6.

The detectors were mounted on rails and placed just forward of the drift chambers at 12° scattering angle. In that position, most of the target area could be monitored

with the telescope. There were three GEM detectors and three MWPCs for a total of six detector planes for each telescope. The two scintillators, the first placed between the scattering chamber and the first GEM, and the second between the last GEM and MWPC, were used for the trigger. Scintillation light from particles passing through the scintillator was captured with silicon photo multiplier multi-pixel photon counters. A coincident hit in both scintillators in one arm and a ToF hit in the opposite sector triggered the readout of signals in the 12° telescopes. A lead glass calorimeter was behind the GEM and MWPCs consisting of three lead glass bars with a PMT readout. This monitored the efficiency of the scintillator trigger during the experiment.

The GEM detectors each consisted of three GEM foils, a 2D strip readout board, a cathode foil, and two pressure volume foils. The foils were held apart by frames and stacked together. The detector was filled with a Ar:CO_2 (70:30) gas mixture. The cathode foil was made of kapton with a thin layer of copper on one side, which provided a uniform electric field across the GEM detector. The three GEM foils, made by TechEtch, were kapton with a thin layer of copper on both sides and chemically etched with 70 μm holes. Each GEM measured 10 cm by 10 cm. A readout board made of a kapton substrate was behind the GEM foils. On the side facing the GEMs, a pattern of copper lines and pads collected the ionization electrons from the gas and produced a two-dimensional hit position. On the front and back faces of each GEM stack, pressure volume foils of aluminized mylar enclosed the gas volume and electrically shielded the GEM foils.

The MWPCs consisted of three anode planes of sense wires alternating with cathode wire planes. The angle of the wires in the anode places were off set by 30° so that two-dimension readout was possible. Each wire plane was in a fiberglass frame, stacked together together in an aluminum outer frame. Each MWPC covered an active area of 112 mm by 112 mm. The gas used was Ar:CO_2:CF_4 (65:30:5).

3.4.2 Møller and Bhabha Calorimeters

The luminosity was also monitored by measuring the rates of Møller and Bhabha scattering produced by the lepton beam incident on the atomic electrons in the hydrogen target. The Møller and Bhabha cross sections are precisely calculable with quantum electrodynamics, and therefore the relative rates of Møller and Bhabha scattering provided a high rate luminosity monitor. To limit background processes, OLYMPUS measured the Møller and Bhabha scattering at symmetric scattering angles, which for a 2.01 GeV beam, was at $\pm 1.29°$. This allowed for the lepton-lepton peaks to be clearly identified. The physical signals observed in the calorimeters were the Møller scattering, Bhabha scattering, pair annihilation ($e^+e^- \rightarrow \gamma\gamma$), and very forward angle lepton-proton scattering.

This measurement was made by two lead fluoride PbF_2 calorimeters placed at $1.29°$ scattering angle on either side of the beam line in the horizontal plane. Each calorimeter consisted of a three-by-three array of lead fluoride crystals, wrapped in millipore paper to increase surface reflectively and reduce light loss. The front face of the crystals were 26-by-26 mm square and slightly tapered towards the back. Each calorimeter was 160 mm long, which was roughly equivalent to 15 radiation lengths. Each crystal was connected to a PMT which read out Cerenkov light produced by the particles passing through the crystal. With the high rates of Møller and Bhabha scattering, this method provided an accurate luminosity measurement on a short time scale.

The calorimeters were placed inside a μ-metal box to shield the PMTs from the toroidal magnetic field. Between the target and the front face of the calorimeters were lead collimators, which provided shielding from bremmstrahlung and non-symmetric Møller and Bhabha scattering.

To trigger an event, the sum of the analog signals from all nine crystals in a calorimeter needed to exceed a threshold as measured by a constant-fraction discriminator. The center crystal of the three-by-three grid was required to have the largest signal. When an event was triggered, the summed signals were digitized and sorted into a histogram of left ADC channel versus right ADC channel. Because of the fast rate, each event was not read out individually, but instead the ADC histogram was sent to the data acquisition system periodically.

3.5 Event Trigger

The primary event trigger system for OLYMPUS relied on signals from the ToF scintillators, the two scintillators in the 12° arms, and the DORIS beam information. The trigger logic was implemented in a VME-field programmable gate array (FPGA) module to combine 16 detector signals into 16 parallel trigger conditions with independent pre-scaling factors. The main event trigger for elastic scattering through the drift chamber region required coincident signals from both the top and bottom PMTs on at least one ToF paddle in both left and right detector sectors. Since OLYMPUS was only interested in measuring elastic lepton-proton scattering, the ToF trigger was reduced to ToF paddles corresponding to kinematically allowed angular ranges, which significantly increased the signal-to-noise ratio in the forward section of the detector. The trigger for luminosity monitoring in the 12° arm required coincident signals in the two scintillators on the 12° arm and a signal from both PMTs on a ToF paddle in the opposite sector. In addition to these two trigger conditions, other significantly pre-scaled triggers requiring less restrictive ToF conditions were included for efficiency calibrations and to monitor non-elastic backgrounds. When a trigger condition was met, all detectors were read out simultaneously and all other triggers were stopped until the signals were read out entirely.

To further increase the signal-to-noise in the drift chambers, a second level trigger was included. This trigger required that at least one wire in the middle and outer drift chambers in both sectors registered a signal. This reduced the false trigger rate in the drift chambers by a factor of 10.

3.6 Running

During data collection, the slow control system allowed for many parameters, such as detector high voltage, magnetic field, target parameters, and beam information, to be monitored, modified, and recorded. The Experimental Physics and Industrial Control System (EPICS) was used for the slow control system, and provided parameter information continuously during data taking. The slow control parameters were collected and stored in a PostgreSQL database.

While the data was being collected, the experiment ran continuously and the beam species were switched once every morning. During the Fall 2012 data period, the magnetic field was kept at the same polarity to avoid high backgrounds being pushed into the drift chambers with the "negative" field polarity. In total, approximately 4 fb^{-1} of data was taken, providing sufficient statistics for this measurement. The luminosity as a function of time is shown in Figure 3.7.

During breaks in the data taking and after the Fall data period finished, cosmic ray data were collected with the detector. The comsic ray data were used for detector calibration, as described in Chapter 4.

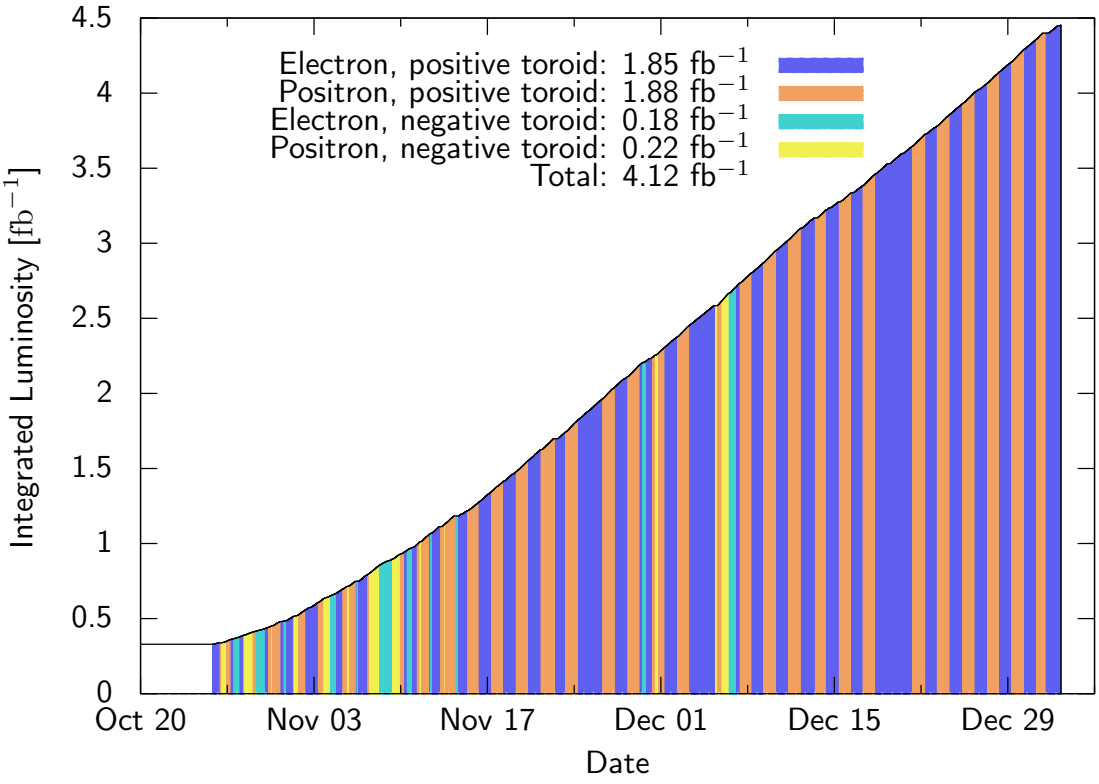

Figure 3.7: The integrated luminosity as a function of time.

Chapter 4

PRELIMINARY DETECTOR ANALYSIS

To make a cross section ratio measurement, elastic electron-proton and positron-proton scattering events were reconstructed from the signals recorded in the detector subsystems. To reconstruct elastic scattering events and to help differentiate between elastic scattering and background, as will be discussed in Chapter 5, the scattering angles, θ and φ, momentum p, and the scattering vertex position in the target z were determined from each charged particle's trajectory through magnetic field within the OLYMPUS detector.

This chapter discusses the detector calibration and track reconstruction used to reconstruct the tracks and the scattering events. The time-of-flight (ToF) detector calibration and analysis constrained drift chamber tracks and was used for particle identification (PID) methods. From the signals in the drift chambers, the tracks were fully reconstructed, and the kinematic parameters for each scattered particle – θ, φ, p and z – determined. Also discussed are the analyses and results from the luminosity systems.

4.1 Time-of-Flight Detectors

The ToF detectors provided measurements of the flight time of charged particles coming from the target and through the magnetic field region, and a measurement of the azimuthal scattering angle φ. This provided important starting points and bounds for the track reconstruction through the drift chambers. The ToF detectors also provided the timing and energy deposition information necessary for PID methods. This section will discuss how the ToF detectors were calibrated.

The time-of-flight for each event was calculated with the ToF detectors using the two time-to-digital converters (TDC) signals. For a paddle i, the mean-time t_i was measured as

$$t^i = \frac{1}{2}\left(\mathrm{TDC}_b^i + \mathrm{TDC}_t^i\right) t_{\mathrm{res}}, \tag{4.1}$$

where TDC_t^i (TDC_b^i) was the calibrated TDC time for the top (or bottom) photomultiplier tube (PMT). The TDC channel time, which was the conversion factor from TDC channels to nanoseconds, was $t_{\mathrm{res}} = 0.05$ ns per TDC channel. The mean-time that was measured was different from the actual time-of-flight by a constant factor of $\frac{L^i}{2v_{\mathrm{sc}}^i}$, where L^i was the length of the scintillator and v_{sc}^i was the measured speed of light in the scintillator. However, this factor was folded into the TDC delay calculated in Equation (4.4) below. The time-of-flight was used in the initial time-to-distance parameterization and the TDC offset for the drift chambers.

The vertical position in the scintillator paddle where a particle passed through ToF was found from the difference in the top and bottom TDC signals as,

$$y^i = \frac{1}{2}\left(\mathrm{TDC}_b^i - \mathrm{TDC}_t^i\right) v_{\mathrm{sc}}^i, \tag{4.2}$$

where v_{sc}^i was the calibrated speed of light in the scintillator bar, given in mm per TDC channel. With the vertical position y^i, the azimuthal angle of a track φ was calculated using the difference in position along the x-direction from the paddle to the beam line axis D_x^i as

$$\tan\left(\varphi\right) = \frac{y^i}{D_x^i}. \tag{4.3}$$

The azimuthal angle φ was used as a starting parameter for the track reconstruction fitting algorithm.

For Equations (4.1) and (4.2), $\mathrm{TDC}_{t(b)}^i$ was the calibrated TDC time, which was related to the raw TDC time $\left(\mathrm{TDC}_{raw}\right)_{t(b)}$ by an offset as

$$\mathrm{TDC}_{t(b)}^i = \left(\mathrm{TDC}_{\mathrm{raw}}\right)_{t(b)}^i + \left(\mathrm{TDC}_{\mathrm{delay}}\right)_{t(b)}^i - \mathrm{TDC}_{\mathrm{ref}}. \tag{4.4}$$

The $\mathrm{TDC_{ref}}$ was the reference time given by the beam bunch clock counter and $(\mathrm{TDC_{delay}})^i_{t(b)}$ was the TDC time delay from TDC electronics, cables, and trigger. The TDC time delays and the speed of light in the scintillator were calibrated from data, using either cosmic ray data or a selection of elastic scattering events. Because the calibrations were found from data, $\mathrm{TDC_{delay}}{}^i_b$ and $\mathrm{TDC_{delay}}{}^i_t$ could not be found with independent calibrations. Instead, those constants were extracted from calibrations of $y^i_{L(R)}$ and $t^i_{L(R)}$.

4.1.1 Mean-Time Delays

The delays in the calculated mean-time (given in Equation (4.1)) for each paddle were calibrated using cosmic ray events, where a cosmic ray passed through ToF bars in both the left and right sectors of the detector. For this calibration, the relative mean time offsets were labeled as $(t_{\mathrm{offset}})^i_R$ and $(t_{\mathrm{offset}})^j_L$, where the index i was used for the ToF paddles in the right sector and j for the left sector.

For the left/right coincident events, the mean time difference corrected by the angle of the cosmic ray,

$$(t^i_R + t^j_L)/\cos(\phi_{\mathrm{cosmic}}), \tag{4.5}$$

was binned into 18×18 histograms. The angle of the cosmic ray relative to the xz-plane ϕ_{cosmic} was found using the reconstructed hit positions and the distance between the two ToF paddles D_{ij} as

$$\tan(\phi_{\mathrm{cosmic}}) = \left|y^i_R - y^j_L\right|/\mathrm{D}_{ij}. \tag{4.6}$$

When histograms of Equation (4.5) were produced, two Gaussian peaks were found, as shown in Figure 4.1. The negative peak was produced from particles traveling from the right sector to the left, and the positive peak was produced from particles traveling from the left to the right.

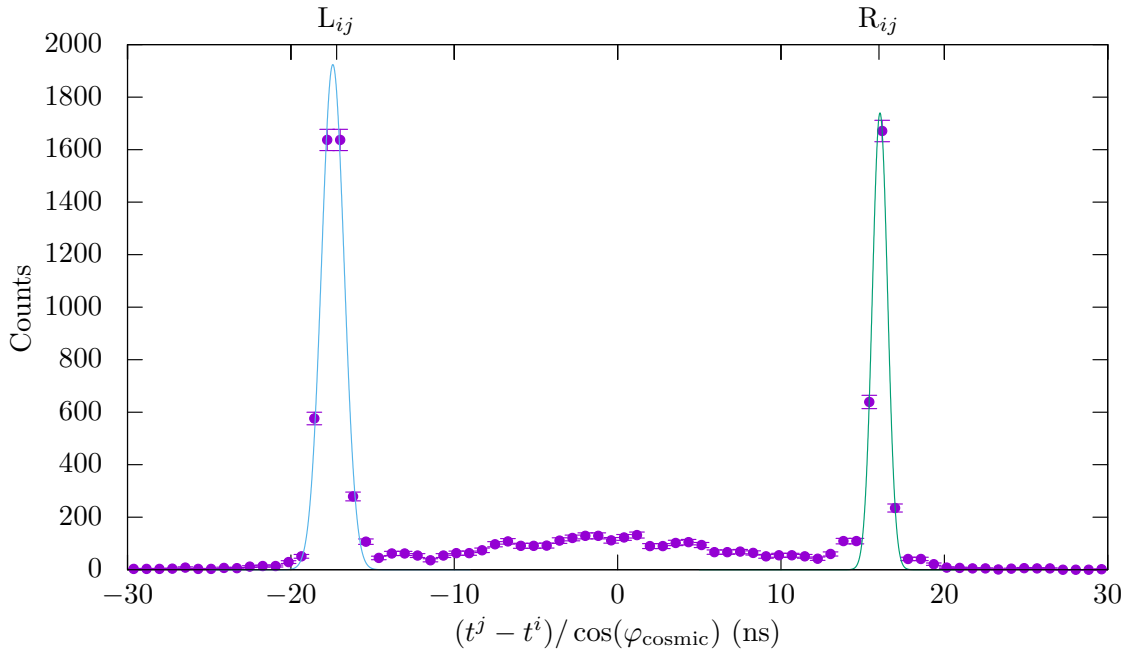

Figure 4.1: An example histogram of $(t^i_R - t^i_L)/\cos(\phi_{\text{cosmic}})$ for ToF i in the right sector and ToF j in the left sector. The peak on the left, L_{ij} was produced from cosmic rays passing from the left to the right sector and R_{ij} was from cosmic rays passing right to left.

The centroids of the two peaks were found by fitting the peaks with Gaussian distributions. The centroids are labeled as L_{ij} and R_{ij} in Figure 4.1. The mean-time offsets can be found from the peak positions as,

$$\mathrm{S}_{ij} = \frac{1}{2}\left(\mathrm{L}_{ij} + \mathrm{R}_{ij}\right) = (t_{\text{offset}})^i_R - (t_{\text{offset}})^j_L. \tag{4.7}$$

This gave $18 \times 18 = 324$ equations, from which the relative mean time offsets $(t_{\text{offset}})^{i(j)}_{R(L)}$ were extracted using a least squares minimization of Equation (4.7). Each of the equations in the least squares minimization was given a weight w_{ij} where

$$w^2_{ij} = \frac{1}{\left(\frac{\sigma^R_{ij}}{\sqrt{N^R_{ij}}}\right)^2 + \left(\frac{\sigma^L_{ij}}{\sqrt{N^L_{ij}}}\right)^2}. \tag{4.8}$$

$N^{R(L)}_{ij}$ was the integrated number of events in the peak, and $\sigma^{R(L)}_{ij}$ was equal to one standard deviation of the Gaussian fit.

The least squared minimization determined the 36 mean time offsets $(t_{\text{offset}})_R^i$ and $(t_{\text{offset}})_L^j$ relative to each other, with an undetermined global offset. The global offset was restrained by setting one ToF paddle's timing offset to zero with a very high weight. This forced all that the offsets $(t_{\text{offset}})_{R(L)}^{i(j)}$ for the remaining ToF paddles to be determined relative to the ToF paddle with the high weight. Then the global offset was determined with the method described below.

Initially the global offset was determined by matching the reconstructed mean-time in data to the Monte Carlo simulation's calculation of the average flight time for leptons. Once track reconstruction was completed, the global offset was recalculated using the flight time of leptons calculated from the momentum p, and path length L_{path}, of a track as

$$t_{\text{track}} = \frac{L_{\text{path}}}{c}\sqrt{\left(\frac{m_e}{p}\right)^2 + 1}, \tag{4.9}$$

where c is the speed of light, and m_e is the mass of the electron.

This method determined the mean time offset of each ToF relative to the others to within 0.08 ns. The global offset was determined to within 0.5 ns. The delays in the mean time were related to the $\text{TDC}_{\text{delay}}$ by

$$(t_{\text{offset}})_{R(L)}^{i(j)} = \frac{1}{2}\left[(\text{TDC}_{\text{delay}})_b^{i(j)} + (\text{TDC}_{\text{delay}})_t^{i(j)}\right] t_{\text{res}}. \tag{4.10}$$

4.1.2 Position Offsets

The time delays were different for the two PMTs on a ToF paddle because the top and bottom PMTs had different cable lengths. The time delay difference translated the reconstructed position in the ToF detectors (Equation (4.2)) vertically. Several methods used to calibrate the position reconstruction in the ToF detectors are described in this section.

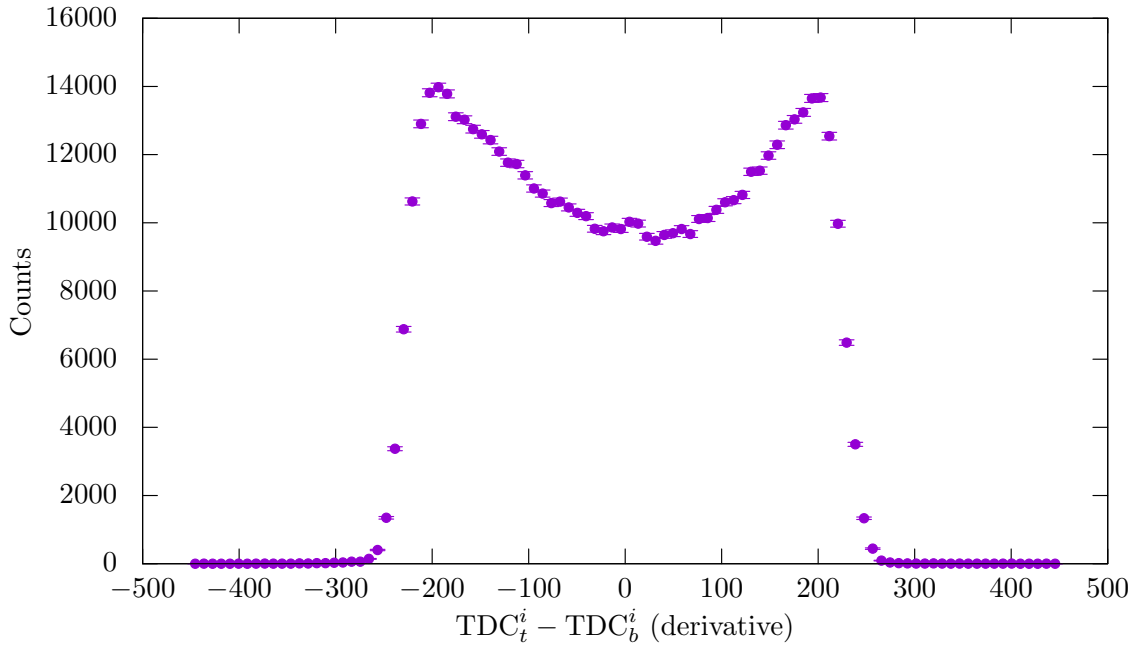

Figure 4.2: The TDC difference between the TDC values for the top and bottom PMT for a ToF paddle. This was used for the hit position calibration.

The first method looked at cosmic rays passing through a ToF paddle. A histogram of the TDC difference between the top and bottom PMT was produced for each ToF for many cosmic ray events. This produced the structure seen in Figure 4.2.

If, for ToF i, $\mathrm{TDC}_{\mathrm{delay}_t}^{\ i} = \mathrm{TDC}_{\mathrm{delay}_b}^{\ i}$, then the distribution as shown in Figure 4.2 should be centered around zero. The deviation of the center of the distribution from zero was equal to the $y_{\mathrm{offset}}^i = -\left[\mathrm{TDC}_{\mathrm{delay}_t}^{\ i} - \mathrm{TDC}_{\mathrm{delay}_b}^{\ i}\right]$. For this analysis, cosmic ray data was used because, for lepton-proton scattering data, the drift chambers prevented most particles from hitting the scintillator at the top and bottom edges of the paddle. This pushed the edges of the distribution shown in Figure 4.2 closer to the center and made the rise and fall less steep.

To find center of the distribution, the positions of the rise and fall were used. To find these positions, the absolute value of the derivative of Figure 4.2 was found and

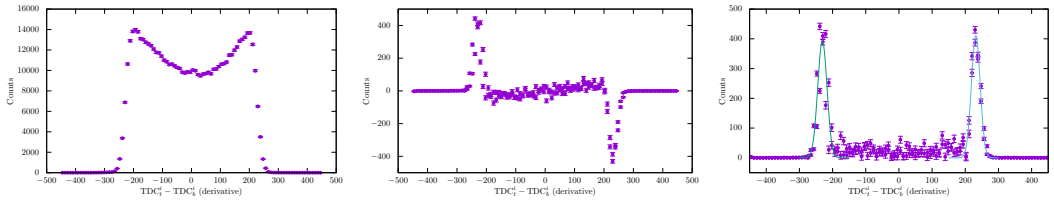

(a) Original (b) Derivative (c) Fitted

Figure 4.3: The process for finding the width and center of the TDC top-bottom difference for a ToF paddle. (a) The original TDC difference. (b) The derivative. (c) Two Gaussian functions were fitted to the absolute value of the derivative.

fitted with two Gaussian functions. This method is illustrated in Figure 4.3.

This method was originally used to get y^i_{offset} for all ToF paddles. However, because the edges of the distribution shown in Figure 4.2 were not sharp, there was an uncertainty in this measurement of approximately 5-10 channels. Another method, described next, was used to get a more precise measurement.

The second method to calibrate the hit position in the scintillator used elastic lepton-proton scattering. With elastic lepton-proton scattering, conservation of momentum restricted the scattered particles to always lie in the same plane. Using this principle, coincident hits in the left and right sectors of the detector, from elastic scattering, were used to calibrate the hit position offsets.

This calibration was completed after a preliminary track reconstruction through the drift chambers, which provided a sample of events of elastic scattering. Using this sample of elastic events and requiring that one particle passed through a scintillator on the right and the other through a scintillator on the left, the sum of the azimuthal angles defined in Equation (4.3), as calculated from the ToF hit positions, yields

$$\Delta\varphi_{ij} = \varphi^i_R + \varphi^j_L, \tag{4.11}$$

which was binned into 18×18 histograms. For coincident ToF detectors that were

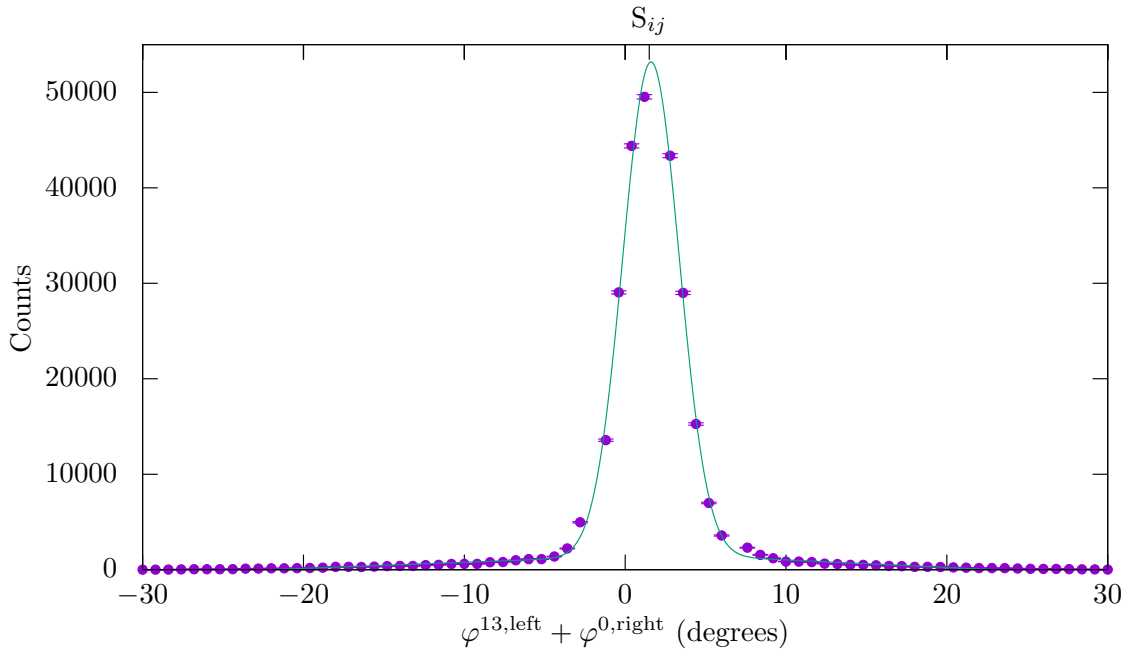

Figure 4.4: The sum of azimuthal angle φ for coincident events in the left and right sectors of the detector. This distribution allowed for the ToF position offsets to be found.

positioned at angles allowed by elastic scattering, these histograms had a Gaussian peak with a triangular background. To calibrate the offsets, the shift in $\Delta\varphi_{ij}$ to center the Gaussian at zero was calculated.

First, the position, width, and integrated number of events in the Gaussian peak was found by fitting all 18×18 histograms with a Gaussian function on top of a triangular background. The background was subtracted and the mean of the Gaussian S_{ij} was found, as shown in Figure 4.4.

The position of the peak related to the positional offsets $(t_{\text{offset}})^{i(j)}_{R(L)}$ as

$$S_{ij} = (t_{\text{offset}})^{i}_{R} + (t_{\text{offset}})^{j}_{L}. \tag{4.12}$$

The offsets were then found using the least squares minimization method, which used much of the same code as the mean time offsets. A weighting was incorporated from

the width σ_{ij} and the integrated number of events in the Gaussian peak N_{ij} as

$$w_{ij} = \sqrt{N_{ij}}/\sigma_{ij}. \tag{4.13}$$

For coincident ToF bars with left-right combinations not permitted with the kinematic relations of elastic scattering, only the triangular background was used in the fit and were given a weight of zero in the minimization. The least-squares fit returned the position offsets, relative to each other. An overall offset was needed to complete the calibration. To find the overall offset, elastic lepton-proton scattering was used where the lepton was scattered into the 12° telescope. The position in the 12° telescopes had an independent positional measurement, and therefore provided an overall offset.

The calibration from lepton-proton scattering generally returned more precise positional offsets. However, the uncertainties in the positional offsets for five ToF bars were found to be large because of strange structure in some of the ToF bars in the left sector. The distribution for the sum of azimuthal angles (Figure 4.4) revealed a double Gaussian distribution for five ToF bars in the left sector. The source of the second Gaussian peak was never identified, although it could have been a result of damage in the scintillator or unidentified issues with the electronics.

4.1.3 Speed of Light in the Scintillator

To get the speed of light in the scintillator, the same calibration as the hit position offset from cosmic ray data was used. The width of the distribution in Figure 4.2 should be equal to $2L/v_{sc}$, where v_{sc} was the speed of light in the scintillator in mm per TDC channel and L was the length of the scintillator. Since the scintillator length was known, the speed of light in the scintillator was calculated from the difference in the peaks as shown in Figure 4.3c. This method provided the speed of light in the

scintillator to within an uncertainty of 4 to 10 μm per TDC channel for most ToF bars. Figure 4.5 shows the measured hit position along the ToF bars for cosmic data, before and after the calibration.

4.1.4 Energy Deposition

The energy deposited in the scintillator was estimated from the integral of the PMT pulses digitized by the analog-to-digital converters (ADC) for the top and bottom PMTs. Other information needed to calculate the energy deposited in the scintillator were the ADC pedestals, the PMT gains, and the scintillator attenuation length.

When a particle passed through the active region of a ToF paddle (i.e., the plastic scintillator element) scintillation light was emitted. The light was transmitted through the scintillator and light guides to the PMT windows. As the light was transmitted through the scintillator, the intensity of the light N was attenuated, characterized by a factor given as a reduction of the intensity $1/e$ for a characteristic distance ℓ, called the attenuation length. The attenuation length varied significantly from bar to bar and along the length of the scintillator. The intensity of light which reached the top PMT window was parameterized as

$$(N_{\text{atten}})_t^i = f^i N e^{-\left(\frac{L^i}{2} - y^i\right)/\ell^i}, \tag{4.14}$$

where f^i is the fraction of the light that was transmitted towards the top PMT and $\left(\frac{L^i}{2} - y^i\right)$ was the distance between hit position of the particle and the top of the scintillator. Similarly the intensity of light at the bottom PMT was parameterized as

$$(N_{\text{atten}})_b^i = \left(1 - f^i\right) N e^{-\left(\frac{L^i}{2} + y^i\right)/\ell^i}. \tag{4.15}$$

The integrated ADC pulse as recorded by the PMTs was related to N_{atten} by the

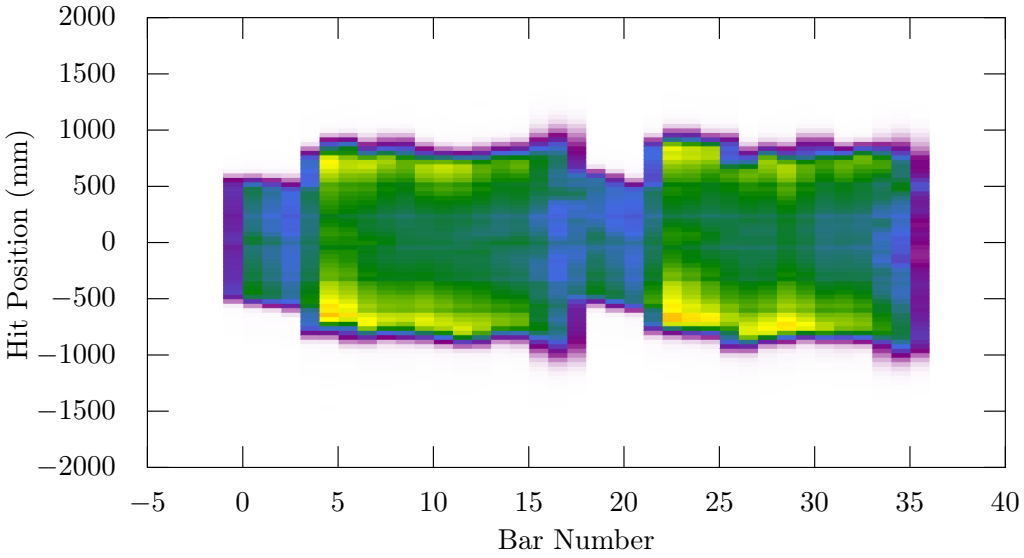

(a) Before the calibration

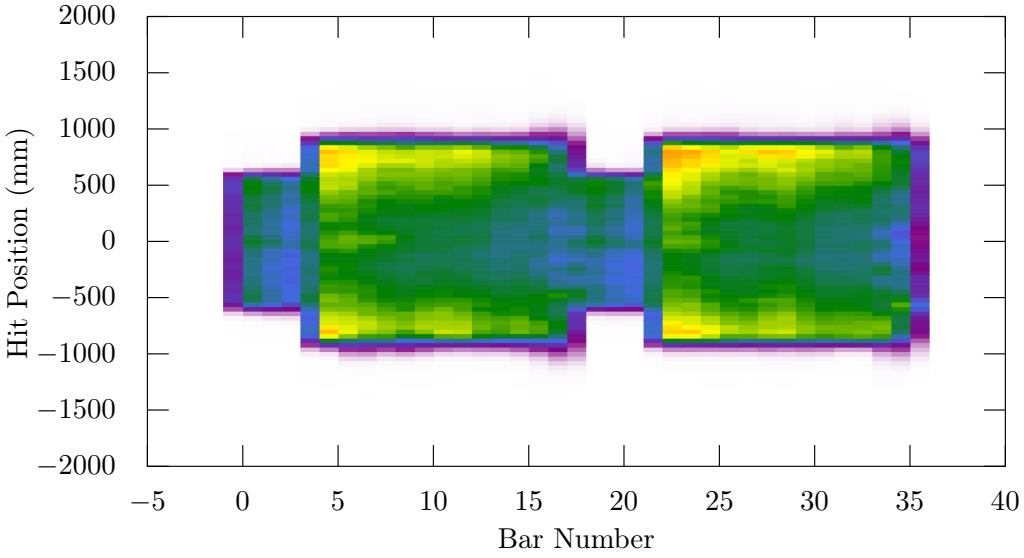

(b) After the calibration

Figure 4.5: The calibrated speed of light in the scintillator using cosmic ray events.

PMT gain $G_{t(b)}$ and the ADC pedestal height $\mathrm{ADC}_{\mathrm{ped}}$ as

$$\mathrm{ADC}_t^i = (N_{\mathrm{atten}})_t^i \, G_t^i + (\mathrm{ADC}_{\mathrm{ped}})_t^i \,, \tag{4.16}$$

for the top PMT and

$$\mathrm{ADC}_b^i = (N_{\mathrm{atten}})_b^i \, G_b^i + (\mathrm{ADC}_{\mathrm{ped}})_b^i \,, \tag{4.17}$$

for the bottom PMT.

Both the PMT gains and the attenuation length were determined from data. Assuming a linear relationship between the intensity of scintillation light N and energy deposited in the scintillator material, the energy deposited was estimated.

4.1.5 Pedestal Offsets, Gains, and Thresholds

For the energy deposited in the scintillator to be calculated, factors that characterized the response of the PMT and ADC electronics (such as the ADC pedestal height, the PMT gain, and the discriminator thresholds) needed to be known. Details on these calibrations are in (Russell, 2016).

The ADC pedestal height $\mathrm{ADC}_{\mathrm{ped}}$ defined as the base ADC value when the PMT was not emitting a pulse, was recorded during data taking for each PMT, and the mean and standard deviation (in channels) were saved in the raw data.

The gain calibration, in addition to the PMT gain, accounted for the intensity of light output as a function of the energy deposited in the scintillator. While, the gain in the PMT was assumed to be linearly related to the light that reached the PMT windows, the scintillator light output was not a linear function of the energy deposited due to recombination and quenching effects in the scintillator, which were accounted for using an empirical formula, as described in (Russell, 2016).

The top/bottom relative PMT gain matching was done by requiring that half of the energy deposited in the scintillator went to each PMT, $f^i = 0.5$. Using Equations

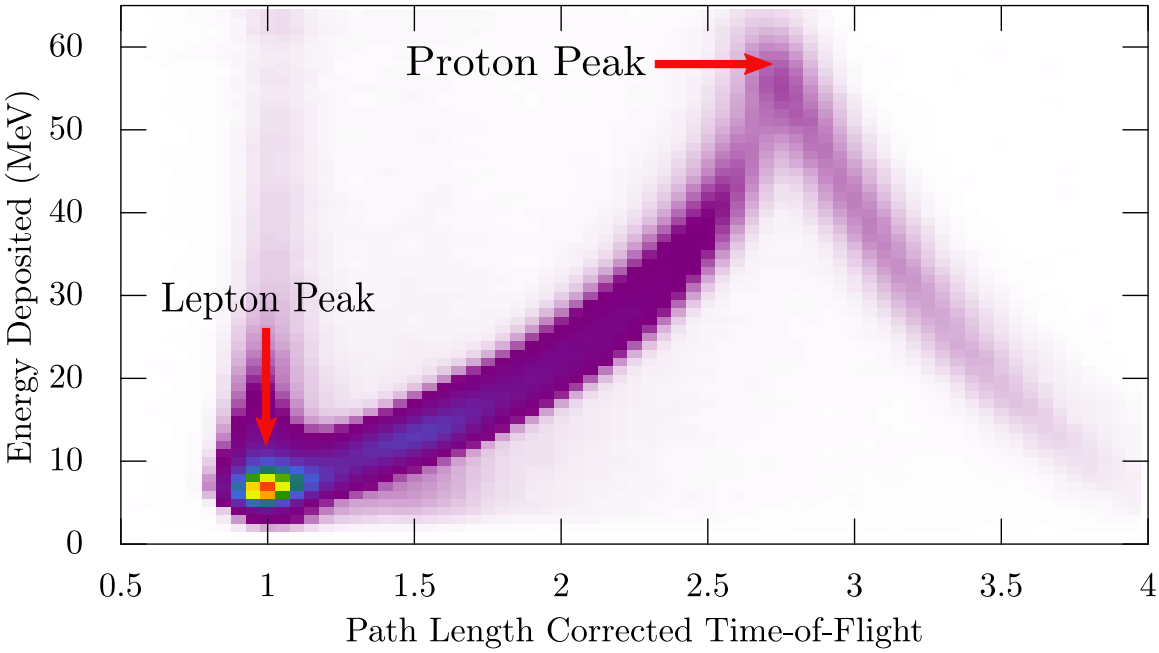

Figure 4.6: The energy deposited in the ToF bar as a function of the path length corrected time-of-flight ct^i/L^i.

(4.14) and (4.15), f^i was found as

$$f^i = \frac{(\mathrm{N}_{\mathrm{atten}})_t^i}{(\mathrm{N}_{\mathrm{atten}})_t^i + (\mathrm{N}_{\mathrm{atten}})_b^i} = \left(1 + \frac{G_b^i}{G_t^i}\frac{[ADC - ADC_{ped}]_t^i}{[ADC - ADC_{ped}]_b^i}\exp\left(-2y^i/\ell^i\right)\right), \quad (4.18)$$

where the attenuation length ℓ was assumed to be constant along the bar for this calibration. From this expression, the ratio of G_b to G_t for each ToF bar was extracted.

The absolute gain was estimated by matching the data to a Monte Carlo simulation. Figure 4.6 shows the energy deposited in the ToF bar as a function of the mean time of the particle. For the gain calculation, the proton peak was used because that peak was the most distinguishable feature of the distribution. The values used for the gains of the ToF detectors were adjusted until the energy peak of the proton distribution from data matched that of the Monte Carlo. The gains were found to change throughout the data taking period, requiring that this calibration was done multiple times.

The thresholds for the discriminators were found using a trigger that required a coincident ToF signal (from both the top and the bottom PMT) in one sector, but only one PMT signal in the other sector. This trigger was primarily used for calibration purposes and was significantly pre-scaled during data taking. Events that fired this "3/4 trigger" provided the data required to find the thresholds for the ToFs where only one PMT signal had been required for the trigger. For these events, the fraction of events where both ToFs had a valid TDC signal as a function of ADC was measured. This produced a step function near the ADC value of the threshold.

4.1.6 Attenuation Length

The ToF detectors were previously used for the BLAST experiment, and showed signs of aging caused by radiation damage, surface damage, and structural stress from moving. The main sign of the degradation of the scintillator was a shortened attenuation length, which varied significantly along the length of the ToF paddle. Allowing for the attenuation length to vary along the ToF bar $\ell \to \ell(y)$, Equations (4.14) and (4.15) become

$$(\mathrm{N}_{\mathrm{atten}})^i_t = f^i \mathrm{N} \exp\left(- \int_{y^i}^{\mathrm{L}^i/2} \frac{dx}{\ell(x)^i} \right), \tag{4.19}$$

and

$$(\mathrm{N}_{\mathrm{atten}})^i_b = \left(1 - f^i\right) \mathrm{N} \exp\left(- \int_{-\mathrm{L}^i/2}^{y^i} \frac{dx}{\ell(x)^i} \right). \tag{4.20}$$

By assuming that half of the light was transmitted towards the top PMT, $f^i = 0.5$, the ratio of Equations (4.19) and (4.20), gave the integral of the attenuation length as a function y^i of the hit,

$$\ln\left(\frac{(\mathrm{N}_{\mathrm{atten}})^i_t}{(\mathrm{N}_{\mathrm{atten}})^i_b} \right) = - \int_{-\mathrm{L}^i/2}^{\mathrm{L}^i/2} \frac{dx}{\ell(x)}. \tag{4.21}$$

Because the attenuated intensity could be found from data using Equations (4.16) and (4.17), this allowed for the attenuation lengths to be found from data. By binning

$$\ln\left(\frac{(\mathrm{N}_{\mathrm{atten}})_t^i}{(\mathrm{N}_{\mathrm{atten}})_b^i}\right) = \ln\left(\frac{\left[\mathrm{ADC}_t^i - (\mathrm{ADC}_{\mathrm{ped}})_t^i\right] G_b^i}{\left[\mathrm{ADC}_b^i - (\mathrm{ADC}_{\mathrm{ped}})_b^i\right] G_t^i}\right) \tag{4.22}$$

as a function of y^i over many events for each ToF bar and fitting with a polynomial function, $\ell(y^i)$ was found. The attenuation length measured with this method was found to be as low as 110 cm for some paddles. More detail on the attenuation length analysis method and results can be found in (Russell, 2016).

4.2 Drift Chambers

The drift chambers in OLYMPUS provided the information needed to reconstruct the trajectories of particles traversing through the detector from the target. From these trajectories (or "tracks"), the original scattering event was reconstructed. Processing raw drift chamber TDC signals into full tracks, a multi-step reconstruction process was used. First, the electron drift time was reconstructed from the wire TDC signal. The drift time was the time difference between the time when a track traversed a cell and ionized the chamber gas, and the time that the electrons from the ionization reached a sense wire. The drift time calculation included a wire time offset from TDC delays and the time for the scattered particle to travel from the interaction vertex in the target to a cell in the drift chambers. In the next step of the process, the between the track and the sense wire was calculated from the measured electron drift time, This was called the time-to-distance (TTD) and was a function of the electric and magnetic fields in the cell and gas properties. This provided a two-dimensional hit position of the track in each sense wire plane. The last step of the process used all the hit positions to reconstruct the particle trajectory. This section discusses the steps of this process.

From the signals of the six drift chambers, the trajectories of the scattered particles were reconstructed. The reconstructed tracks provided information on the initial interaction vertex, polar and azimuthal scattering angles, and the momentum from the curvature of the trajectory in the magnetic field.

As a charged particle passed through the drift chambers, each charged particle intersected with 18 planes of sense wires and, assuming ideal efficiencies, the tracks were reconstructed from 18 sense wire timing signals. As each charged particle passed through the gas in the drift chambers, the transit of the particle ionized the argon, producing electron-ion pairs. The ionization electrons, responding to the electric field produced by the field wires, drifted toward the closest sense wire. Close to the sense wire, the signal was amplified by the high electric field surrounding the sense wire, producing an electron cascade. The cascade, upon contact with the sense wire, produced a signal that then traveled down the sense wire to the readout electronics. The TDC distribution for events on typical a sense wire is shown in Figure 4.7. Because the drift chambers operated in common-stop mode, the highest TDC channel corresponded to the shortest drift time. Similar to the ToF TDC signals, there was an inherit unknown offset for the wire TDC signals that needed to be determined before meaningful timing information could be extracted from the detector.

4.2.1 Drift Chamber Timing Calibration

The TDC signals, corrected for delays caused by electronics, cables, and flight time for the particles, provided the drift time for the ionization electrons in the gas. By knowing the drift time of the ionization electrons, a one-dimensional hit location in the wire plane could be reconstructed. The drift time t_{drift} was calculated from the raw TDC with the relationship

$$t_{\text{drift}} = \left[t_{\text{ref}} + t_0^i - (\text{TDC}_{\text{raw}}{}^i)\right] C_{\text{ch}} - t_{\text{w}}^i(t_{\text{ToF}}). \tag{4.23}$$

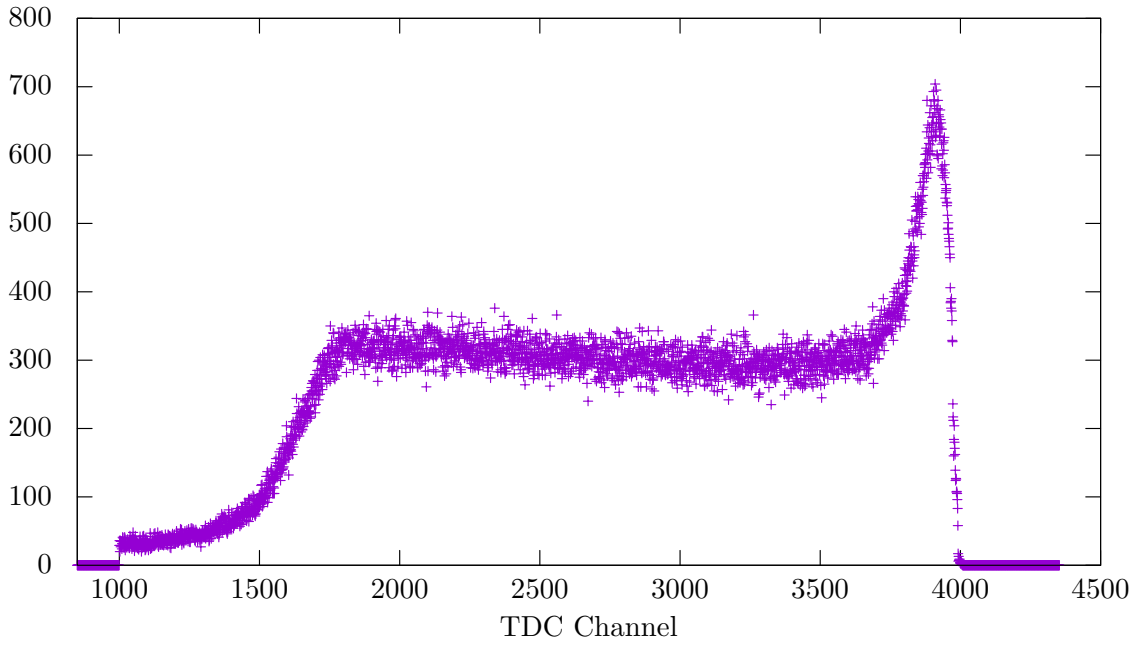

Figure 4.7: The TDC distribution from one wire. Because the drift chambers operated in common-stop mode, the largest channel time corresponded to the earliest signal time.

The ToF detectors provided the reference time t_{ref}, and C_{ch} was the TDC channel time, given in μs per TDC channel. The overall offset caused by the readout electronics, cables, and trigger time was t_0. The parameter $t^i_{\text{w}}(t_{\text{ToF}})$ was an estimate of the time for the particle to travel from the interaction region to the wire, based on the ToF information.

The timing offsets,t^i_0 for each wire were determined from data by fitting the trailing edge of the TDC spectra produced by particles traversing the chambers (Figure 4.7). The trailing edge of the spectra corresponded to high-energy leptons that passed close to the wire, minimizing the drift time of the resulting ionization electrons to reach the sense wire.

The edge of the spectra gave the offsets from electronics and cables, but only accounted for the time needed for a high-energy lepton to traverse from the interaction

point to the wire, since these were the fastest charged particles. A strong correlation was found between the ToF time and the time-to-wire for particles, as shown in Figure 4.8, which shows Monte Carlo simulations for the time-to-wire as a function of the corresponding ToF mean-time. For simulated protons, Figure 4.8b shows a strong linear correlation between the wire time and the ToF mean time.

The linear relationship between wire-time and ToF mean-time provided a way to account for the time needed for a charged particle to reach a wire plane from the target. For each sense wire, Monte Carlo simulated prediction for the wire time as a function of ToF mean time was binned into a histogram. These histograms were linearly fit to find the function $t_{\mathrm{w}}(t_{\mathrm{ToF}})$, and the resulting slope and intercept were saved. For each track, the drift time t_{drift} was corrected by the time-to-wire calculated from the ToF mean-time.

4.2.2 Time-to-Distance Calibration

From the corrected TDC time for a drift chamber wire, the distance the track passed with respect to that wire was found using a time-to-distance (TTD) function. This function mapped the time for ionization electrons to drift from the point of ionization to a sense wire. For each wire, there were two TTD functions; the first describing drift times from tracks that passed upstream of the sense wire and the other from tracks that passed downstream of the sense wire. The TTD functions were dependent on the electric and magnetic fields in the cell, the gas properties, and the angle of the track with respect to the wire plane. The electric field was calculated from the field and sense wire positions and voltages, and the magnetic field strength in the cell was taken from the field maps described in Section 3.3.1.

The function used to fit the TTD for each cell was required to be continuous and consisted of three functions. The electric field strength was constant throughout

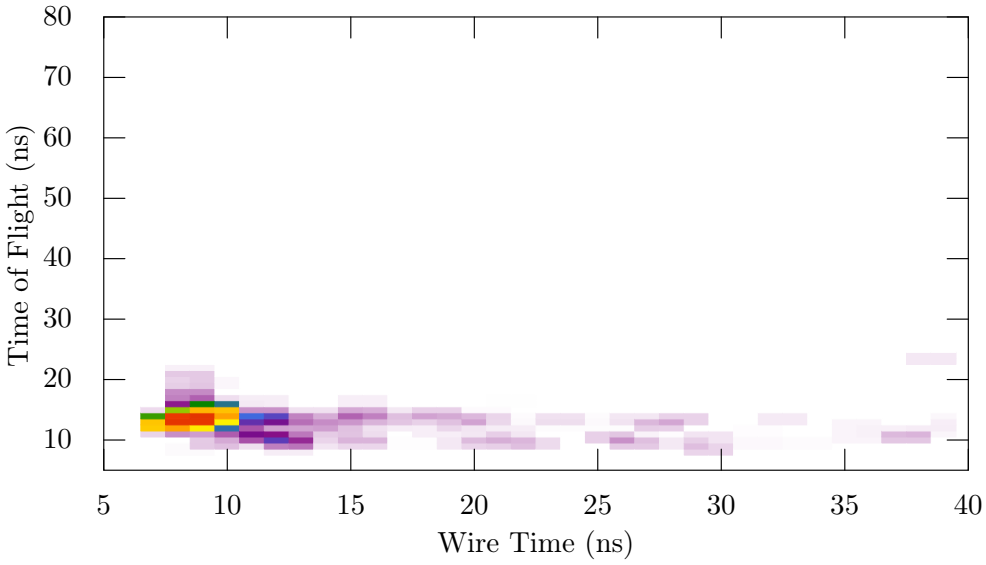

(a) Monte Carlo electrons

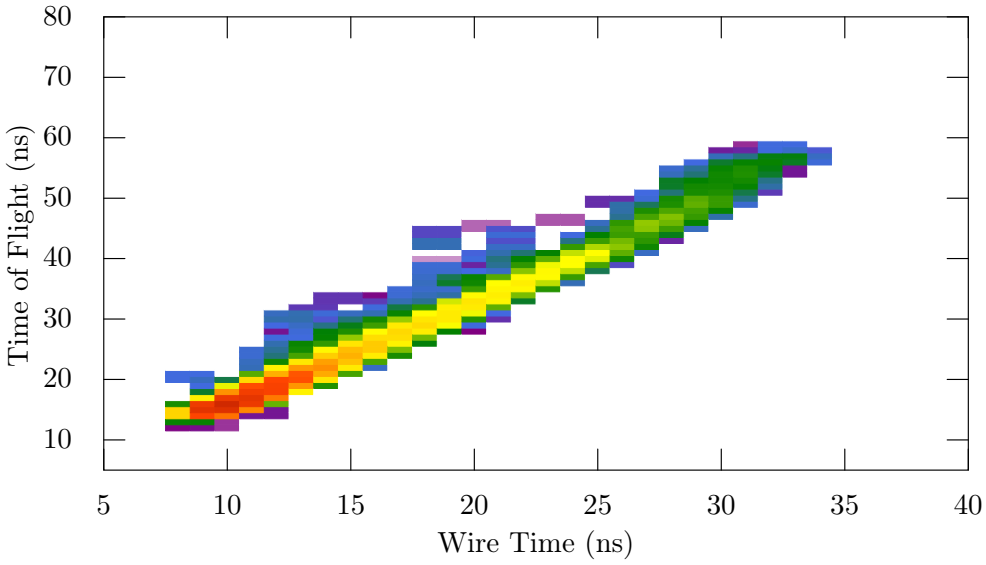

(b) Monte Carlo protons

Figure 4.8: Monte Carlo time-to-wire verses the time-of-flight to the ToF bars for leptons and protons.

most of the cell, corresponding to a linear TTD function. In close proximity to the sense wires, the large electric field increased the drift speed significantly and was better modeled with a cubic function. The small electric field near the ground planes corresponded to a steeper linear TTD function. The functions were allowed to vary with the track azimuthal angle φ to account for TTD changes along the wires.

The TTD function was found by iterative fitting to tracked data. This method allowed the effects of imperfections in the wires, field and gas changes, and edge effects to be included in the fit. Because the ethanol mixture varied during data taking, the data was first grouped by length of the TTD function. This was done by looking at the width of the TDC distribution shown in Figure 4.7. The TTD functions for each group were then estimated using Garfield, (Veenhof *et al.*, 1993), a Monte Carlo simulation of gaseous detectors. Garfield modeled the electron drift in the chamber taking into account the electric and magnetic fields and used a program (Magboltz, 2002) that calculated the Boltzmann transport equations for electrons in gas mixtures. With the Garfield TTD functions, the track reconstruction software returned a large number of possible track candidates. After removing poorly reconstructed tracks, the TTD functions were adjusted to minimize the difference between the distances found from the TTD and the returned track. Then the procedure was repeated with the new TTD functions until no significant improvement was seen. For most wires, only two iterations were needed before the results converged. These fits are described in (Schmidt, 2016).

4.3 Track Reconstruction

From the hit positions in the wire planes, the tracks were reconstructed. The tracks provided the kinematic information necessary to select elastically scattered $e^- p$ and $e^+ p$ events as a function of Q^2.

Reconstructing the tracks through the drift chambers proved to be very challenging for several reasons.

1. A significant amount of noise existed in the drift chambers. This noise included both random electronic noise and a large background of low energy lepton tracks. The inner drift chambers had the most noise. A scattering event is shown in Figure 4.9 using the event display software, and illustrates the large amount of noise in the chambers.

2. The low magnetic field caused high momentum leptons to traverse the drift chambers with very little curvature. At particular angles, the tracks did not have any cell-crossings where the track would enter two cells in a layer. For such events, resolving whether the tracked passed to the left or right of a sense wire column was difficult.

3. The small Lorentz angle made the staggering in the sense wires insufficient to resolve the ambiguity between a track passing upstream or downstream of a sense wire column. The left-right ambiguity posed a significant problem, as an incorrect left-right decision could significantly change track parameters, particularly the momentum. At certain angles, where a track at high momentum had very low curvature, distinguishing between electrons and positrons was difficult.

4. The track reconstruction software had to run fairly quickly to allow for the TTD to be found iteratively.

To overcome these challenges, several approaches were taken. The first was a software program was written that provided quick maps between track parameters and hit positions in the drift chambers and ToF detectors. Second, a pattern matching

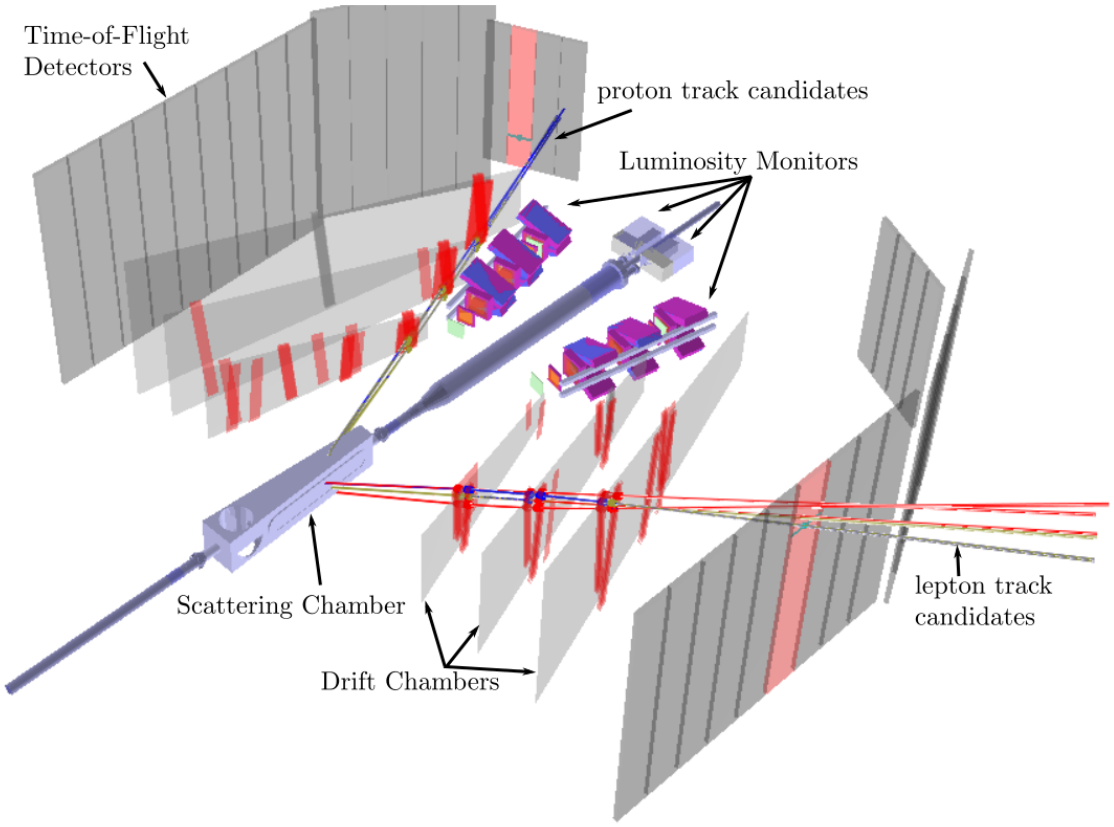

Figure 4.9: An event display image of a typical elastic electron-proton scattering event. There are several track candidates shown.

algorithm based on (Dell'Orso and Ristori, 1990) cut down on noise events in the data. Finally, to reconstruct the tracks while solving the left-right ambiguity, an algorithm based on the elastic arms method described in (Ohlsson *et al.*, 1992) and (Ohlsson, 1993) was used.

4.3.1 The Fast Track Algorithm

The first step in reconstructing the tracks from wire chamber and ToF hits was to correlate the kinematic track parameters – θ, φ, and z-vertex, and momentum p – to a trajectory through the complex magnetic field and detector. The trajectory of each particle was written as $\vec{\pi} = (\theta, \varphi, z, p)$.

A variable change of the track parameters was made to simplify the mapping from $(\theta,\varphi,z,p) \rightarrow (p0,\ p1,\ p2,\ p3)$. While the change of parameters is not critical to this discussion, it is important to note that the momentum parameter $p3$ was defined so that the trajectory of the particle could transition smoothly from electrons to positrons through straight tracks. This was done by making $p3 < 0$ for negatively charged particles, $p3 > 0$ for positively charged particles, and $p3 = 0$ for particles with zero charge or infinite momentum.

To map the kinematic parameters to hit positions in the drift chambers and the ToF detectors, Geant4 and Geant4e, (Agostinelli *et al.*, 2003), were used. Simulated leptons (e^+ and e^-) and protons were generated for the full kinematic range of θ, φ, vertex position z, and momentum p from 200 MeV/c up to infinite momentum (straight tracks). Using Geant4, the horizontal hit positions in the 18 wire planes and the ToF plane in each sector were output. Four-dimensional cubic splines were fit through these hit positions, and their derivatives and coefficients were saved into a database. Running the Geant4 path "swimming" simulation was CPU- and time-intensive. Saving the spline coefficients into a library provided a quick reference during the track reconstruction, significantly speeding up the track reconstruction and allowing for the iterative TTD approach.

Output from this "fast track" algorithm included the cubic spline coefficients for the following parameters for each sector:

- 18 horizontal positions in each wire plane
- 4×18 first derivatives in θ, φ, z vertex, and momentum
- 10×18 second derivatives
- 2 (vertical and horizontal) hit position in ToF plane

- 4×2 first derivatives in ToF plane
- 10×2 second derivatives in ToF plane
- The total path length from target to ToF plane

Using the saved coefficients, initial track parameters $\vec{\pi}$ could be quickly mapped to hit positions in the drift chambers and ToF detectors.

4.3.2 Pattern Matching

Before running the data through the computationally-intensive track reconstruction software, the data were trimmed of noise and background events using a Monte Carlo pattern matching algorithm. Using this algorithm, events which included hits corresponding to elastically scattered particles were selected for track reconstruction, and noise events discarded. This pruning of events increased the speed of the track reconstruction and increased the signal to noise ratio of tracks.

The Monte Carlo pattern matching algorithm was based on (Dell'Orso and Ristori, 1990), which used a tree structure to store and search the pattern data quickly. For this algorithm, a pattern was defined as any combination of drift chamber and time-of-flight signals that corresponded to a particle originating in the target and traversing through the detector. To produce all drift chamber and ToF signal combinations, the Monte Carlo simulation of the detector was used. Simulated events for leptons, pions, and protons scattering for all kinematic and vertex position ranges were propagated through the detector simulation, using Geant4 and the measured magnetic field maps. The pattern of drift chamber cells and ToF paddles that registered a hit were stored as a 180-character bitset in a pattern bank organized into a tree structure. With this tree structure, patterns were organized into increasing spacial resolution with increasing depth. Before track reconstruction, the events were matched to patterns

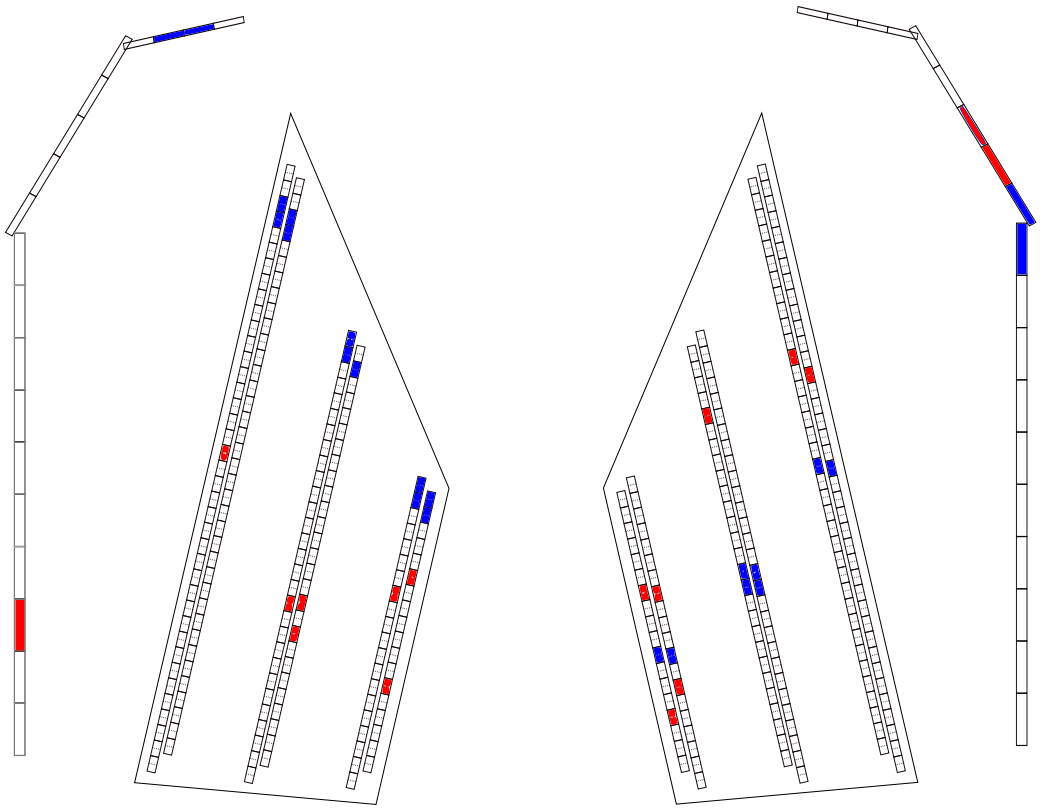

Figure 4.10: A diagram showing the signals from an event in the drift chambers and the time-of-flight detectors. For the cells that are blue or red, at least one wire in the cell recorded a signal for this event. The cells in blue are those that matched with a Monte Carlo pattern, where those in red were not. The signals that were successfully matched to Monte Carlo patterns are sent to track reconstruction and the others are discarded.

in the pattern bank with a tree search. If an event had hits which matched one or more patterns, these hits were sent to the track reconstruction, and all other hits were discarded. The pattern search was modified to include events with missing hits to account for imperfect efficiencies in the detector.

The signals produced by the drift chambers and the ToF for a typical data event are shown in Figure 4.10. The signals that were successfully pattern matched are

shown in blue, while the rejected hits are shown in red. For the final track reconstruction of the data, only events which matched patterns in both detector sectors and matched elastic kinematics were tracked. This significantly reduced the number of events that needed to be reconstructed, decreasing the time needed to analyze the full data set.

4.3.3 Elastic Arms Algorithm

The tracks were reconstructed from the hit positions in the wire planes, which were calculated from wire TDC times and the time-of-flight signals. Because of the left-right ambiguity of each hit and the high number of noise events in the wire chambers, a complex approach was taken to reconstruct the track, called the Elastic Arms Algorithm (EAA), by (Ohlsson *et al.*, 1992). Using this method, an elastic arm, or track as defined from the fast track database $\vec{\pi}(\theta, \varphi, z, p)$ was laid in each sector of the detector. These arms were given freedom to vary θ, φ, z and p so as to minimize the sum of the distances between hits in the detector and the track intersections with the wire and ToF planes.

Minimizing the sum of the distances was done by defining an energy function, of which the minimum corresponded to the best fitted track. The energy function was written as,

$$E\left(\{s_{hw}|S_w\}, \vec{\pi}\right) = \sum_{w=1}^{N_w} \left[S_w \sum_{h=1}^{N_{hw}} s_{hw} M_{hw}(\vec{\pi}) + \lambda (S_w - 1)^2 \right], \tag{4.24}$$

where the square distance $D_{hw}(\vec{\pi})$ between a hit h in the plane of wire w and the arm $\vec{\pi}$ was

$$M_{hw}(\vec{\pi}) = \left(D_{hw}(\vec{\pi})\right)^2. \tag{4.25}$$

In Equation (4.24), N_w was the number of wires with valid TDC hits that were

returned from the pattern matching. For each TDC time recorded on a wire, there were two hits, one for the left side of the wire and one for the right side of the wire. Some wires had multiple TDC signals, which would add more hits. The total number of hits on a wire was N_{hw}.

Because of the noise in the drift chambers, it was advantageous to allow for some wires to be excluded from the energy function. Whether a wire with a valid TDC signal was included in the energy function was given by

$$S_w = \begin{cases} 1 & : \text{if wire } w \text{ is assigned to the arm } \vec{\pi}, \\ 0 & : \text{otherwise.} \end{cases} \tag{4.26}$$

If a wire returned from the pattern matching was excluded from the energy function entirely, an energy penalty of units length λ was added in the energy function. The parameter λ was calibrated so that, for $\lambda > M_{hw}$, the energetically favorable decision was to discard that wire and all of its hits. Therefore λ also regulated the number of noise hits that the algorithm allowed for; if there was a lot of noise in the data, λ was set to be small.

The binary function that selected which hit on a wire was used in the energy function, given $S_w = 1$ was

$$(s_{hw}|S_w) = \begin{cases} 1 & : \text{ if hit } h \text{ on wire } w \text{ is assigned to } \vec{\pi}, \\ 0 & : \text{otherwise.} \end{cases} \tag{4.27}$$

There was no penalty for rejecting hits from a wire unless all the hits were rejected. For the final energy function, only one hit per wire was included in the energy function, chosen to minimize Eq (4.24).

The projected horizontal and vertical track positions in the time-of-flight planes provided the information necessary to extend Equation (4.24) to the ToF detectors.

The fast track algorithm returned the projected vertical hit position $y_{\mathrm{Tr}}(\vec{\pi})$ in mm from the xz-plane. The vertical position was then corrected for any vertical shifts in

the ToF positions, as measured with the detector survey, so that a track that went directly through the center of a ToF bar returned $y_{\mathrm{Tr}}(\vec{\pi}) = 0$.

The horizontal ToF position projection $x_{\mathrm{Tr}}(\vec{\pi})$ was given from the fast track algorithm in unit-less numerical values that corresponded to bar number, where the integers corresponded to the horizontal center of the ToF paddle. For example, if a track went through the ToF plane where ToF bar 3 was positioned, the fast track algorithm returned a value $x_{\mathrm{Tr}}(\vec{\pi}) \in (2.5, 3.5)$, where $x_{\mathrm{Tr}}(\vec{\pi}) = 2.5$ corresponded to the track passing through the most downstream horizontal position of ToF 3, and $x_{\mathrm{Tr}}(\vec{\pi}) = 3.5$ the most upstream horizontal position of ToF 3.

All the hits in the drift chambers were weighted evenly, meaning the probability of including a wire depended only on the metric M_{hw}. The ToF bars were weighted relative to the wire hits with w_b corresponding to the weight of the ToF bar hit, and w_y corresponding to the vertical hit position on the ToF. Because the positions of the ToF bars in the detector were known to high precision from the survey, w_b was set to be high, which limited the θ range for the track. There was relatively large uncertainty in the reconstructed ToF hit position y_{ToF}, which corresponded to a small w_y. The hit position weight also was calibrated bar-by-bar to account for variances in the uncertainties in the ToF time delays.

Adding the ToF detectors into the energy equation, the metric was calculated, for ToF bar b as

$$M_b(\vec{\pi}) = w_b[\Delta x]^2 + w_y[\Delta y]^2 \tag{4.28}$$

where

$$\Delta y = y_{\mathrm{Tr}}(\vec{\pi}) - y^b_{\mathrm{ToF}}, \tag{4.29}$$

and

$$\Delta x = \begin{cases} x_{\mathrm{Tr}}(\vec{\pi}) - (b - \frac{1}{2}) & : x_{\mathrm{Tr}}(\vec{\pi}) - b < \frac{1}{2}, \\ 0 & : |x_{\mathrm{Tr}}(\vec{\pi}) - b| \leq \frac{1}{2}, \\ x_{\mathrm{Tr}}(\vec{\pi}) - b + \frac{1}{2}) & : x_{\mathrm{Tr}}(\vec{\pi}) - b > \frac{1}{2}. \end{cases} \tag{4.30}$$

This resulted in the modified energy equation,

$$E\left(\{s_{hw}|S_w\}, \vec{\pi}\right) = \sum_{w=1}^{N_w} \left[S_w \sum_{h=1}^{N_{hw}} s_{hw} M_{hw}(\vec{\pi}) + \lambda (S_w - 1)^2 \right] + \sum_{b=1}^{N_{\mathrm{ToF}}} M_b(\vec{\pi}). \tag{4.31}$$

There was no penalty for rejecting ToF hits from a track except in the case all ToF hits were rejected. If all ToF hits were excluded from the track, the assessed penalty was almost infinite.

The ToF weights were originally found using the Monte Carlo simulation. Many simulated tracks were reconstructed using the tracking software over a range of w_b and w_y. The tracks that fell within three standard deviations of the true value were considered correctly reconstructed. The ToF weights were adjusted to maximize the percentage of correctly tracked Monte Carlo tracks. The results from the ToF weight scans are shown in Figure 4.11.

This scan produced reliable results for w_b, but did not accurately reproduce the uncertainty in the reconstructed hit position in the ToF bars. Small deviations in the reconstructed hit positions stemmed from uncertainty in the ToF timing delays. Setting w_h to be large originally caused issues with the TTD calibrations. Lowering w_h resolved this issue.

The modified energy equation produced an energy landscape with many minima; for a perfect track where all 18 wires hit, there were 2^{18} minima. Searching all minima for the global minimum was combinatorically very difficult. A way to avoid searching all of the minima for the global minimum was to introduce noise, as simulated thermal noise, into the system. This was done with a procedure called simulated

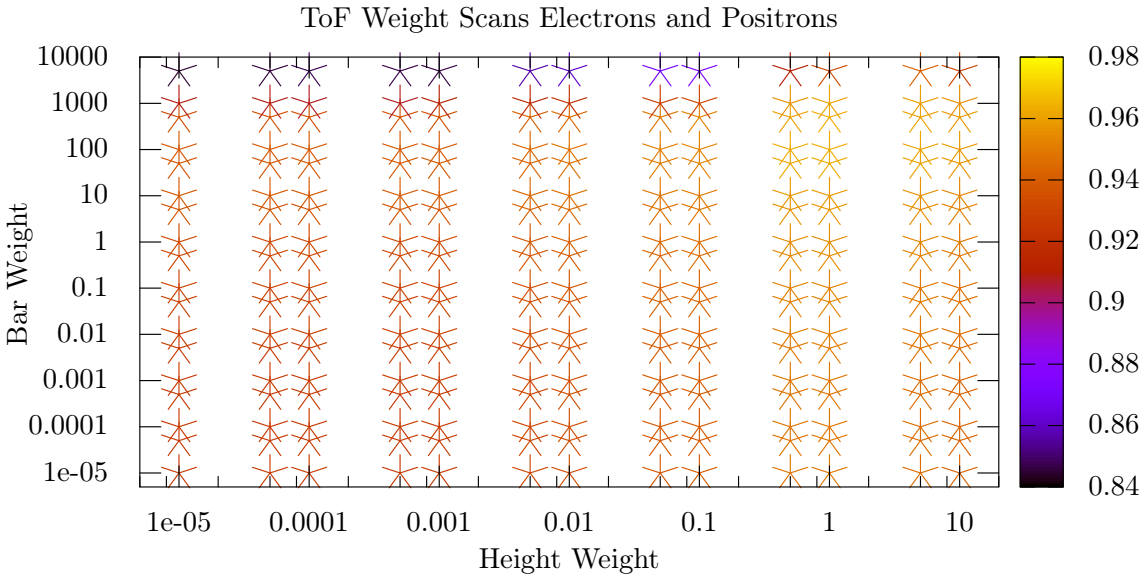

Figure 4.11: Scans of the weights for including the ToF detectors in the track reconstruction. The x- and y-axes are the weights (unit-less parameters) and the color scale is the percentage of correctly reconstructed Monte Carlo tracks. A weight equal to unity would weight the ToF parameters equal to a wire hit.

annealing, where thermal noise was introduced into the energy equation according to the Boltzmann distributions as

$$P\left(\{s_{hw}|S_w\},\vec{\pi}\right) = \frac{1}{Z}e^{-\beta E(\{s_{hw}|S_w\},\vec{\pi})}, \tag{4.32}$$

where $\beta = 1/T$, which regulated the amount of thermal noise in the system; and Z was the usual partition function. Summing over all configurations of s_{hw}, the marginal probability distribution was

$$\begin{aligned} P_M(\vec{\pi}) &= \sum_{s_{hw}} P\left(\{s_{hw}|S_w\},\vec{\pi}\right) \\ &= \frac{1}{Z}e^{-\beta E_{eff}(\vec{\pi})} \end{aligned} \tag{4.33}$$

where $E_{eff}(\vec{\pi})$, the effective energy function, was defined as

$$E_{eff}(\vec{\pi}) = -\frac{1}{\beta}\left[\sum_{w=1}^{N_w}\ln\left(N_{hw}e^{-\beta\lambda} + \sum_{h=1}^{N_{hw}} e^{-\beta M_{hw}(\vec{\pi})}\right) + \sum_{b=1}^{N_{\mathrm{ToF}}} e^{-\beta M_b}\right]. \tag{4.34}$$

By introducing noise into the system, the landscape was smoothed at higher temperatures (i.e. small β). This smoothing allowed for the global minimum to be found quickly without the complication of the many local minima. Ideally, the minimum of E_{eff} at high temperature would correspond the the true global minimum when the noise was removed. Therefore by iteratively minimizing E_{eff} while slowly decreasing the temperature of the system, the track would tend towards the global minimum, avoiding all local minima. While increasing β, the penalty for rejecting a wire decreased, which allowed the algorithm to reject noise hits with less energy penalty after a energetically favorable set had been selected. This method worked relatively well for OLYMPUS, but several modifications to the algorithm were made to improve EAA, as discussed in 4.3.3.

While (Ohlsson *et al.*, 1992) and (Ohlsson, 1993) outlined how to set up E_{eff}, neither gave a prescription on starting or ending values for β or λ, or how to evolve them during the cooling process. To set the λ and β evolution, a trial-and-error approach, as described in (Russell, 2016), was used as to maximize the number of elastic tracks found in data. During each step of evolving λ and β, E_{eff} was minimized iteratively using Newton's method. Newton's method returned the stationary points of E_{eff}, including minimums and maximums relatively quickly, by assuming that the function was roughly quadratic near a starting point and taking the four-dimensional Taylor expansion of E_{eff} about the current $\vec{\pi_0}$. This method allowed for the gradient of the Taylor expansion to be calculated, using the derivatives as returned from the fast track algorithm, and the roots to be found. The track parameters were then adjusted to the stationary point $\vec{\pi} \rightarrow \vec{\pi_0} + \delta\vec{\pi}$, and the method repeated until no significant improvement was found. Occasionally Newton's method found a local maximum. To test if the stationary point was a maximum or minimum, the gradient descent method was used. The minimization of E_{eff} was done simultaneously while

lowering the temperature. For each β and λ value, only one step in the Newton's method was taken.

EAA Modifications

Several additional steps were added to the EAA algorithm to improve the accuracy and speed of the method. The OLYMPUS data presented a difficult challenge, as the left-right ambiguity for single wire hits could sometimes not be resolved unless at low temperatures, when the track was already stuck in an incorrect minimum. This invalidated the assumption that the minimum at high temperatures corresponded to the global minimum at low temperatures. For most of the tracks, especially those with cell-boundary crossings, the left-right ambiguities could be resolved at high temperatures. The cell-boundary crossing widened and deepened the global minimum at all temperatures. However at large scattering angle, $\theta > 70^\circ$ or so, most tracks did not cross any cell boundaries. This made the left-right decisions at small β impossible to resolve and frequently the track would descend into a wrong minimum as the temperature was lowered. Usually if a left-right decision was made incorrectly, the track search failed for the whole superlayer (all 6 sense wires) which could significantly change the track parameters, especially the momentum. At certain angles, the low magnetic field and high beam energy with the small Lorentz angle made distinguishing electrons and positrons very difficult.

To ensure that the tracks started near the correct value, preliminary scans in θ, z and p were done at high temperature. The φ and θ were well-restricted by the ToF reconstructed hit position and the ToF bar hit. The ToF hit that was used was the ToF signal that was matched to a Monte Carlo pattern for that event. If more than one ToF was pattern matched, the average of the hit positions was used. For the initial scan, the trajectories were assumed to be straight. This allowed the

momentum parameter to fall into either a positively or negatively bending particle, so no assumption about the PID was made before the tracking took place. The first scan was in θ, from the minimum allowed angle θ_{min} to the maximum allowed angle θ_{max}, in 50 evenly spaced steps. Taking the minimum for the θ scan, the vertex position z was scanned in 20 steps from z_{min} to z_{max}. For each scan in z, the angle θ was re-scanned over the full range and the minimum returned. For the initial scans, no minimizing was done. With the minimum in θ and z found, the momentum was coarsely scanned in 10 steps for p_{min} to p_{max}. For each step, $\vec{\pi}$ was allowed to change in all parameters to minimize E_{eff} partially.

Because the minimum of E_{eff} at high temperatures did not always correlate to the minimum at low temperatures, a method to determine if the track was trending away from global minimum was developed. With this method, the parameter space surrounding the current $\vec{\pi}$ was searched for a lower E_{eff}. The search was performed at a temperature that was determined to produce the best result, and also correlated to where the specific left-right ambiguities were becoming resolvable. With this method, the angle parameter was adjusted in four steps between the current value $\pm 10°$, and for each new value of θ, the azimuthal angle was adjusted to the current value $\pm 8°$. For each new θ-φ combination entire momentum range was scanned in four steps, while leaving the vertex position fixed. For each new θ, φ, and p value E_{eff} was minimized. The track parameters which produced the minimal E_{eff} were then selected and the cooling procedure continued.

With the initial scans and mid-temperature scans, the efficiency of the track reconstruction method improved significantly. Using Monte Carlo data, the track reconstruction software was able to make every left-right decision correctly over 99% of the time for electrons, positrons and protons over the full acceptance range of the detector.

For each pattern matched, the track reconstruction software attempted to fit a lepton and a proton. There were several scenarios where the track reconstruction would reject a track candidate. A track candidate was rejected if all the ToF detector signals or all the wire hits in a chamber were rejected. Tracks that were reconstructed completely straight (i.e., with infinite momentum) were also rejected.

4.4 Luminosity Analysis

To measure the cross section ratio with small uncertainty the relative luminosity between data taken with the positron beam and data taken with the electron beam must be known to high certainty. As mentioned in section 3.4, three independent luminosity monitoring techniques were utilized during the OLYMPUS experiment. The analysis and results from those systems are presented in this section. Each luminosity monitoring system provided a measure of the absolute electron-beam luminosity $\mathcal{L}_{e^-}$ and the absolute positron-beam luminosity $\mathcal{L}_{e^+}$ but for the OLYMPUS measurement the relative luminosity $R_{\mathcal{L}} = \frac{\mathcal{L}_{e^+}}{\mathcal{L}_{e^-}}$ was the crucial measurement. For the relative luminosity $R_{\mathcal{L}}$, many of the systematic uncertainties in the absolute luminosity measurements canceled, allowing for a more precise luminosity measurement.

The luminosity measurement made using beam and target information was called the "slow-control luminosity". This measurement estimated the luminosity using the gas density in the target and the beam current to provide a real-time estimate of the luminosity during data taking. The 12° GEM and MWPC telescopes recorded forward angle elastic electron-proton and positron-proton scattering to measure the luminosity at small angles where the two-photon exchange contribution was expected to be small. The very forward angle PbF_2 calorimeters measured the high rate Møller and Bhabha scattering from the atomic electrons in the hydrogen target. The analysis for the luminosity determined by the forward angle Møller and Bhabha calorimeters

Method	Luminosity Correction	Relative Uncertainty
12° Telescopes	1.0012	±0.47%
MIE Analysis	1.0055	±0.26%

Table 4.1: The correction to the slow-control for the relative luminosity from the 12° telescopes and the Multi-Interaction Event analyses.

utilized events where more than one interaction was recorded simultaneously in the calorimeters. This analysis was called the Multi-Interaction Event (MIE) analysis, and is discussed further in Section 4.4.3.

As will be described in Chapter 5, the result for the positron-proton to electron-proton cross section ratio was normalized using a Monte Carlo simulation. For each data file, an equivalent simulated data file was produced and the number of events in that file corresponded to the estimate of the luminosity from slow-control system. Then the other luminosity systems, the 12° and the Møller and Bhabha calorimeters, provided a correction factor to the slow-control. Because the 12° and Møller and Bhabha calorimeters provided a correction factor, the relative electron beam and positron beam luminosity is quoted as a correction to slow-control. This section discusses the three luminosity determination methods. The correction factor to the slow-control luminosity $\mathcal{L}_{\rm corr}$ was calculated as

$$\mathcal{L}^{\rm Ratio}_{\rm Corr} = \frac{\mathcal{L}^{\rm corr}_{e+p}}{\mathcal{L}^{\rm corr}_{e-p}} \frac{\mathcal{L}^{\rm SC}_{e-p}}{\mathcal{L}^{\rm SC}_{e+p}}, \tag{4.35}$$

where $\mathcal{L}^{\rm corr}_{e^+p(e^-p)}$ was provided by either the 12° luminosity monitor or the MIE analysis yielding the results shown in Table 4.1.

4.4.1 Slow-Control Luminosity Estimate

The slow-control luminosity estimate used beam and target parameters to monitor the luminosity while taking data, and provided a reliable estimate for the other luminosity systems as a check. The slow-control luminosity estimate had the advantage that the estimation was a relatively quick calculation with little analysis necessary. The instantaneous luminosity was dependent on the beam current $I_{\text{beam}}(t)$ and the target density function $\rho(z,t)$ as

$$\frac{\partial \mathcal{L}_{\text{slow}}(t)}{\partial t} = \frac{I_{\text{beam}}(t)}{e} \int_{z_{\text{min}}}^{z_{\text{max}}} \rho(z,t) dz, \tag{4.36}$$

where the beam current, $I_{\text{beam}}(t)$ was provided by the accelerator dipole magnets and e is the charge of the particles. The density of protons in the target $\rho(t,z)$ was a function of the target geometry, the gas flow, the gas diffusion rate, and the temperature of the target cell.

Originally the target density was estimated using a elliptical tube conductance analytical calculation, based on (Steckelmacher, 1986). However, the analytical calculation was found to be underestimating the target density significantly when compared to the density reconstructed using both the tracked drift chamber and 12° particles. To improve the target density calculation, a Monte Carlo simulation of the hydrogen molecules in the target was developed by (Henderson, 2016). For the entire target cell, the gas could be modeled well with a molecular flow simulation. In the molecular flow regime, the interaction of the molecules with the target cell walls dominate the dynamics of the gas and the molecule-molecule interactions can be neglected. The molecular flow simulation took information such as target geometry, gas flow, at the temperature of the target cell, and estimated the target density as discussed in detail in (Henderson, 2016).

While the Monte Carlo target simulation significantly improved the slow-control

luminosity estimation, there were still large uncertainties that stemmed from the uncertainty in the target temperature and the gas flow rate. With the molecular flow simulation, the slow-control approach could determine the luminosity to ±5% absolute luminosity and ±2% relative luminosity. While not a high accuracy luminosity monitoring system because of the large uncertainty, the slow-control luminosity estimate provided an important benchmark for the other luminosity monitoring systems.

4.4.2 12° Luminosity Telescopes

Positioned at ±12° scattering angle were two telescopes, each consisting of three Gas Electron Multiplier (GEM) and three Multi-Wire Proportional Chamber (MWPC) detectors. These tracked the forward angle electrons and positrons from elastic scattering in the target. For electron and protons scattered at $\theta = 12°$, the four-momentum transfer for the elastic scattering was $Q^2 = 0.165$ GeV/c^2, where the two-photon exchange was expected to be small or negligible. This allowed for a luminosity measurement by comparing the relative electron and positron rates in the 12° telescopes, corrected by the Monte Carlo simulation to account for acceptance changes and radiative corrections. The Monte Carlo simulation data were processed through the detector calibration, track reconstruction, and analysis software. The ratio of data to simulation events was found and the absolute luminosity for electron and positron events was given as

$$\mathcal{L}^{e^\pm}_{12^\circ} = \frac{N^{e^\pm}_{\text{data}}}{N^{e^\pm}_{\text{MC}}(\mathcal{L}_{\text{SC}})}\mathcal{L}_{\text{SC}}, \tag{4.37}$$

where $N^{e^\pm}_{\text{data}}$ was the number electrons or positrons from data and $N^{e^\pm}_{\text{MC}}$ was the number of electrons or positrons found in the Monte Carlo simulation. The simulation used the slow-control luminosity $\mathcal{L}_{\text{SC}}$ which was a source of systematic uncertainty in the absolute luminosity measurements. Fortunately, most of this systematic uncertainty

canceled in the relative luminosity measurement.

At very forward lepton scattering angle, the luminosity monitors take advantage of the very large elastic scattering cross section at small Q^2. This significantly decreased the statistical uncertainty in the luminosity measurement and allowed for the luminosity to be monitored by the 12° luminosity telescopes at a high rate. However, significant backgrounds of Møller and Bhabha scattering events were observed in the telescopes. To resolve the elastic scattering from the background at small angles, only events where the proton was also measured simultaneously in the upstream region of the drift chambers and ToF detectors, at the correct kinematic angles for elastic scattering, were included in the luminosity measurement. By requiring the events to be exclusively detected, the background was reduced significantly, providing a cleaner signal for the luminosity measurement.

This section discusses the main points of interest and results from the 12° luminosity measurement. The analysis was carried out and discussed by (Henderson, 2016). (Henderson, 2016) also discusses using the 12° telescopes to measure two-photon exchange effect at very small Q^2 using the multi-interaction events (MIE), discussed below in section 4.4.3 as a luminosity reference. While the theories unanimously assume a low two-photon exchange at that angle, the assumption had not previously been tested experimentally.

For the luminosity determination in the 12° luminosity monitors, the data from the GEM detectors was ignored and only the MPWC detectors were used. The GEM detectors showed an approximately 10% time dependence on the efficiency, which was both beam-species- and rate-dependent. New track reconstruction and hit finding were written for the GEM detectors, however these modifications did not resolve the issue, which stemmed from a saturation in the readout electronics at high event rates. (Henderson, 2016) has a detailed study of this GEM detector discrepancy.

The three MWPC planes for each telescope were used to reconstruct the trajectories of the electrons and positrons. The two-dimensional hit position that marked where the particle passed through a MWPC detector was calculated from signals on the three wire planes. To reconstruct the tracks, GEANT was used to create trajectories from all possible combinations of hits in the three planes, and provided the scattering angles, momentum, and the interaction vertex position.

Combining the lepton tracks from the 12° arm and the proton tracks from the drift chambers and ToF detectors, the elastic events were selected from the background using the φ correlation between the lepton and proton, and by requiring that the lepton and proton trajectories both projected back approximately the same vertex position in the target cell.

The efficiencies for the 12° SiPM trigger and each of the MWPC planes were calculated and included in the Monte Carlo simulation. The SiPM trigger efficiencies were calculated using triggers from the lead glass calorimeter mentioned in Section 3.4.1. For lead glass trigger events which also had hits in the MWPC planes, the tracks were reconstructed using Geant4, and projected back through the SiPM scintillator paddles to determine if the SiPM had registered a hit. This provided a two-dimensional efficiency map of each of the SiPM scintillator paddles. For all the paddles, the efficiency was in excess of 97%, the majority were over 99%. To estimate the efficiencies of the MWPC detectors, signals in the GEM detectors were used. Reconstructing tracks using the three GEM and two MWPC signals, a two-dimensional efficiency map for each MWPC was calculated.

Other efficiencies and uncertainties that were considered in the MWPC luminosity measurement were the lepton tracking efficiency, and the ToF trigger efficiency from the coincident proton. Other uncertainties that contributed to the measurement were beam position, magnetic field strength, and the effect of the elastic cuts. The

uncertainty from the two-photon exchange contribution was also estimated. The overall average absolute luminosity measurement uncertainty for the 12° luminosity monitoring method was found to be ±2.44% and the relative luminosity uncertainty to ±0.47%.

4.4.3 Symmetric Møller and Bhabha Calorimeters

At $\theta = 1.28°$ on either side of the beamline were lead fluoride (PbF_2) crystal detectors. Each consisted of a three by three array of crystals connected to PMTs which readout Cerenkov light produced by particles stopping in the crystal. These crystals were set up to monitor very forward angle electron-electron (Møller) and electron-positron (Bhabha) elastic scattering off the atomic electrons in the hydrogen target. The 1.28° scattering angle is the angle where both leptons for a 2.0 GeV beam have the same outgoing momentum of 1.0 GeV and the same scattering angle θ. The goal was to get a very precise relative luminosity measurement by measuring the rates of Møller and Bhabha events in the crystal detectors, and then comparing those rates to the rates estimated from the theoretical calculations of the cross sections and the slow-control luminosity. The Møller and Bhabha scattering processes are purely quantum electrodynamics processes and are calculable to very high precision. Also, by restricting the events to the symmetric angle, backgrounds could easily be identified and subtracted.

There were two trigger conditions that prompted for the integrated analog-to-digital (ADC) to be readout for an event: that the total integrated ADC surmounted a threshold, and that the central crystal in the array had the largest ADC signal. The calorimeters ran in three trigger modes: coincident, left-master, and right-master. For the coincident trigger, both the left and right calorimeters had to pass the two trigger conditions. In left-master mode, only the left calorimeter had to pass the trigger

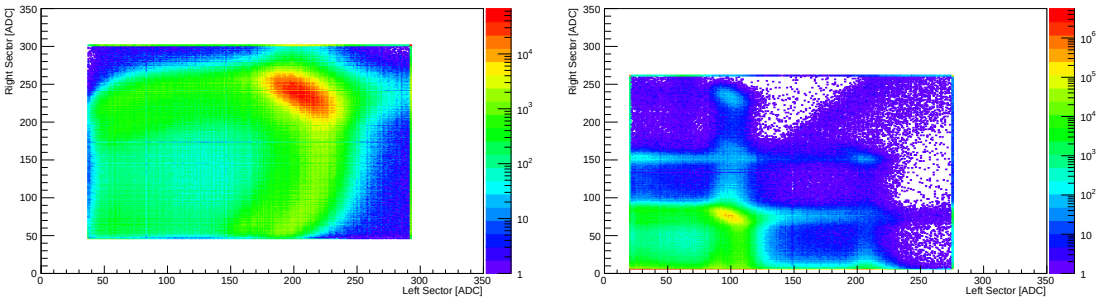

(a) Coincidence

(b) Left Master

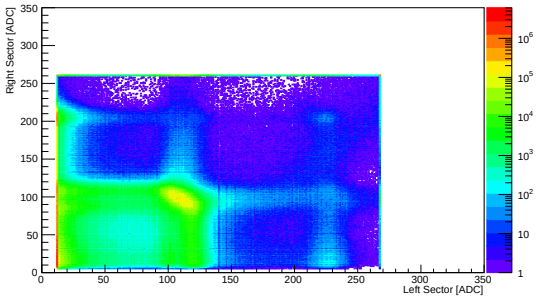

(c) Right Master

Figure 4.12: The histograms produced from the symmetric Møller/Bhabha calorimeters. Figure 4.12a was produced when both the left and right calorimeters triggered. Figures 4.12b and 4.12c were produced when only left or right calorimeter triggered.

conditions; for the right-master, only the right calorimeter had to pass the trigger conditions.

To avoid dead time in the crystals while monitoring high-rate processes, events were binned into ADC-left versus ADC-right histograms, corresponding to the three trigger modes. The data acquisition system readout the histograms approximately once per 30,000 events, which corresponded to a minute of data taking. Examples of the three histograms recorded is shown in Figure 4.12

Figure 4.12 shows the ADC-left and ADC-right histograms for coincident, left-master and right-master events. The signal from the calorimeters was digitized and

recorded in less time than the DORIS bunch spacing, which allowed for the calorimeters to differentiate between bunches in the beam. However, the signal timing was too slow to differentiate between multiple events produced from the same bunch. Therefore, the integrated ADC signal was the sum of all events per bunch that produced particles that scattered into the calorimeters. Each event in Figure 4.12 corresponded to a single bunch passing through the target. The central peak in all three histograms corresponds to Møller and Bhabha events. The peaks at higher channels correspond to either more than one Møller or Bhabha event occurring in the same bunch or other processes, including very small Q^2 elastic electron-proton and positron-proton scattering.

Measuring the Møller and Bhabha scattering did not produce a reliable luminosity monitor for the OLYMPUS experiment. However, a luminosity measurement was possible using events where more than one interaction was recorded in the calorimeters, called an Multi-Interaction Event (MIE). The analyses for the Møller and Bhabha scattering and the MIE events are discussed in the next two sections.

Symmetric Møller and Bhabha Scattering

The symmetric Møller and Bhabha calorimeters were extremely important for determining the relative luminosity to very high precision, and benefited from measuring independent processes with an independent detector and triggering system. To determine the luminosity from the rates in the calorimeters, a Monte Carlo simulation for the Møller and Bhabha cross sections, that included next-to-leading order radiative corrections, was developed by (Epstein and Milner, 2016). While the calorimeters appeared to operate correctly, the systems did not provide a result consistent with the slow-control and 12° luminosity measurements, which were consistent with each other. Figure 4.13 shows the ratio of the luminosity measured with symmetric Møller

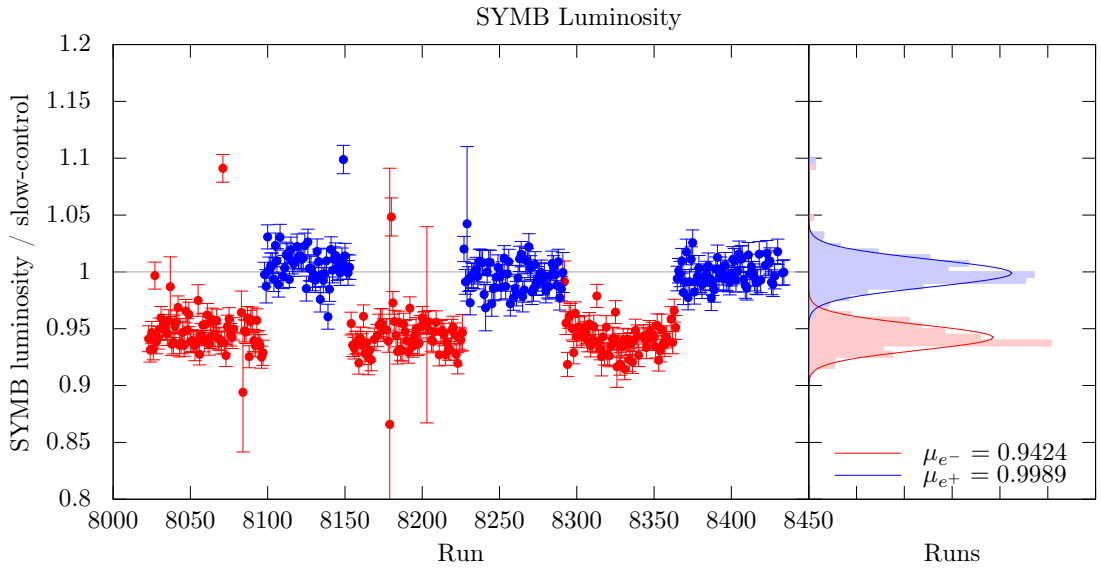

Figure 4.13: The ratio of the luminosity extracted from the rates of Symmetric Møller and Bhabha scattering to luminosity as estimated with the slow-control luminosity monitor as a function of run number. The electron beam runs are shown in red and the positron beam runs are shown in blue. Also shown is the projected ratio over all runs, fit with a Gaussian function. This figure is from Colton O'Connor.

and Bhabha calorimeters to the slow-control luminosity estimation as a function of run number. Here the electron runs are shown in red and the positron runs are shown in blue.

The luminosity determination for the Møller scattering shows approximately a 5% discrepancy with the slow-control luminosity estimation and has a slight time dependence, where as the Bhabha luminosity determination agreed with slow-control luminosity estimate.

To reconcile the luminosity measurements, a multi-year thorough search to identify and correct problem was undertaken by Colton O'Connor, which is described in detail in (O'Connor, 2017). However, the source of the discrepancy remained unknown. There were several possible explanations for the discrepancy. First, the rates of Møller and Bhabha scattering in the calorimeter were extremely sensitive to the beam

position in the target, which produced a 3% uncertainty in the luminosity extraction. Second, the cross section simulations could be incorrect. Last, an inefficiency in the calorimeters that was not well understood and was beam species dependent might be present.

Multi-interaction Events

While a direct luminosity measurement was not possible by monitoring the Møller and Bhabha rates in the calorimeter, the calorimeters still provided a precise luminosity measurement. The calorimeters not only recorded ADC spectra for Møller and Bhabha events, but also recorded the electrons or positrons from elastic scattering at very low Q^2, which would deposit about 2.0 GeV of energy in one of the calorimeters. The elastic scattering recorded in the calorimeters allowed for the luminosity to be extracted with a different method. This analysis is described in (Schmidt, 2016), with the procedure and results briefly summarized below.

As stated in the beginning of Section 4.4.3, the calorimeters could not differentiate between simultaneous events produced in the same beam bunch, and the integrated ADC recorded for that bunch was the sum of all particle entering the calorimeters. ADC recorded signals with more than one event can be seen in Figure 4.12.

Because the histograms readout by the DAQ had different ranges on the axis, some peaks were not seen in all three histograms. The largest peak in all three histograms at approximately left-ADC and right-ADC equal (200,250) channels in the Figure 4.12a, was produced from symmetric Møller and Bhabha scattering, where both particles deposited all 1.0 GeV of energy into both calorimeter. The peak at (225,200) channels in the right-master (Figure 4.12c)and left-master (4.12b) histograms corresponded to where two simultaneous Møller and Bhabha scattering events occurred. The peaks at approximately (200,0) channels in the right-master and (0,200) channels in the

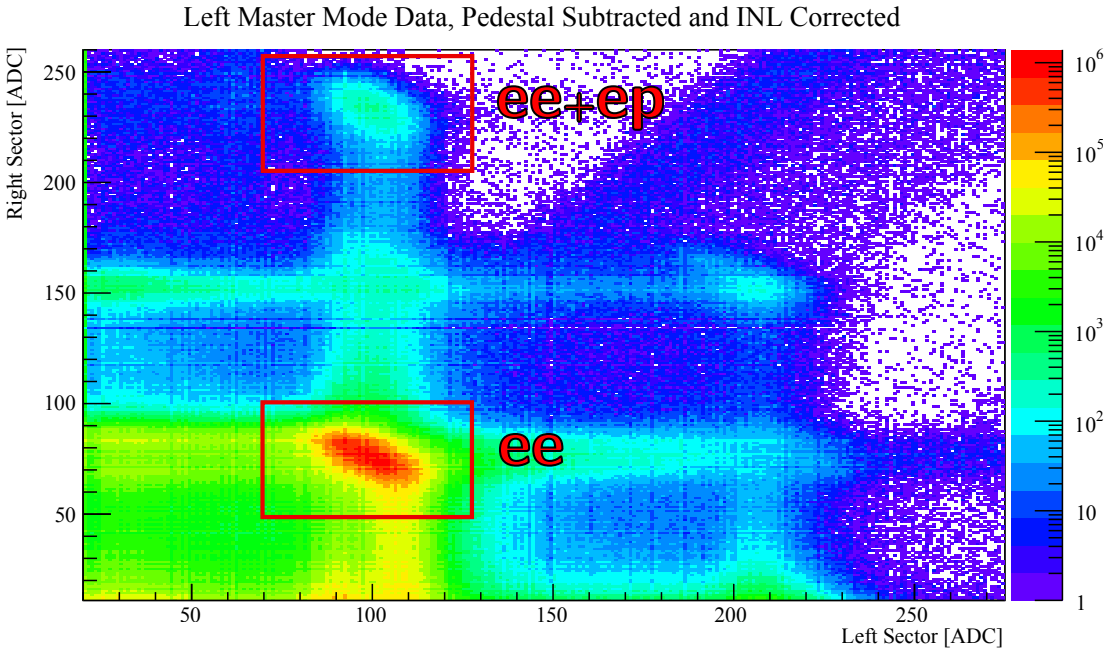

Figure 4.14: The left master histogram with the coincident peak and the Multi-Interaction Event (MIE). The coincident peak is from Møller or Bhabha Scattering detected in both calorimeters. The MIE peak was produced when a Møller/Bhabha event was observed simultaneously as a lepton from elastic scattering. Figure from Axel Schmidt (Schmidt (2016)).

left-master were produced by leptons produced from elastic lepton-proton scattering.

Important, specifically for the luminosity extraction, was the peak in the left-master histogram at (100,250) channels. This peak corresponded to when a Møller or Bhabha event was recorded in the calorimeter simultaneously with an elastic scattering event. This simultaneous interaction, called the Multi-Interaction Event or (MIE) is labeled as $(ee + ep)$ in Figure 4.14.

The rates estimated from Monte Carlo for the MIE peak were very close to what was observed in data. The MIE peak also showed the same beam species discrepancy for electron-beam events. Because of these observations, by taking the ratio of the MIE events to the symmetric Møller or Bhabha peak, the beam-species relative

luminosity was extracted. The luminosity was extracted from MIE by

$$\mathcal{L}_{\mathrm{MIE}} = \frac{N_{\mathrm{MIE}} N_{\mathrm{bunch}}}{N_{e^{\pm}e^{-}} \sigma_{e^{\pm}p}} + \text{corrections}, \tag{4.38}$$

where N_{MIE} was the number of MIE events, N_{bunch} was the number of particles in the beam bunch, $N_{e^{\pm}e^{-}}$ was the number of events in the (100,100) channel symmetric Møller or Bhabha peak, and $\sigma_{e^{\pm}e^{-}}$ was the Monte Carlo cross section for elastic lepton-proton scattering.

There were two corrections to the luminosity. The first stemmed from variance between bunches,

$$\frac{-\nu_{\mathrm{bunch}} N_{\mathrm{bunch}}^2}{\mathcal{L}_{\mathrm{SC}}}, \tag{4.39}$$

where $\nu_{\mathrm{bunch}} = \langle \mathcal{L}_{\mathrm{SL}}^2 \rangle - \langle \mathcal{L}_{\mathrm{SL}} \rangle^2$ was the variance between the number of particles in a bunch. This was found to be on the order of a one percent correction to the absolute luminosity extractions, and varied significantly with beam species. The second correction was due to higher order multi-interaction events where more than two events were observed,

$$-N_{\mathrm{bunch}} \sigma_{\mathrm{total}}^{\mathrm{sim}} \left\{ \left(\frac{\nu_{\mathrm{bunch}} N_{\mathrm{bunch}}}{\mathcal{L}_{\mathrm{SC}}} + \frac{\mathcal{L}_{SC}}{N_{\mathrm{bunch}}} \right)^2 - \frac{\langle L_{\mathrm{SL}}^3 \rangle N_{\mathrm{b}}}{\mathcal{L}_{\mathrm{SC}}} \right\}, \tag{4.40}$$

where $\sigma_{\mathrm{total}}^{\mathrm{sim}}$ was the summed cross sections for both the Møller and Bhabha events and the elastic scattering. This correction was extremely small (on the order of a tenth of a percent). While the MIE method did not provide a luminosity monitor entirely independent of the slow-control luminosity monitor the dependence is only present in the correction terms.

To extract the luminosity, the sum of the events in the MIE and the Møller/Bhabha peak was determined by cutting a box around the peak and summing all events inside. The size and shape of the box was a source of systematic uncertainty in the luminosity measurement.

The MIE analysis was able to provide the relative luminosity measurement to $\pm 0.27\%$. The uncertainties come from beam position and energy, geometry of the calorimeters, the cuts on the peaks, the magnetic field, and from uncertainty from the radiative corrections in the elastic electron scattering cross section simulation.

Chapter 5

ANALYSIS

The goal of OLYMPUS was to measure the positron-proton to electron-proton elastic scattering cross section ratio over a four-momentum transfer range $Q^2 \in (0.6, 2.2)$ $(\mathrm{GeV/c})^2$. The process to calculate the cross section ratio from the reconstructed track candidates is outlined in this chapter.

The most basic method for calculating the cross section ratio was to sort elastic scattering events in Q^2 bins, and then to compare the number of positron-proton tracks to the number of electron-proton tracks, normalized by the relative luminosity measured for both species. This process included selecting track candidates that corresponded to scattering events, discriminating between elastic and inelastic scattering, and subtracting the remaining inelastic and noise background. However, two more effects also needed to be taken into account before a accurate measurement of the cross section ratio could be extracted from the data. The first effect was radiative corrections, which are higher-order processes to the scattering cross section and can also influence the cross section ratio. The second effect was the acceptance of the detector, which function accounted for detector geometry, efficiency functions, and the accuracy of the track reconstruction software. Both these corrections were found to be species-dependent and could produce false structure in the cross section ratio.

A Monte Carlo simulation was used to account for the radiative corrections and the detector acceptance function. This simulation reproduced the cross section for lepton-proton scattering, including first-order radiative corrections. Using Geant4, the simulated data was propagated through the detector geometry and the detector acceptance function integrated. Including the Monte Carlo simulation, the positron-

proton to electron-proton elastic scattering cross section ratio was calculated as,

$$R_{2\gamma} = \frac{N^{\text{Data}}_{e^+p}}{N^{\text{Data}}_{e^-p}} \frac{\mathcal{L}_{e^-p}}{\mathcal{L}_{e^+p}} \left(\frac{\sigma^{\text{MC}}_{e^-p}}{\sigma^{\text{MC}}_{e^+p}} \right). \tag{5.1}$$

$N_{e^\pm p}$ was the number of positron-proton or electron-proton elastic events within the Q^2 bin, $\mathcal{L}_{e^\pm p}$ was the measured luminosity for both beam species and the simulated cross sections was $\sigma^{MC}_{e^\pm p}$.

The first section of the chapter describes the Monte Carlo simulation, from event generation through digitization. The remainder of the chapter describes the particle identification methods, the event selection, and the background subtraction procedure used to remove inelastic events, all applied to both real and simulated data.

5.1 Monte Carlo Simulations

The purpose of the Monte Carlo simulation was to account for the convolution of the radiative corrections, the geometry and measured efficiencies of the detector, the track reconstruction efficiency, the analysis cuts, and the background subtraction in the measured cross section ratio. In particular, understanding any beam species dependent differences in the detector resolution or analysis which might produce false features in the cross section ratio was important.

A duplicate Monte Carlo file was generated for each data file. The Monte Carlo simulation obtained the beam energy, slope, position, beam type and other experimental parameters from each data file. The luminosity applied to the Monte Carlo was based on the slow control calculation with the molecular flow model, described in Section 4.4.1.

The method for including the Monte Carlo simulation is outlined in the flow chart shown in Figure 5.1. As shown in Figure 5.1, for the simulation, first $e^\pm p$ scattering events (including inelastic processes where a real photon emission occurred via

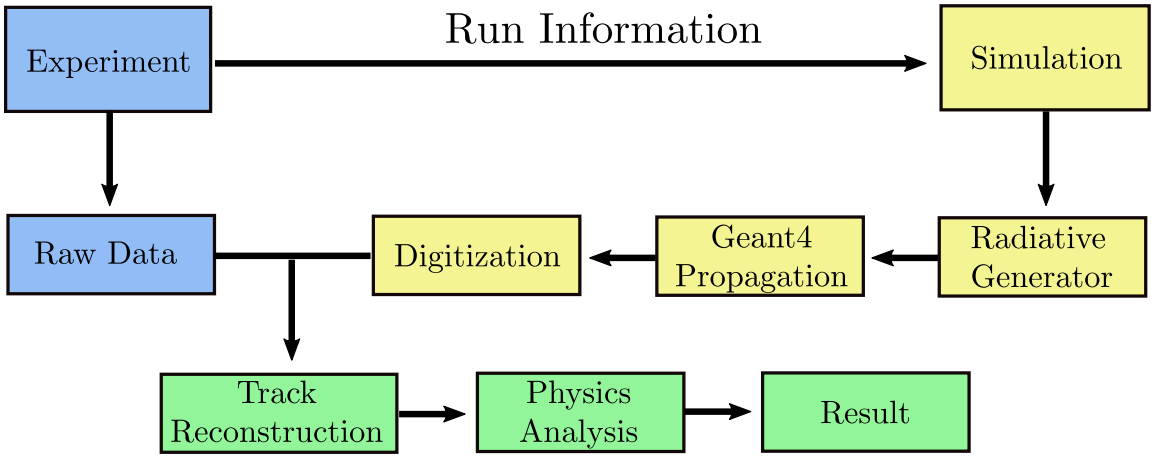

Figure 5.1: A diagram of the analysis method. The simulated Monte Carlo events were generated with the radiative generator as described in Section 5.1.1. The simulated particles were propagated through the detector simulation using Geant4. The digitization software recreates the detector signals from the tracks in the same format at the raw experimental data. Both the experimental and simulated detector data is reconstructed into tracks and sent to the physics analysis software.

bremsstrahlung radiation) are simulated and weighted by the scattering cross section. These events are propagated through the simulation of the detector using Geant4. This accounts for any hard-edge acceptance effects at the edges of the drift chambers or time-of-flight detectors. Then the interactions of the simulated particles with the sensitive regions of the detector were digitized. The digitization takes the simulated signal from the Monte Carlo simulation (which included the energy deposited, the hit position and the time) and attempted to reproduce the raw data. To do this, the timing delays, efficiencies and the effect of the electronics on the raw data were reproduced. The digitized simulated data and the real data were processed with the same track reconstruction, analysis, and background subtraction software. Last, the ratio $R_{2\gamma}$ was calculated using Equation 5.1.

The complete first-order radiative correction to the lepton-proton cross section cannot be calculated without including either an assumption of the proton structure,

or an approximation in the calculation. The variance in $R_{2\gamma}$ based on the model of the proton structure used or the approximations made in the radiative cross section calculation, provided an estimate of the systematic uncertainties due to the radiative correction model. To avoid simulating, propagating, digitizing, and tracking multiple events with the same kinematic parameters (θ, φ, etc.) the various cross sections for the radiative lepton-proton scattering were carried as a weight. The cross section variations included different models for the proton structure and various commonly used radiative correction prescriptions. The cross section weight was selected during the physics analysis, allowing the effect of the weights on the ratio to be studied.

This section will outline the radiative scattering generator, and the propagation and digitization of the simulated data.

5.1.1 Radiative Corrections

Radiative correction are higher order contributions to the cross section. The radiative corrections can either be internal or external. For internal contributions, all the photon lines are closed. At the the first order in the perturbation in the elastic lepton-proton scattering cross section, these include the lepton and proton vertex corrections (Figures 5.2e and 5.2f), vacuum polarization (Figure 5.2i), the two-photon exchange box and cross box contributions (Figure 5.2g and 5.2h), and the lepton and proton self energy diagrams (Figures 5.2a, 5.2b, 5.2c, and 5.2d).

The external radiative processes include emissions of a final state photon via bremsstrahlung radiation off of any of the proton or lepton arms. These are shown in Figure 5.3.

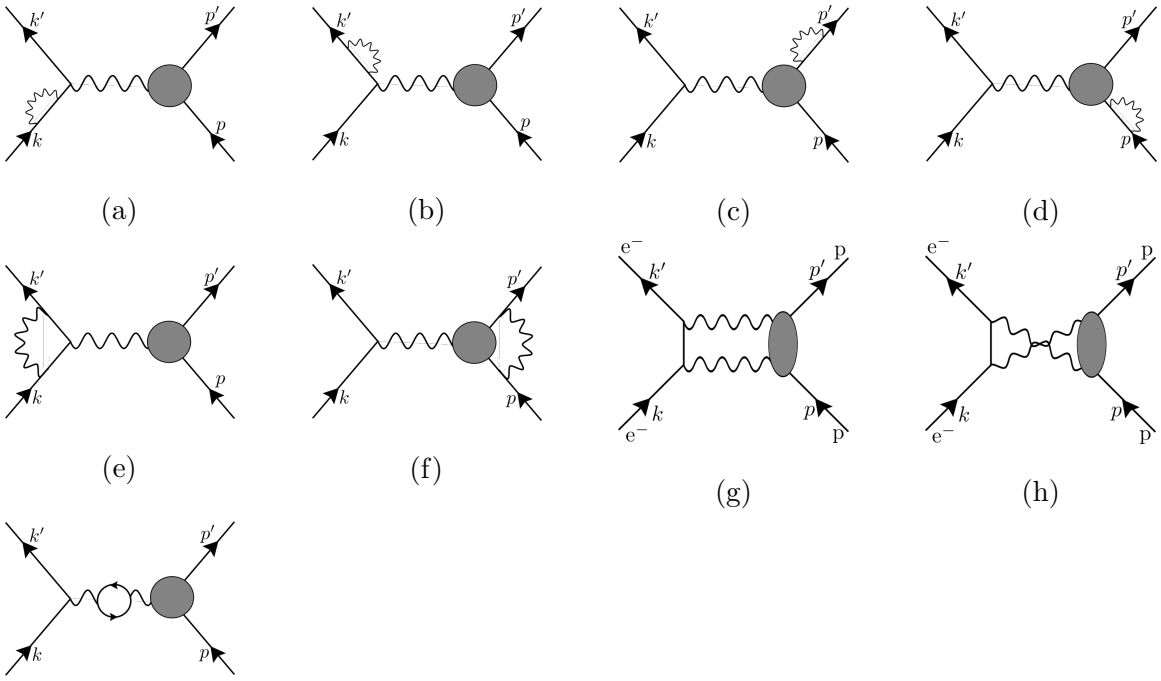

Figure 5.2: Feynman diagrams of first order virtual radiative corrections in lepton-proton scattering. (a)(b): lepton self energy. (c)(d): proton self energy. (e): lepton vertex correction. (f): proton vertex correction. (g): two-photon box diagram. (h): two-photon cross-box diagram. (i): vacuum polarization.

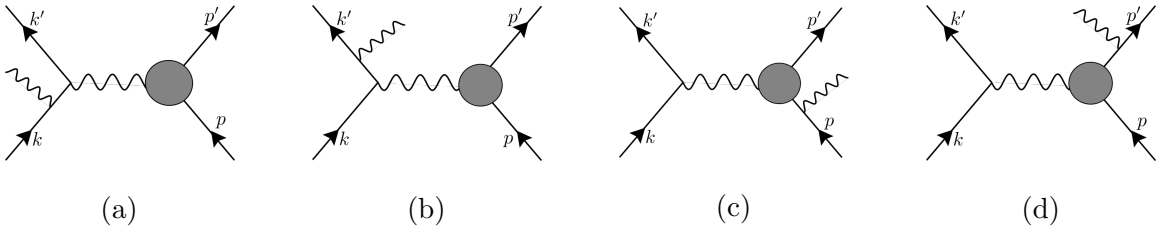

Figure 5.3: Feynman diagrams of order α^3 external radiative corrections. (a)(b): lepton bremsstrahlung. (c)(d): proton bremsstrahlung

Radiative Corrections in OLYMPUS

The goal of OLYMPUS was to determine the hard two-photon exchange contribution by measuring the interference term between the one- and two-photon exchange amplitudes. This contributes to the electron-proton scattering cross section at order α^3 in the perturbation. However, that effect is not the only order α^3 contribution to the scattering cross section. Additional radiative corrections beyond the two-photon exchange contribute more to the electron-proton elastic cross section. These radiative corrections also can effect $\frac{\sigma_{e^-p}}{\sigma_{e^+p}}$ and, if not included in the measurement, will distort the the extraction of the two-photon exchange contribution. Most of the first order radiative corrections can be calculated independent of a proton form factor model, and are included in the standard radiative corrections applied to scattering experiments. The internal contributions, which are order α^3, are interference terms between the one-photon exchange amplitude and the following:

- the lepton vertex correction: 5.2e
- the proton vertex correction: 5.2f
- the soft two-photon correction box: 5.2g and cross box 5.2h diagrams
- and the vacuum polarization: 5.2i

All these corrections except vacuum polarization diverge in the limit that the internal photon line momentum goes to zero, $k_\gamma \to 0$. The external contributions of order α^3 are

- the lepton bremsstrahlung: $[5.3\text{b} + 5.3\text{a}]^2$
- the proton bremsstrahlung: $[5.3\text{c} + 5.3\text{d}]^2$
- and interference term between the lepton and proton bremsstrahlung:

$$[5.3\text{b} + 5.3\text{a}]^{\dagger}\,[5.3\text{b} + 5.3\text{a}]$$

These also all diverge when $k_\gamma \to 0$; however, the divergences between the internal and external contributions mathematically cancel. Therefore, none of the first-order process can be entirely neglected from the calculation.

Processes that are most important are the lepton-proton bremsstrahlung interference and the soft two-photon box and cross box diagrams because those diagrams are sensitive to the charge of the lepton.

Including Radiative Corrections in the Cross Section Ratio

Historically, radiative corrections have been applied to experimental results following the prescription of (Mo and Tsai, 1969) and more recently (Maximon and Tjon, 2000). These prescriptions assume inclusive scattering, where only the lepton is detected and the proton and any bremsstrahlung photons go undetected.

In (Mo and Tsai, 1969), the two-photon exchange box and cross box diagrams are taken in the limit of "soft" two-photon exchange, where the cross section is calculated in the limit that one of the photon's momentum is zero. Also, the bremsstrahlung calculation and the proton vertex corrections are taken in the soft photon limits. By taking the soft-photon limits, (Mo and Tsai, 1969) were able to avoid including models for the proton form factors in the cross section calculation.

This method also allowed for the Born approximation cross section to be completely factorized out from the contribution to the measured cross section from radiative corrections. From this, the radiative cross section $d\sigma_{\mathrm{RC}}/d\Omega_{e^-}$ could be separated into the Born cross section Equation (2.11) and a contribution from radiative corrections δ:

$$\frac{d\sigma_{\mathrm{RC}}}{d\Omega_{e^-}} = \frac{d\sigma_{\mathrm{born}}}{d\Omega_{e^-}}\,(1+\delta)\,, \tag{5.2}$$

where $\delta = \delta(\theta, \Delta E_{\text{cut}})$, and θ is the lepton scattering angle. This method of including the radiative corrections relies on the ability to reasonably define a minimum energy difference ΔE_{cut}, the minimum energy difference that can be resolved between an elastic scattering event and an event with a low energy bremsstrahlung emission. The minimum energy ΔE_{cut} correlated to the momentum resolution in the detector. Any event with a bremsstrahlung photon with missing energy less than ΔE_{cut} will contribute to the measured elastic cross section. For this method to work, the momentum resolution of the detector has to be well defined.

(Maximon and Tjon, 2000) updated the (Mo and Tsai, 1969) method to include models for the proton's structure. This negated the need for the soft photon approximation in the proton vertex correction and bremsstrahlung calculation. (Maximon and Tjon, 2000) also relaxed the soft photon limit in the two-photon exchange calculations.

While (Maximon and Tjon, 2000) significantly improved the radiative correction calculation, the correction was still formulated for inclusive scattering and relied on the ability to define ΔE_{cut}. OLYMPUS measured exclusive scattering, where the coincident lepton and proton both were detected. Making an exclusive measurement was important for OLYMPUS to identify and eliminate backgrounds, partially because the momentum resolution was poor. Also, the resolution of the OLYMPUS detector was not well understood. A significant, but not well known, fraction of hard bremsstrahlung events fall below the resolution of the detector and contributed significantly to the cross section ratio. This made defining a meaningful ΔE_{cut} impossible for OLYMPUS, and a different process was used.

To include radiative corrections in the exclusive measurement for OLYMPUS, while avoiding a hard ΔE_{cut}, a Monte Carlo simulation was used. This allowed for the bremsstrahlung photon energy to be integrated using the Monte Carlo simulation.

The Monte Carlo simulation also permitted incorporating the complicated acceptance function, detector resolution and efficiencies, as well as permitting analysis cuts and background subtraction to be combined with the radiative corrections in one step. The Monte Carlo generator for radiative events was written by Axel Schmidt, Rebecca Russell, and Jan Bernauer. For details on the cross section calculation, event sampling, and results, see (Schmidt, 2016) and (Russell, 2016). The generator followed the same approach shown in (Bernauer, 2010).

Calculating the radiative correction using a Monte Carlo simulation allowed for a full bremsstrahlung calculation without the soft-photon approximation or the peaking approximation, where the photon is restricted to being emitted in either the incident or scattered lepton directions.

The lepton-proton bremsstrahlung interference term was dependent on the form factor for the proton. Several models of the form factor were used, as discussed below.

The Monte Carlo Event Generator

The radiative events produced by the Monte Carlo generator were constrained by the scattered lepton and the bremsstrahlung photon. Events were sampled over the lepton scattering angles θ_e and φ_e, the angles relative to the lepton track of the radiated photon θ_γ and φ_γ, and the photon energy k_γ. By weighting the events, the radiative cross section was included.

Because the outgoing kinematic parameters for the particles were generated independently of the cross section weight, multiple weights could be assigned to each event. The weights included form factor models and other radiative correction prescriptions to study the effect of the radiative correction model on the result. The weights included:

1. Form Factor Models

(a) Point-like proton

(b) Dipole form factor, Equation (2.14)

(c) Global Kelly fit ((Kelly, 2004))

(d) Global Bernauer fit ((Bernauer *et al.*, 2014b))

2. Radiative Correction Prescriptions

(a) (Mo and Tsai, 1969)

(b) (Maximon and Tjon, 2000)

(c) (Meister and Yennie, 1963)

(d) Soft Bremsstrahlung

3. Vacuum Polarization Particles

(a) Lepton contributions, ((Gramolin and Nikolenko, 2016))

(b) Lepton and hadronic contributions ((Actis *et al.*, 2010))

After generation, the simulated particles were propagated through the detector, digitized, and processed with the track reconstruction and analysis software. The weight was selected while calculating the final result. This allowed the influences of the various prescriptions and form factor models on the final result to be understood.

Details of the methods and the results from the radiative generator are discussed (Russell, 2016) and (Schmidt, 2016).

5.1.2 Propagation

After the simulated particles were generated, they were propagated through a simulation of the detector geometry using Geant4, ((Agostinelli *et al.*, 2003) and (Allison *et al.*, 2006)). Geant4 is a "toolkit for the simulation of the passage of

particles through matter", and includes libraries, written in c++, to simulate how the scattered particles will interact with the detector geometry and materials. During the simulation, when a particle interacts with any of the materials in the detector, Geant4 returns the interaction point, a time stamp, and a predicted amount of energy deposited in the material.

The geometry of the OLYMPUS detector was measured during the detector survey, described in (Henderson, 2016), and simulated using Geometry Description Markup Language (GDML), ((Chytracek *et al.*, 2006)), as described in (O'Connor, 2017). The magnetic field maps, as described in 3.3.1 and (Bernauer *et al.*, 2016), were included to model how the scattered particles would bend in the magnetic field.

5.1.3 Digitization

The goal of the digitization simulation was to convert the Geant4 hit information into an accurate estimate of the detector response. This involved modeling how the detector subsystems responded to particles passing through the detector and how these signals were read out with the data acquisition (DAQ) system. The simulated electronic signals were stored in identical formats to the real raw data. This allowed for the simulated data to be analyzed with the same software as the real data. A digitization routine was written for the detector components to fully reproduce the raw data.

The digitization methods also simulated the efficiencies in the detector subsystems. Position-dependent efficiencies in the detector had large effects on the relative e^+p and e^-p rates measured. With the magnetic field, the electrons and positrons of the same scattering angle are pushed into slightly different parts of the drift chambers and time-of-flight detectors. Therefore, any position dependent efficiencies, if not properly simulated, were sources of false structure in the ratio.

Time of Flight Digitization

The goal of the time-of-flight digitization was to convert the simulated energy deposited in the scintillator into analog-to-digital (ADC) and time-to-digital (TDC) distributions for each photomultiplier tube (PMT). By modeling the light-output response of the scintillator and attenuating the amplitude as the light traveled towards the lightguides, an estimate of the signal reaching the PMT was generated. Using the PMT gains found from data (Section 4.1.5), and by modeling the discriminators, the ADC and TDC distributions were found. Accurately modeling the amplitude of the light output, the gain, and the discriminators also produced an estimate of the efficiencies of the ToF detectors. The efficiency studies for the ToF were especially important because the ToF counters were used as a trigger for the experiment. Any inefficiencies that correlated to trigger bias could affect the ratio results significantly.

The propagation simulation, as discussed in Section 5.1.2, used the Geant4 libraries to simulate the interaction between the scattered particles and the materials in the detector. Geant4 modeled each particle's path through the scintillator paddles in small discrete steps. For each step, the local position in the scintillator, a time stamp, and estimation of the energy deposited in the scintillator was calculated. With these parameters and the ToF calibrations from data, the resulting ADC and TDC were calculated.

The time needed for the signal to reach the top and bottom PMTs on each ToF bar was calculated iteratively, step-by-step, using the hit location in the scintillator and the measured speed of light, as described in section 4.1.3. For each step, half the energy deposited was propagated with attenuation to the top PMT and the other half was propagated with attenuation to the bottom PMT. The resulting signal amplitude at each PMT was calculated using the location of the step and the position

dependent attenuation function, Section 4.1.6. Before simulating the response of the discriminators, the energy signal was smeared, ((Russell, 2016)). The smearing was important to help account for uncertainties in the calibrations and to add realistic noise to the Monte Carlo data.

At the PMT, the signal was assumed to have a shape as a function of time given by

$$A(t) = \sum \frac{A_{\text{step}}}{\tau_1 - \tau_2} \left[e^{-\frac{t-t_{\text{step}}}{\tau_1}} - e^{-\frac{t-t_{\text{step}}}{\tau_2}} \right] \Theta(t - t_{\text{step}}), \tag{5.3}$$

where A_{step} is the attenuated amplitude of the signal at the PMT, and t_{step} is the calculated time for the light to each the PMT. The decay and rise constants τ_1 and τ_2 were estimated from oscilloscope images taken while checking the PMTs before data were taken. Assuming the signals at each PMT had this shape, the discriminator responses were simulated. The discriminator simulation is described in (Russell, 2016) and included calculations for both the leading-edge and constant-fraction discriminators using thresholds extracted from data.

The two most upstream bars in either sector had leading-edge discriminators. The simulation for the leading-edge discriminators simply returned the time when the amplitude $A(t)$ from Equation (5.3) crossed the threshold. The rest of the ToF detectors had constant-fraction discriminators. These were simulated in the manner such devices work. The signal, as given by Equation (5.3), was split into two. One pulse was amplified and the other was inverted and delayed. The zero crossing of the recombined signal was given as the time for that event. Events which did not cross the threshold were rejected. The ToF trigger was simulated, and events which did not meet any of the trigger conditions were rejected.

The time calculated from the discriminator simulation was converted to channels using the TDC time per channel conversion t_{res}. The time-delays TDC_{delay} described in Sections 4.1.1 and 4.1.2 were applied along with a randomly generated reference

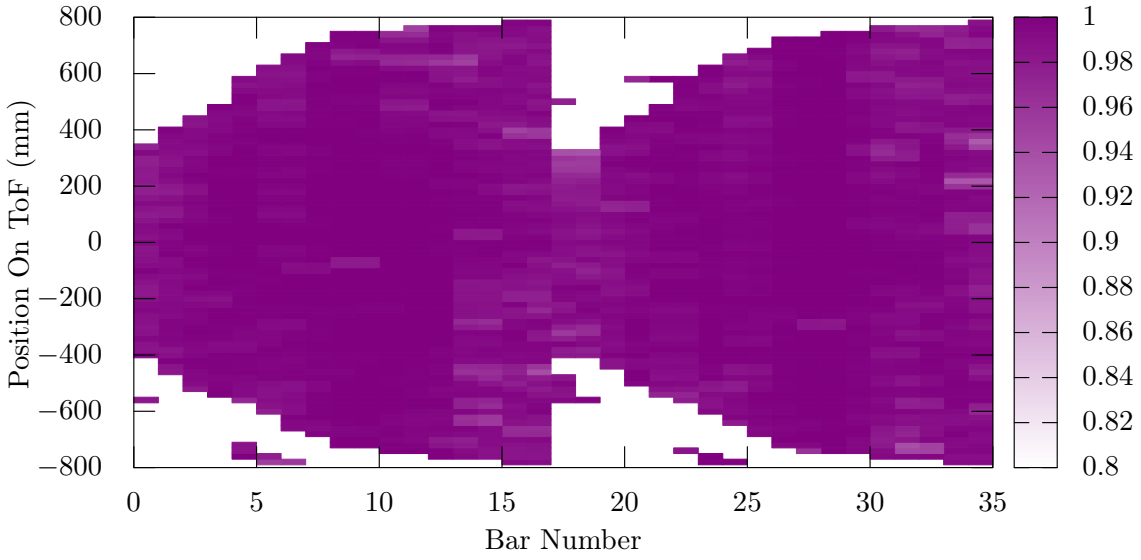

Figure 5.4: Time-of-flight efficiency estimated from the Monte Carlo.

time TDC_{ref}. Both TDC_{delay} and TDC_{ref} were subtracted from the time in the first step of the analysis, but those times were put in the digitization so that the same analysis code could be used for data and Monte Carlo. The integrated ADC values were calculated for events which crossed the threshold by integrating the signals that reached a PMT, converting to channels using the gain, and adjusting by the ADC pedestal.

Trusting the attenuation lengths, the PMT gains, and the discriminator thresholds extracted from data, the discriminator simulation also provided an estimate of the efficiency of the ToF detectors. Signals that were below the thresholds after being attenuated through the scintillator were rejected and did not trigger an event. The efficiency for the ToF bars, as found with the Monte Carlo simulation, is shown in Figure 5.4.

This method for estimating the efficiency had the benefit that the efficiency as a

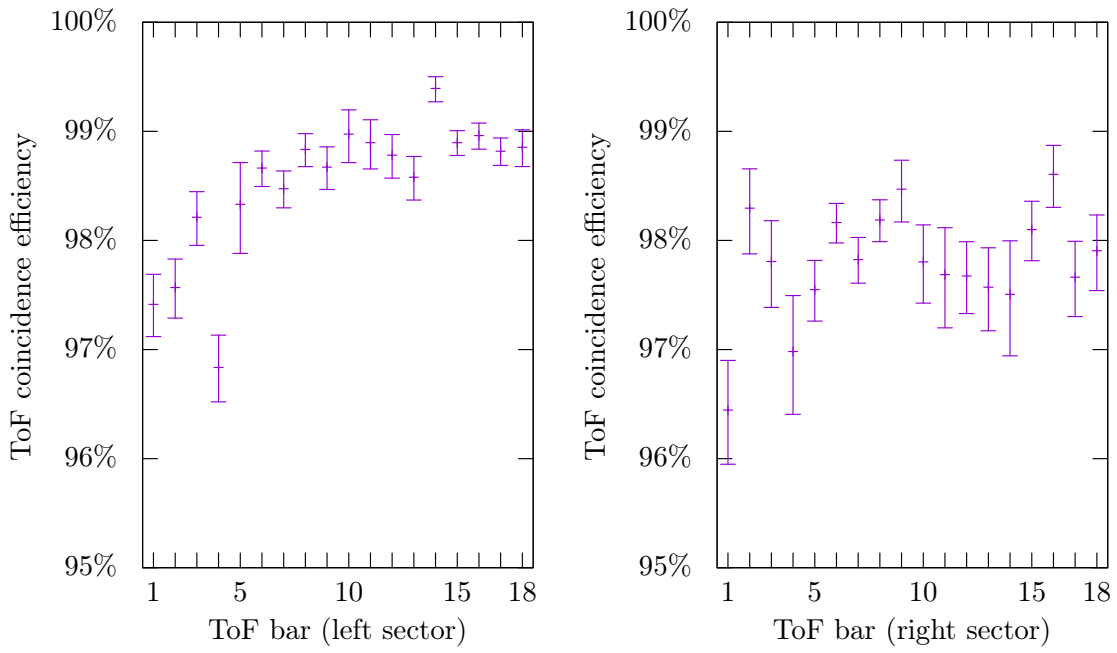

Figure 5.5: Time-of-flight efficiency as measured using the Silicon Photo-multiplier sandwich.

function of the hit position was calculated. Also, this method allowed for efficiency as a function of time during the data taking period to be monitored by updating the ToF parameters with a time dependence. Two other methods were used to calculated the ToF efficiency, but both had flaws that limited their usefulness.

The first method of extracting the ToF efficiencies measured these efficiencies directly while taking cosmic data using two silicon photomultiplier (SiPM) scintillators. The SiPM detectors were hung from the ToF support so that the two SiPMs were on either side of the ToF paddle and at roughly the same height. This created a SiPM ToF SiPM sandwich. Coincidence hits for both SiPMs triggered an event, and the efficiency of the ToF was found by looking at the SiPM coincidence rate to the number of ToF triggers. The ToF efficiencies measured this way are shown in Figure 5.5.

The SiPM efficiency method had the disadvantage that only a small section of the ToF paddle was measured near the center of the bar. Because of the shortened attenuation length, the efficiency of the detector decreased further from the center of the bar, which is not measured with this method. This method also does not account for any efficiency differences with particle species, or time-dependent changes that might have occurred during the long data taking periods.

A second method to estimate the ToF efficiency was using the pre-scaled 3/4 trigger. This trigger required a coincident top and bottom PMT signal on one ToF bar, but only a signal in one PMT on another ToF bar in the other sector. By selecting events which fired the 3/4 trigger and checked to see if a signal was recorded on the PMT not required from the trigger, an estimate of the efficiency was ascertained. However, the signal was almost completely dominated by low energy lepton background events. To reconcile this, the events that triggered the 3/4 trigger were reconstructed using the drift chamber information in Section 4.3 without the ToF information included. Using this approach, the low-energy lepton backgrounds could be identified. Unfortunately, because the trigger was pre-scaled, the inefficiency of the track reconstruction without the ToF information, and the large background rate, a comprehensive efficiency measurement was not possible.

Drift Chamber Digitization

The drift chamber digitization reproduced the TDC distributions for wires from the hit positions of the tracks through the chambers. The Geant4 propagation returned the positions where particles intercepted with the drift chamber wire planes. To account for the drift time of the ionization electrons to reach the wire, the time-to-distance function, described in Section 4.2.2, was inverted, so that the time-to-distance function became a distance-to-time function. Smearing and the time-delays

from electronics and the particle time-to-wire, as described in Section 4.2.1, was performed and were added to the time, and the time was converted into channels using the time-to-channel conversion, C_{ch}.

Efficiency maps were calibrated from data, which have the efficiency as a function of hit position in the drift chambers. Simulated events were excluded from the simulation with probabilities based on the efficiency maps, to simulate the inefficient regions in the drift chamber. These maps are described in (Henderson, 2016).

5.2 Analysis for the Cross Section Ratio

This section describes how the cross section ratio was formed from the real and simulated Monte Carlo data. With the digitized simulation files and the raw real data, the preliminary detector analysis and track reconstruction software, described in Chapter 4, was run over the entire data set. The output of the track reconstruction software provided track candidates for each event. This included information on $\vec{\pi} = (\theta, \varphi, z, p)$ and the track's projected hit position $(x_{\mathrm{Tr}}(\vec{\pi}), y_{\mathrm{Tr}}(\vec{\pi}))$ on the ToF plane. The track reconstruction also included the information as to whether $\vec{\pi}$ was a lepton track or a proton track. With this information, the correct track candidates were selected and the scattering event recreated.

Because the tracking software returned at least one track candidate for each pattern matched (unless all track candidates were rejected), there were usually several track candidates per sector to select from. An illustration of the track candidates for a scattering event is shown in Figure 5.6, which shows several track candidates and several ToF hits per sector. The cells in the drift chambers and ToF detectors where a signal was recorded are filled with either blue or red. The cells and ToF bars filled with blue are the signals that were matched with the pattern matching algorithm, and the red hits are the signals that were not matched. The track candidates, as recon-

structed using the EAA algorithm, are represented by the red or blue curves coming from the target. The blue curves correspond to positively-charged particles and the red curves correspond to negatively-charged particles. This diagram illustrates the complexity of some of the events, where multiple track candidates and corresponding ToF signals were output from the track reconstruction software. The purpose of the particle identification and track selection routines was to correctly identify the track candidates and ToF signals that corresponded most accurately to a real scattering event.

Before selecting the best track candidates to reconstruct an event, a ToF signal was assigned to each track candidate. This was done by minimizing the difference between $(x_{\mathrm{Tr}}(\vec{\pi}), y_{\mathrm{Tr}}(\vec{\pi}))$ for a track and the reconstructed position from the ToF signal. Also, a particle ID consistency check was performed at this stage. This method is described below.

Once a ToF signal was assigned to each track candidate, the two tracks (one for each sector) needed to be selected to produce the most reasonable event. The goal was to select tracks that appeared to be coming from the same scattering event in the target, while not biasing the event reconstruction towards elastic scattering events. The procedure used looked at the vertex position of the tracks and the projected initial timing of the event and is described in Section 5.2.2. Once the two track candidates were selected, events where the angular correlation was far from the region allowed by elastic scattering, were removed. Last, the background was subtracted (Section 5.2.3) to get a clean elastic scattering sample.

5.2.1 Particle Identification

The focus of the OLYMPUS experiment was exclusive lepton-proton elastic scattering. Before rates could be measured, the elastic events were isolated from the

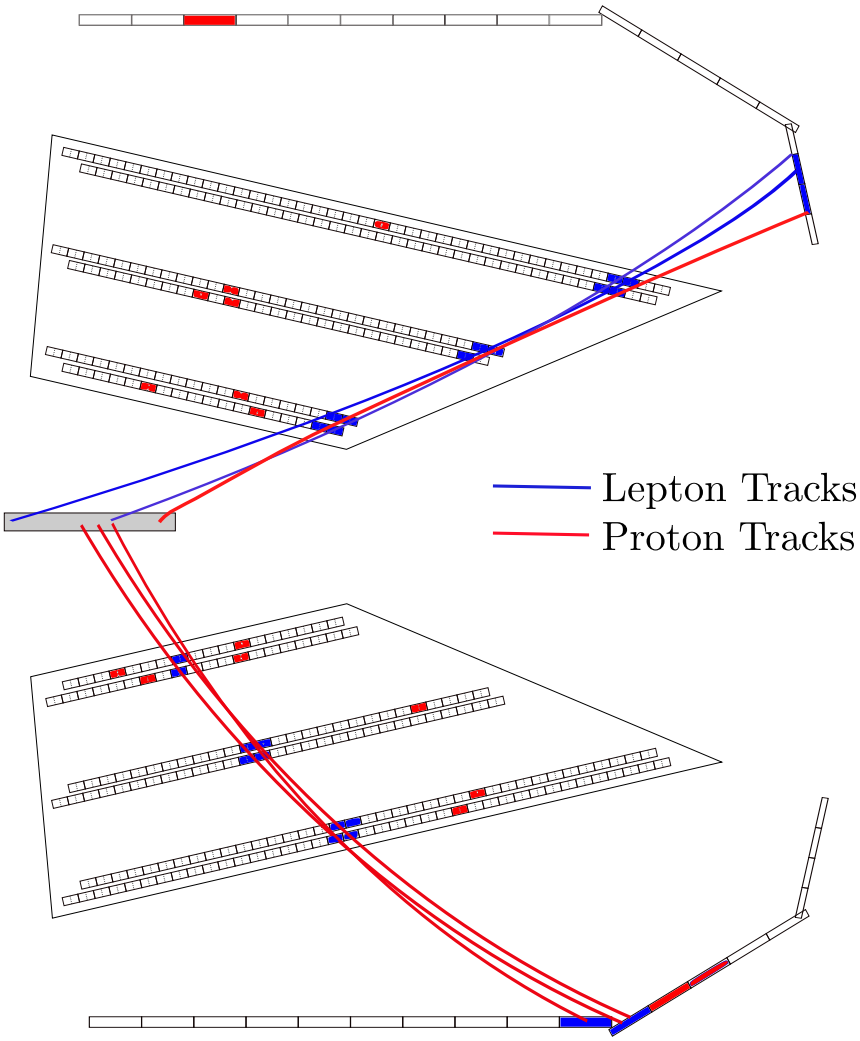

Figure 5.6: Illustration of a scattering event though the drift chambers and the time-of-flight detectors. The track candidates for protons are shown in blue, and electrons are shown in red.

inelastic scattering and noise backgrounds. The first step in doing this was by pairing each track candidate to a ToF hit and from this information, assigning a particle identification to each track/ToF pair. Second, each track/ToF pair had to be matched with another in the opposite sector by looking at track quality, initial timing, and vertex position of the events. Finally, once a two-particle event had been selected, this event needed to be identified as an elastic scattering or inelastic background event using kinematic relations.

For each event, the track reconstruction returned one or more unique track candidates and one or more ToF hits for each data pattern matched. The track reconstruction used Fast Track, as described in Section 4.3.1, which correlated signals in the detector to initial scattering parameters $\vec{\pi} = (\theta, \varphi, p, z)$ for protons and leptons. The track reconstruction attempted to fit $\vec{\pi}$ for both leptons and protons to the detector signals and returned the best fit for both particle types. Unless a failure condition was met in the track reconstruction, twice the number of patterns matched for track candidates per sector per event were generated.

The goal of the PID method was to assign the ToF signal to a track candidate that most likely was produced from the same event. From the ToF information, the ToF bar number and the vertical hit position (b_{ToF} and y_{ToF}, respectively) are known. This information can also be reconstructed for each track candidate by projecting the track to the ToF plane and calculating the estimated ToF bar number and vertical hit position ($x_{\mathrm{Tr}}(\vec{\pi})$ and $y_{\mathrm{Tr}}(\vec{\pi})$) returned from the Fast Track algorithm. For each track candidate and ToF hit, the differences of the ToF bar number b and the vertical position y between the ToF information and the track estimates were written as Δb and Δy and are calculated as

$$\Delta \mathrm{b} = \frac{b_{\mathrm{ToF}} - x_{\mathrm{Tr}} - \mu_b}{\sigma_b}, \tag{5.4}$$

and

$$\Delta y = \frac{y_{\mathrm{ToF}} - y_{\mathrm{Tr}} - \mu_y}{\sigma_y}. \tag{5.5}$$

The means and standard deviations μ_{b}, μ_{y}, σ_{b}, and σ_{y} were found from fitting the difference in bar numbers and vertical hit positions between ToF and track information with Gaussian functions. The width σ_{b} comes from uncertainty in the scattering angle of the reconstructed track, and σ_{y} is related to both the azimuthal angle uncertainty in the track and position in the ToF. Both μ_{b} and μ_{y} were very close to zero, because any lingering differences were corrected for in the detector calibrations.

Before assigning a ToF hit to each track candidate, a particle identification (PID) consistency check was performed. The track reconstruction software returned the PID that corresponded to the $\vec{\pi}$ for each of the track candidates. PID information could also be ascertained from the ToF information. Both the track PID and the ToF PID were required to be consistent.

For the ToF PID, the two relevant parameters were the reconstructed mass of the particle and the energy deposited in the ToF detectors as a function of particle momentum. The mass-squared m^2 was calculated using the ToF mean time t_{ToF}, the track momentum p, and the total path length for the particle from the target to the ToF detector L_{path},

$$m^2 = p^2 \left(\frac{\mathrm{c}t_{\mathrm{ToF}}}{L_{\mathrm{path}}} - 1 \right), \tag{5.6}$$

where c is the speed of light in a vacuum. The reconstructed mass distribution is shown in Figure 5.7. Here the lepton peak and proton peak are easily distinguishable from each other. The lepton peak is labeled m_e^2 and the proton peak is labeled m_p^2. Because $\left(\frac{cT}{L} - 1\right)$ was significantly larger for protons, the variance in the reconstructed momentum broadened the proton peak significantly compared to the lepton peak.

Because the PID from the track parameters was reliable, the calculated m^2 was

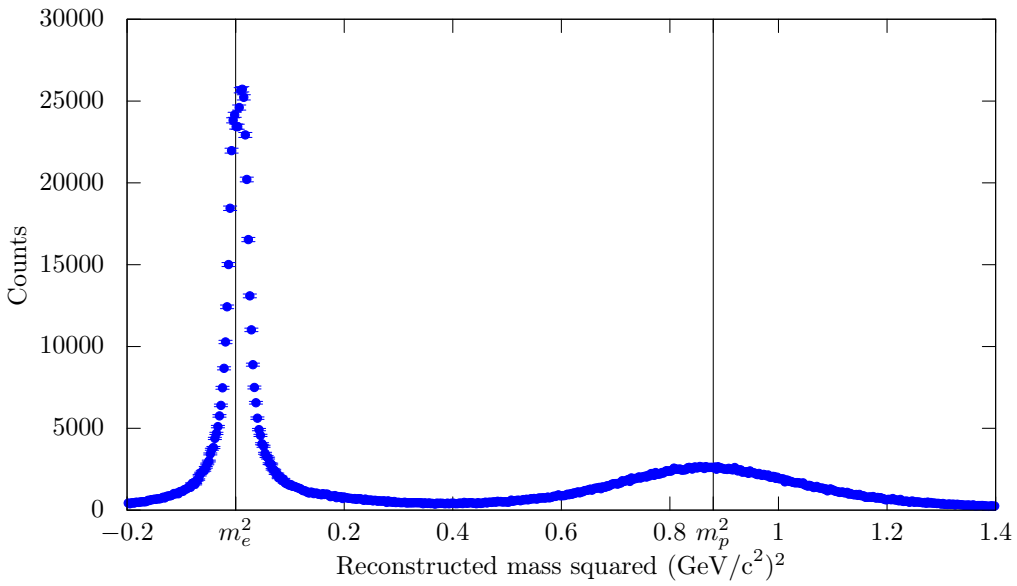

Figure 5.7: Calculated m^2 for all particles using reconstructed momentum and path length and time-of-flight. Particle masses $m^2_{e^\pm}$ and m^2_p are labeled.

just used as a cross check. For each ToF bar, and for both positron and electron beam data, the interception point between the lepton mass peak and the proton mass peak m^2_{cut}, as in Figure 5.8, was found. Figure 5.8, is the mass-squared for leptons and protons over a smaller range of calculated m^2 to highlight the interception of the lepton and proton peaks. As can be seen in the figure, the overlap of the lepton and proton peaks was significant for some ToF bars.

For each ToF-track combination, leptons were required to have $m^2 < m^2_{\text{cut}}$, and protons were required to have $m^2 > m^2_{\text{cut}}$. For particles which did not meet the criterion but were in the region where the lepton and proton peaks overlapped, the energy deposited in the scintillator from that particle was checked. If the particle landed in the m^2 overlap range and had a consistent energy deposited for the particle type, then the PID check was considered correct. Any tracks that did not meet that criterion were rejected. Since the track reconstruction software frequently returned

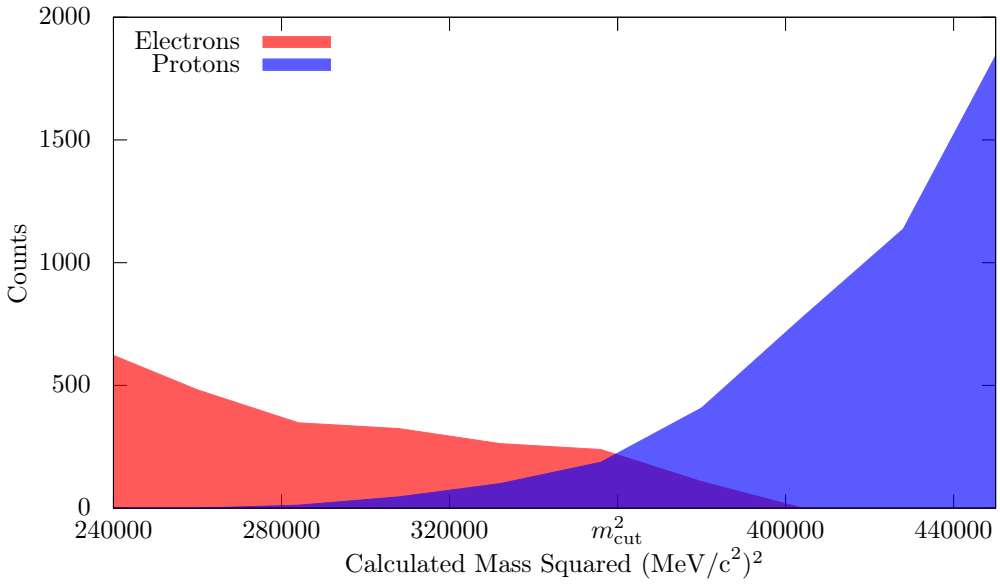

Figure 5.8: Calculated m^2 showing lepton and proton peak overlap.

both a lepton and a proton track for each pattern, this helped reject the tracks that did not match the ToF data. The large m^2 overlap was to allow for particles for which the reconstructed mass was between $0.25\,(\text{GeV/c}^2)^2$ and $0.4\,(\text{GeV/c}^2)^2$ to not be immediately rejected. However, for the downstream ToF bars in each sector, the overlap between positrons and protons during positron-beam running was large. The tighter requirements limited the amount of track candidates selected with the incorrect PID.

Even with the relaxed requirements on the ToF PID, the distributions were easily sorted into lepton and proton groups as shown in Figures 5.9 and 5.10. Shown in Figures 5.9(a-c) are the distributions for the energy deposited in the scintillator as a function of the particle's momentum. In Figure 5.10(a-c) is the time-of-flight of the particle divided by the path length the particle traveled as a function of momentum. Because of the different masses, the distributions have two groups: one for low-mass particles (like leptons) and another for high mass particles (such as protons). The

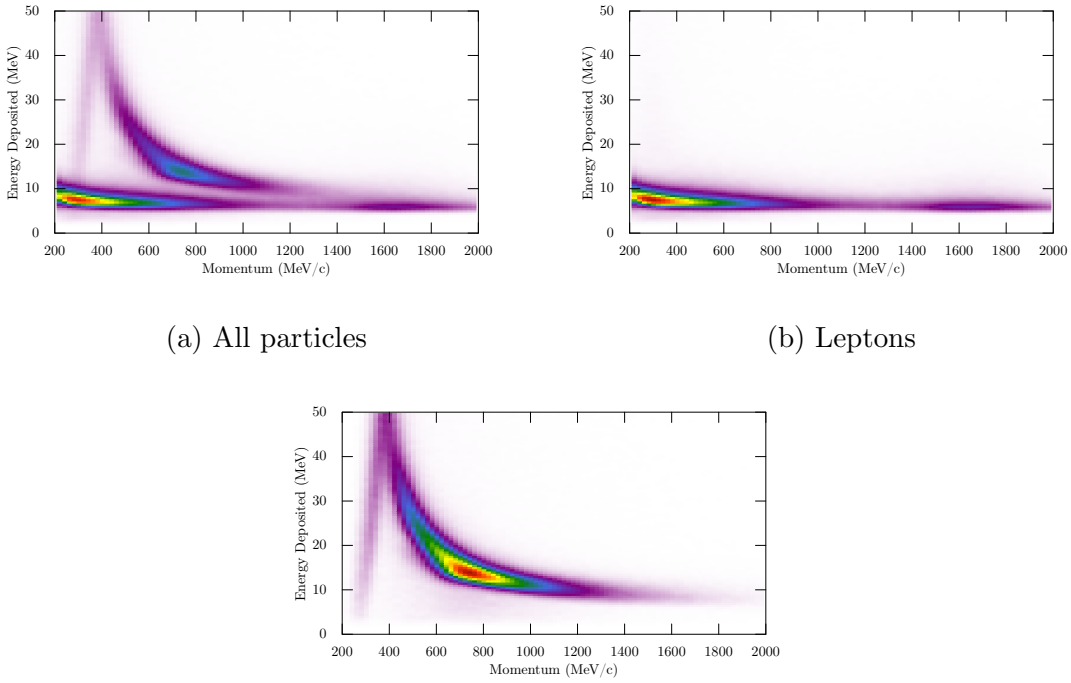

(a) All particles

(b) Leptons

(c) Protons

Figure 5.9: Energy deposited in a ToF detector versus the particle momentum. The lepton and proton peaks are distinguishable at low momentum where the protons deposited a significant amount of energy in the scintillator. For protons at high momentum however, the distribution of the energy deposited in the scintillator overlapped with the lepton distribution.

distributions shown in Figures 5.9 and 5.10 were both used to evaluate how well the PID consistency check worked.

The energy deposited in the scintillators also helped distinguish between minimum ionizing particles and protons in the region that the m^2 calculation overlapped. The energy deposited as a function of the particle's momentum is shown Figure 5.9. Minimal ionizing particles (such as $e^{\pm}$and π^{+}) are distinguishable from protons, especially at low momentum; however the particles overlap at high momentum. Because of this overlap, using the energy deposited did not prove as fruitful as the reconstructed mass

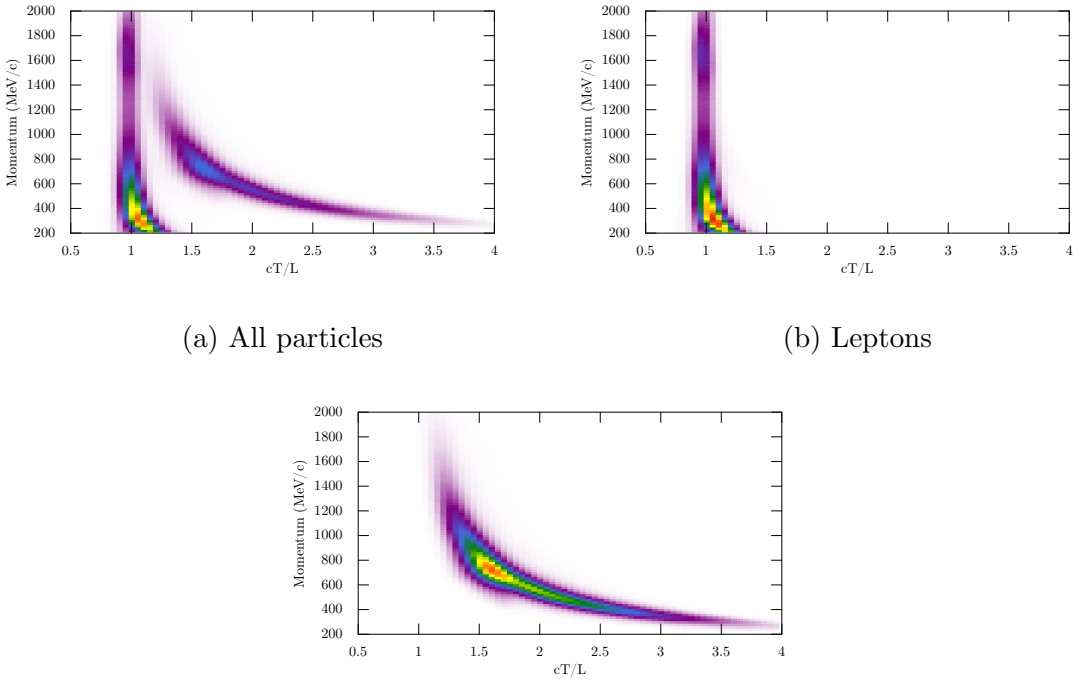

(a) All particles

(b) Leptons

(c) Protons

Figure 5.10: Distributions of the time-of-flight of the particle, divided by the amount of time it would take light to travel the same distance (cT/L) versus the momentum. For scattered leptons in the energy range covered in OLYMPUS, cT/L is very close to unity. For scattered protons however, especially low momentum events, cT/L deviates from unity significantly.

from momentum and timing for PID.

After the PID consistency checks, a ToF signal was assigned to the remaining track candidates using Equations (5.4) and (5.5). For each track, the ToF that returned the minimum of

$$(\Delta b)^2 + (\Delta y)^2, \tag{5.7}$$

was assigned to the track.

Notably, a ToF signal could be assigned to more than one track candidate per event, and a significant number of track candidates per event met the PID consistency

checks. The next step to select a track candidate in each sector was to reconstruct a scattering event, as described next.

5.2.2 Event Selection

Even after the PID consistency checks rejected some of the track candidates, there were usually more than one track candidate per sector that remained. While theoretically more than one scattering event in a bunch crossing might have taken place, the probability of multiple events was very small. To simplify the analysis, and to avoid overcounting events where many track candidates had been produced from the data, only one track per sector per event was assumed to be the correct track, and any other tracks were rejected.

For this section and the result, most parameters and figures are shown as a function of Q^2. Because of the magnetic field, positrons and electrons with the same scattering angles did not take identical paths through the detector. Any position-dependent efficiencies or reconstruction-species dependence could increase the uncertainty in Q^2 if Q^2 were calculated from the lepton parameters. To minimize this, Q^2 was calculated from the scattered proton kinematics as given by

$$Q^2\left(\theta_p\right) = \frac{4m_p^2 E_{\text{beam}}^2 \cos\left(\theta_p\right)}{m_p^2 + 2E_{\text{beam}} m_p + E_{\text{beam}}^2 \sin\left(\theta_p\right)}, \tag{5.8}$$

where θ_p is the polar angle of the proton, E_{beam} was the beam energy and m_p was the actual mass of the proton. Also discussed in this section are additional the lepton (and proton) scattering parameters $\theta_{e(p)}$, $\varphi_{e(p)}$, $p_{e(p)}$, $z_{e(p)}$ and the mass of positrons or electrons m_e.

After cutting on events which passed the main ToF and drift chamber triggers, the two track candidates from which the scattering event was reconstructed were selected. The first step was to remove the tracks with obvious nonphysical parameters.

This included rejecting all tracks with momentum outside of $10 < p < 3500$ MeV/c, and a reconstructed vertex position well outside the target cell, $-350 < z < 350$ mm. With the tracks that passed these cuts, the track selection was performed by iterating through all possible track candidates left-right sector combinations and selecting tracks based on kinematic relations. For positron-beam data, only track combinations for which both particle's curvature identified them as positively charged were kept. This reduced the Møller scattering background in the chambers significantly and helped remove track candidates reconstructed with the wrong charge. For electron-beam data, all track combinations required one negatively-charged particle and one positively-charged particle.

For all remaining track candidate left-right combinations, the event with the best vertex position agreement and the same calculated interaction time was selected. The time of the scattering was calculated using the ToF timing and tracking information. The interaction time, t_0 is

$$t_0 = t_{\mathrm{ToF}} - \frac{L_{\mathrm{path}}}{\mathrm{c}}\sqrt{\left(\frac{m^2}{p^2}+1\right)} + \frac{z}{\mathrm{c}}, \tag{5.9}$$

where L_{path} is the length the particle traveled from the target to the ToF; m is the mass of the particle, assuming the PID from the tracker was correct; and p is the momentum. The factor of z/c accounted for the time needed for the beam bunch to go from the beam reference clock to the scattering vertex in the target.

For the track candidates in both sectors, t_0 was calculated and the difference between them $\Delta t_0 = t_0^L - t_0^R$ found. Δt_0 is shown as a function of Q^2 in Figure 5.11. The distribution of Δt_0 was binned as a function Q^2 and fitted with a Gaussian function. Figure 5.11 also shows the mean (the bold line) and $\pm 1\sigma$ (the thinner lines) of those Gaussian fits. The t_0 distributions for data have a larger variance. Despite smearing in the Monte Carlo, the track reconstruction generally still performed better

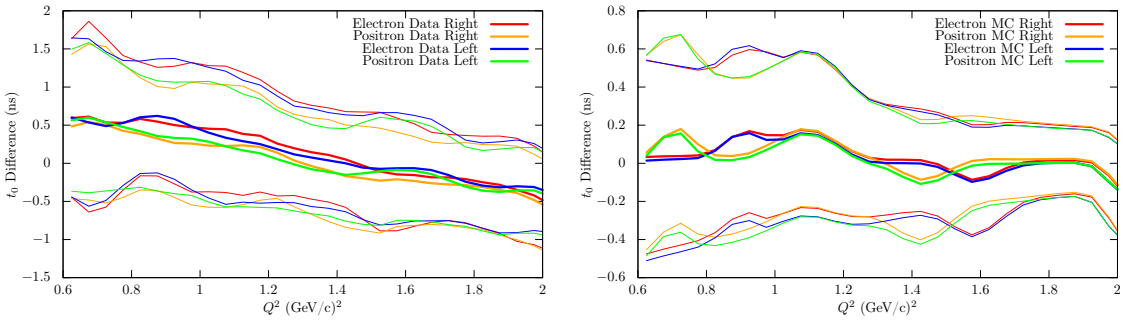

(a) Data (b) Monte Carlo

Figure 5.11: The $\varphi = \varphi_{\text{lepton}} + \varphi_{\text{proton}}$ as a function of four-momentum transfer. The bold line is the mean and the thin lines show $\pm 1\sigma$.

on Monte Carlo data than on real data, probably due to errors in the time-to-distance function and imperfect time-delays in the detector calibration.

To check the vertex correlation between the two track candidates, the vertex position difference

$$\Delta z = z^L - z^R, \tag{5.10}$$

was calculated. These distributions as a function of Q^2 are shown in Figure 5.12. The simulated spread in the vertex position difference corresponded closer to that observed in data, with a one-sigma spread generally about one centimeter.

With the means and standard deviations for the timing correlation μ_{t_0} and σ_{t_0}, and the vertex position correlation μ_z and σ_z, the best track combination was selected. The track combination was selected by picking the two tracks that minimized

$$\Delta_{t_0:z} = \left(\frac{\Delta t_0 - \mu_{t_0}}{\sigma_{t_0}} \right) + \left(\frac{\Delta z - \mu_z}{\sigma_z} \right). \tag{5.11}$$

After the track candidates were selected, the events that looked to be elastic scattering were selected from background events. First, events were selected that had one proton and one lepton. A high rate of events were found where both particles reconstructed as leptons. These were either low-energy lepton backgrounds or pion

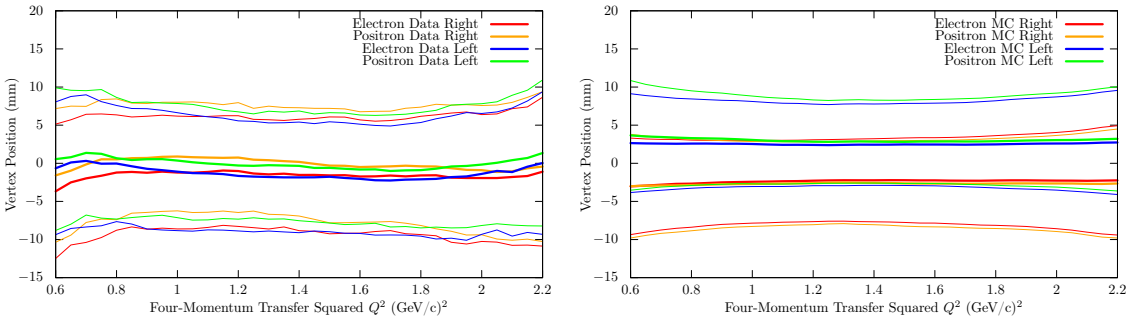

(a) Data (b) Monte Carlo

Figure 5.12: The $\varphi = \varphi_{\text{lepton}} + \varphi_{\text{proton}}$ as a function of four-momentum transfer. The bold line is the mean and the thin lines show $\pm 1\sigma$.

electroproduction, where a π^+ was produced. Very wide cuts, as described next, were then applied to the lepton-proton scattering events to help eliminate some of the background events. These cuts were on the azimuthal angle and scattering angle correlations between the particles and on the reconstructed beam energy.

Momentum conservation for elastic scattering required both the lepton and proton lie in the same scattering plane, which was checked by comparing the azimuthal scattering angles between the particles. If an event was elastic, the azimuthal angle for the lepton φ_e, and the azimuthal angle for the proton φ_p, should be of equal magnitude and of opposite sign, $\varphi_e + \varphi_p = 0$. The azimuthal angle correlation for all tracks which had a lepton and a proton is shown in Figure 5.13 for both data and the Monte Carlo simulation. The φ correlation for both real and simulated events was narrow, with a standard deviation of less than 0.5°. The distributions for the left and right sectors of the detector diverged toward the edges of the acceptance at $Q^2 = 0.6$ (GeV/c)^2 and $Q^2 = 2.4$ (GeV/c)^2. In these regions, the hard acceptance edge of the drift chambers pushed the distribution away from zero.

The scattering polar angles of the two particles are also correlated for elastic

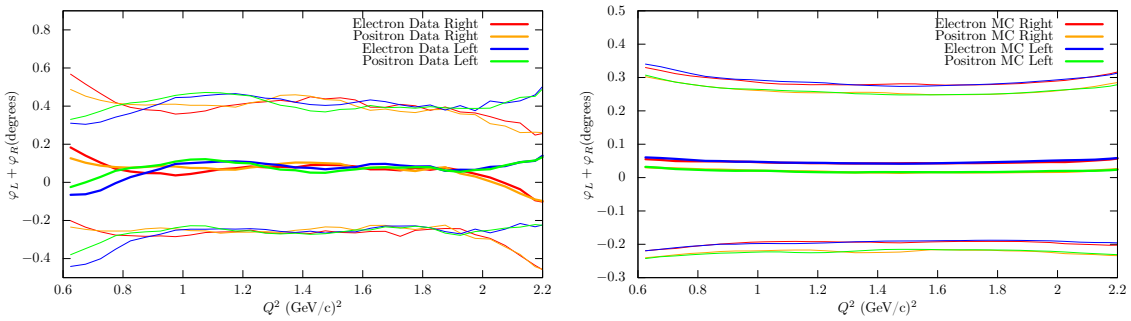

(a) Data

(b) Monte Carlo

Figure 5.13: The $\varphi = \varphi_{\text{lepton}} + \varphi_{\text{proton}}$ as a function of four-momentum transfer. The bold line is the mean and the thin lines show $\pm 1\sigma$.

scattering so that the proton polar angle θ_p can be determined from the lepton polar angle θ_e:

$$\theta_p(\theta_e) = \tan^{-1}\left(\frac{-p_e \sin(\theta_e)}{\sqrt{(E_{beam}^2 - m_e)} - p_e \cos(\theta_e)}\right), \tag{5.12}$$

where $p_e = \sqrt{E_e' - m_e^2}$ is the momentum of the scattered lepton as determined from the scattering angle. The energy of the scattered lepton E_e', is given as

$$E_e'(\theta_e) = \frac{E_{\text{beam}} m_p}{m_p + E_{\text{beam}}(1 - \cos\theta_e)}. \tag{5.13}$$

By examining the difference between the measured proton scattering angle θ_p^{meas} to the proton scattering angle as calculated from the lepton scattering angle $\theta_p(\theta_e)$

$$\Delta\theta_p = \theta_p^{\text{meas}} - \theta_p(\theta_e), \tag{5.14}$$

elastic events were determined. The distributions of polar angle correlation $\Delta\theta$ as a function of Q^2 are shown in Figure 5.14. The simulated data are more tightly correlated than the real data, but both distributions show $\Delta\theta$ to be fairly stable over the Q^2 range.

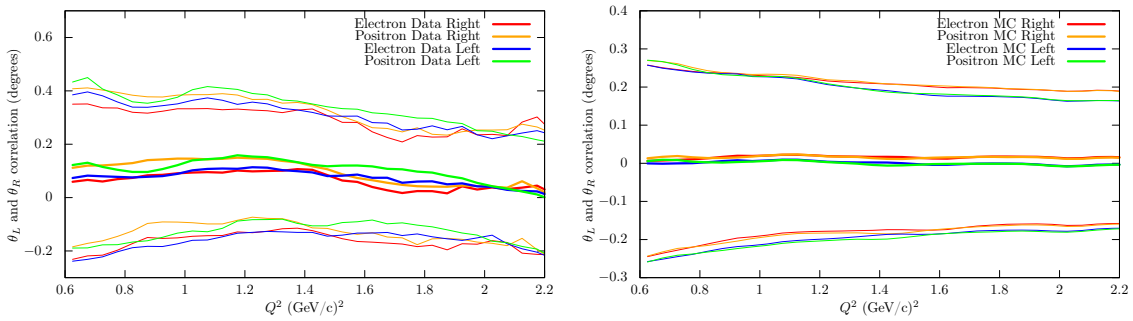

(a) Data (b) Monte Carlo

Figure 5.14: The difference between the measured proton angle θ_p and the proton angle calculated from the electron scattering angle θ_e with elastic kinematics. The bold line is the mean and the thin lines show $\pm 1\sigma$.

The cuts that were made on $\Delta\theta$ and $\Delta\varphi$ were not meant to completely separate the background events from the elastic scattering events. Instead, these cuts were intended to increase the signal-to-noise ratio of the sample while retaining as many elastic events as possible. Because of the large uncertainties in the reconstructed track parameters, the cuts were fairly wide: $\Delta\varphi \in (-8°, 8°)$ and $\Delta\theta \in (-8°, 8°)$.

Another cut to help eliminate background events used the reconstructed beam energy. Using the momentum of the tracks p_p and p_e for the proton and lepton, respectively, and trusting the PID of the track, the beam energy can be reconstructed as

$$E^{\mathrm{R}}_{\mathrm{beam}}(p_e, p_p) = \sqrt{(p_e^2 + m_e^2)} + \sqrt{(p_p^2 + m_p^2)} - m_p. \tag{5.15}$$

The reconstructed beam energy helped separate a large background of low momentum events from the elastic peak, which grew at larger Q^2. At an intermediate range of $Q^2 \in (0.9, 0.95)(\mathrm{GeV/c})^2$, the calculated beam energy is shown in Figure 5.15. This distributions shows the elastic peak at about 2 GeV, which was the actual beam energy. Figure 5.15 also shows a large amount of low-momentum background events with a calculated beam energy far below that of the actual beam.

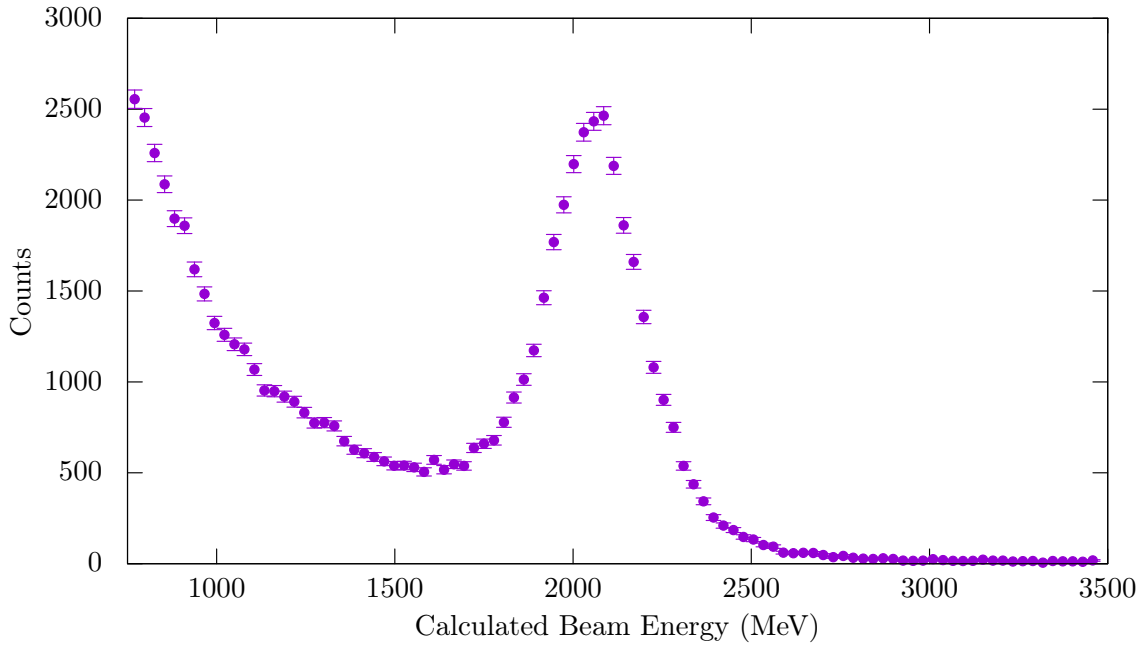

Figure 5.15: The calculated beam energy using the momentum as found with the track reconstruction. This was calculated using Equation (5.15). The elastic peak is shown at 2 GeV and there is a large background of events where the calculated beam energy is too low.

A cut at $E^{\mathrm{R}}_{\mathrm{beam}}(p_e, p_p) = 1.2$ GeV removed a significant portion of the low-momentum background while not being in danger of cutting out any of the elastic peak. After these very wide cuts, the scattering events were sorted into bins of $\Delta Q^2 = 0.05(\mathrm{GeV/c})^2$ from $Q^2 = 0.6(\mathrm{GeV/c})^2$ to $Q^2 = 2.4(\mathrm{GeV/c})^2$.

To increase the signal-to-noise ratio further before background subtraction, for each Q^2 bin the beam energy as reconstructed from the scattering angle was fit to a Gaussian distribution, and events outside $\pm 4\sigma$ were rejected. The beam energy reconstructed from scattering angle is given as

$$E^{\mathrm{R}}_{\mathrm{beam}}(\theta_e, \theta_p) = E'_e(\theta_e) + E'_p(\theta_p) - m_p, \tag{5.16}$$

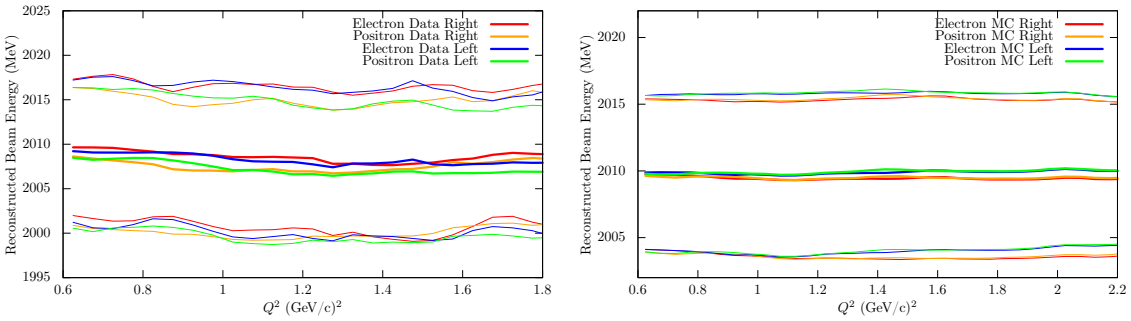

(a) Data (b) Monte Carlo

Figure 5.16: The reconstructed beam energy using the polar angles of the scattered particles, θ_p and θ_e. The bold line is the mean and the thin lines show $\pm 1\sigma$.

where the energy of the proton as calculated from θ_p is

$$E_p^{'}(\theta_p) = \frac{2E_{\text{beam}} m_p \cos(\theta_p)(E_{\text{beam}} + m_p)}{E_{\text{beam}}^2 \sin^2(\theta_p) + 2E_{\text{beam}} m_p + m_p^2} \tag{5.17}$$

and the energy of the scattered lepton is given in Equation 5.13. Because of the better angular resolution, this distribution was more sharply peaked around E_{beam}. The reconstructed beam energy as a function of Q^2 also proved to have a consistent mean and standard deviation, as shown in Figure 5.16. The reconstructed beam energy from scattering angle, peaked around 2.01 GeV, and the standard deviation remained constant over the entire Q^2 range.

Figure 5.16 shows that the reconstructed beam energy was constant with respect to Q^2. Therefore, this provided another method to filter out inelastic events. For this cut, which was the tightest, the calculated beam energy from proton and lepton angles was fit with a Gaussian distribution, and cut at $\pm 4\sigma$. This significantly decreased the inelastic background events, as shown in Figure 5.17.

Once the cuts in the scattering angle corrections $\Delta\theta$ and $\Delta\varphi$ and the reconstructed beam energy were made, the remaining inelastic background events were subtracted for each Q^2 bin.

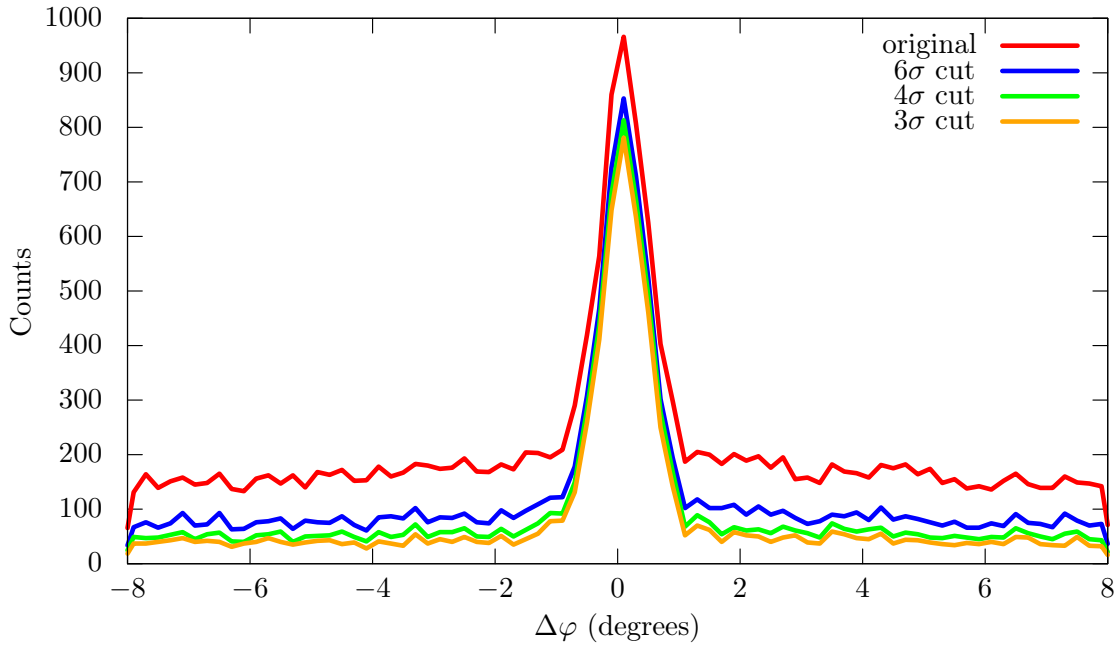

Figure 5.17: The $\Delta\varphi$ correlation before and after cuts on the reconstructed beam energy, for a large Q^2 bin. At large Q^2 where the inelastic backgrounds were highest, cutting on the reconstructed beam energy significantly increased the signal to background ratio.

5.2.3 Background Subtraction

The dominant background events present after track selection and elastic cuts were low-energy lepton background events. The source of these background events was never well identified, but that background appeared to be coming from the same scattering vertex in the target. Initially these background events were considered to be pion electroproduction or stray Møller events; however, the missing mass for these events was not consistent with either of those processes. Since these background events were not discovered until after all the data were taken, instead of attempting to identify the backgrounds and remove them, this background was subtracted from the elastic scattering signal.

Fortunately, the lepton background did not follow elastic kinematics and was sub-

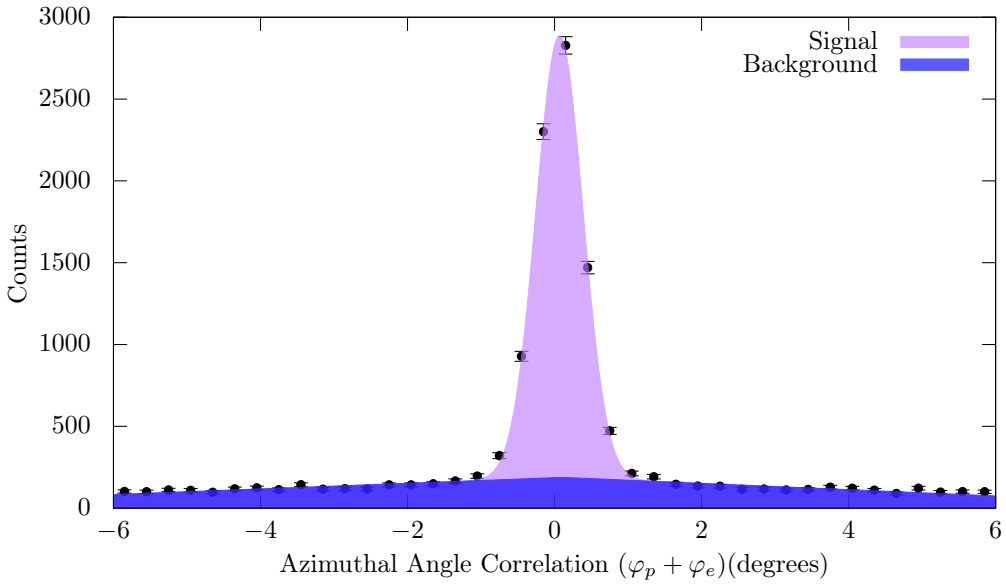

Figure 5.18: The $\Delta\varphi$ correlation for events in Q^2 bin from $1.0 < Q^2 > 1.05$. The triangular background function is shown in dark blue and the Gaussian peak of elastic events is shown in purple.

tracted for each Q^2 bin using the calculated beam-energy-correlation and theφ- and θ-correlation plots. The distribution of $\Delta\varphi = \varphi_p + \varphi_e$ revealed the elastic peak residing on a triangular background, as shown in Figure 5.18, where the $\Delta\varphi$ distribution is shown for a small range of Q^2. The Gaussian peak is visible in purple and the background function is shown in blue.

To remove the background events, the $\Delta\varphi$ distributions for each bin in Q^2 were fit with a Gaussian function plus a triangular function as

$$f(\Delta\varphi) = A\exp\left(-\frac{1}{2}\left(\frac{\Delta\varphi - \mu_\varphi}{\sigma_\varphi}\right)^2\right) + \begin{cases} b + m_0(\Delta\varphi) & : \Delta\varphi < x_0, \\ b + m_1(\Delta\varphi) & : \Delta\varphi > x_0. \end{cases} \tag{5.18}$$

To find the rate of remaining elastic events in each Q^2 bin, the fit parameters from the triangular function were used to estimate the background for each value of $\Delta\varphi$. For each $\Delta\varphi$ distribution, as shown in 5.18, the number of counts in each was reduced

by the estimated background rate. The counts from each bin were then summed over a range of $\Delta\varphi$ from $-5^\circ < \Delta\varphi < 5^\circ$.

The background subtraction method proved to provide stable results, as discussed in Chapter 6. The two parameters that had the largest effect on the background fraction were the cut on reconstructed beam energy, Eq (5.16), and the range in $\Delta\varphi$. The results were obtained for a range of these parameters, which allowed for their influence on the result to be quantified, as is discussed in the next chapter.

After the completion of the particle identification, the event selection, and the background subtraction, the rates for each bin in Q^2 were used to calculate the positron-proton to electron-proton elastic scattering cross section ratio, as discussed in the next chapter.

Chapter 6

CROSS SECTION RATIO RESULTS

In this chapter, the preliminary results for the cross section ratio are presented. The positron-proton to electron-proton elastic scattering cross section ratio was calculated from the rates, observed in data and simulated in Monte Carlo, as a function of four-momentum transfer Q^2 as

$$R_{2\gamma} = \frac{d\sigma_{e^-p}}{d\sigma_{e^+p}} = \mathcal{L}^{\mathrm{MIE}}_{\mathrm{Ratio}} \frac{N^{\mathrm{Data}}_{e^+p}}{N^{\mathrm{Data}}_{e^-p}} \left(\frac{N^{\mathrm{MC}}_{e^-p}(\mathcal{L}^{\mathrm{SC}}_{e^-p})}{N^{\mathrm{MC}}_{e^+p}(\mathcal{L}^{\mathrm{SC}}_{e^+p})} \right). \tag{6.1}$$

The relative luminosity correction $\mathcal{L}^{\mathrm{MIE}}_{\mathrm{Ratio}}$ was taken from the Multi-Interaction Event (MIE) analysis; this is the correction to the slow control (SC) luminosity given as

$$\mathcal{L}^{\mathrm{Ratio}}_{\mathrm{MIE}} = \frac{\mathcal{L}^{\mathrm{MIE}}_{e+p}}{\mathcal{L}^{\mathrm{MIE}}_{e-p}} \frac{\mathcal{L}^{\mathrm{SC}}_{e-p}}{\mathcal{L}^{\mathrm{SC}}_{e+p}}. \tag{6.2}$$

The luminosity correction was found to be $\mathcal{L}^{\mathrm{Ratio}}_{MIE} = 1.006 \pm 0.003$, as described in Section 4.4.3. Because the Monte Carlo rates were generated assuming the slow control luminosity, the MIE correction to the slow control luminosity was used to normalize the ratio. In this chapter, the ratio results as a function of Q^2 and the virtual-photon polarization ϵ (Equation (2.12)) will be presented and preliminary systematic uncertainty studies discussed.

6.1 Results

After the elastic event selection and inelastic background subtraction were made, good agreement existed between the Monte Carlo rate and the data rate for both electron-proton and positron-proton scattering over a wide range of Q^2. These rates are shown in Figure 6.1. The rates for the lepton scattering into the left and right

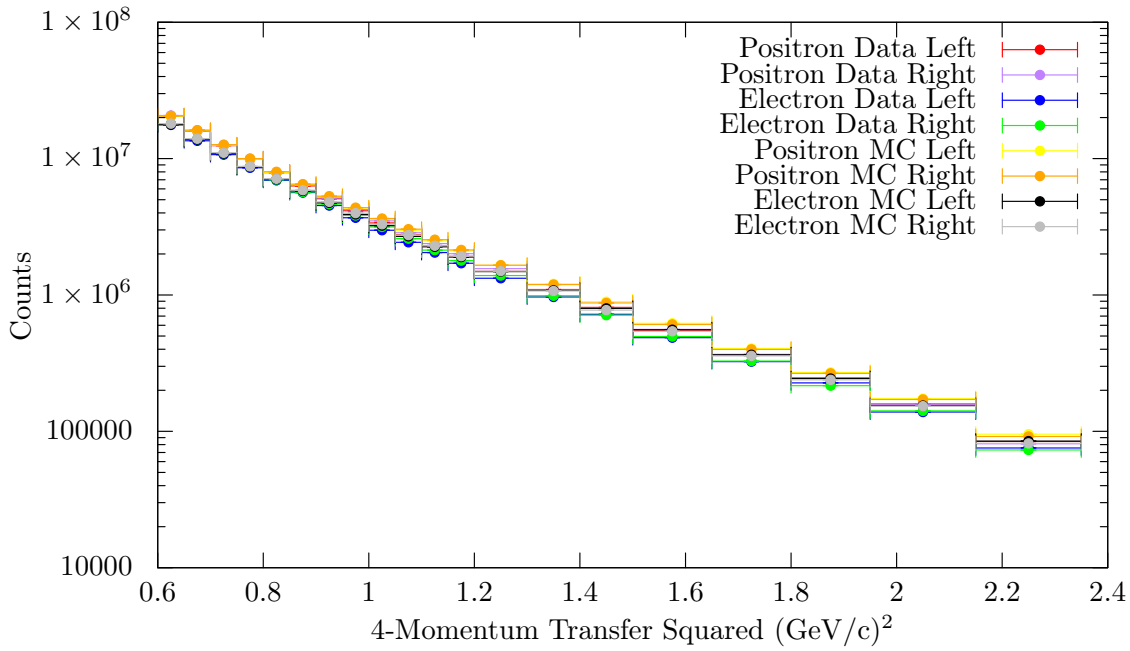

Figure 6.1: Comparison of the rates as a function of Q^2 for both data and Monte Carlo. The rates are given for both the left and right sectors of the detector separately.

sectors of the detector are given separately, and are binned in groups of $Q^2 = 0.5(\mathrm{GeV/c})^2$ for low Q^2. For high Q^2, bins were combined to decrease the statistical uncertainty for those points.

By combining the data rates measured in the left and right sectors of the detector and normalizing by the Monte Carlo and the relative luminosity, the cross section ratio, $R_{2\gamma}$ was calculated from Equation (6.1). The ratio is shown in Figure 6.2, where the error bars are from statistical uncertainties and do not include any systematic uncertainties. The gray rectangle on the plot shows the calculated uncertainty from the MIE luminosity normalization. The distribution of $R_{2\gamma}$ starts slightly below one at low Q^2 and increases at large Q^2. However, at large Q^2 the cross section ratio remains statistically consistent with unity and the slope is shallow. $R_{2\gamma}(Q^2)$ shows an approximate rise of 1%-2% from $Q^2 = 0.6\,(\mathrm{GeV/c})^2$ to $Q^2 = 2.2\,(\mathrm{GeV/c})^2$. For this

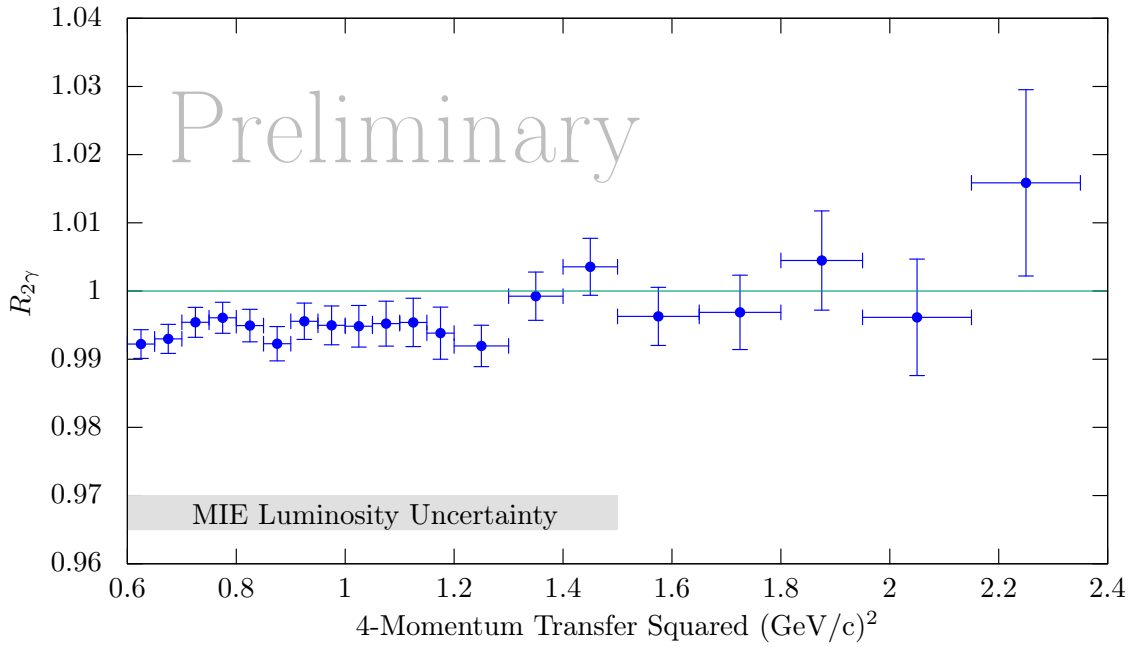

Figure 6.2: The preliminary results for the positron-proton to electron-proton elastic scattering cross section ratio $R_{2\gamma}$ as a function of Q^2. The relative luminosity is taken from the MIE analysis, and the uncertainties in the MIE analysis luminosity are shown in the light gray bar. The uncertainties shown for each point include the statistical uncertainty only.

figure, the Monte Carlo radiative corrections used the form factor fit from (Bernauer *et al.*, 2014b) and only lepton contributions to the vacuum polarization, as described in Section 5.1.1.

Changing from Q^2 to ϵ, as given by Equation (2.12) in Chapter 1, the results from this analysis are plotted in comparison to the theory curves discussed in Section 2.2.1 in Figure 6.3. The data from this analysis show good agreement with Afanasev *et al.* (2005), and also are consistent with Bernauer *et al.* (2014b) at low Q^2. Also, shown in Figure 6.3 is the cross section ratio result measured by the 12° telescopes, as disucssed in Henderson (2016).

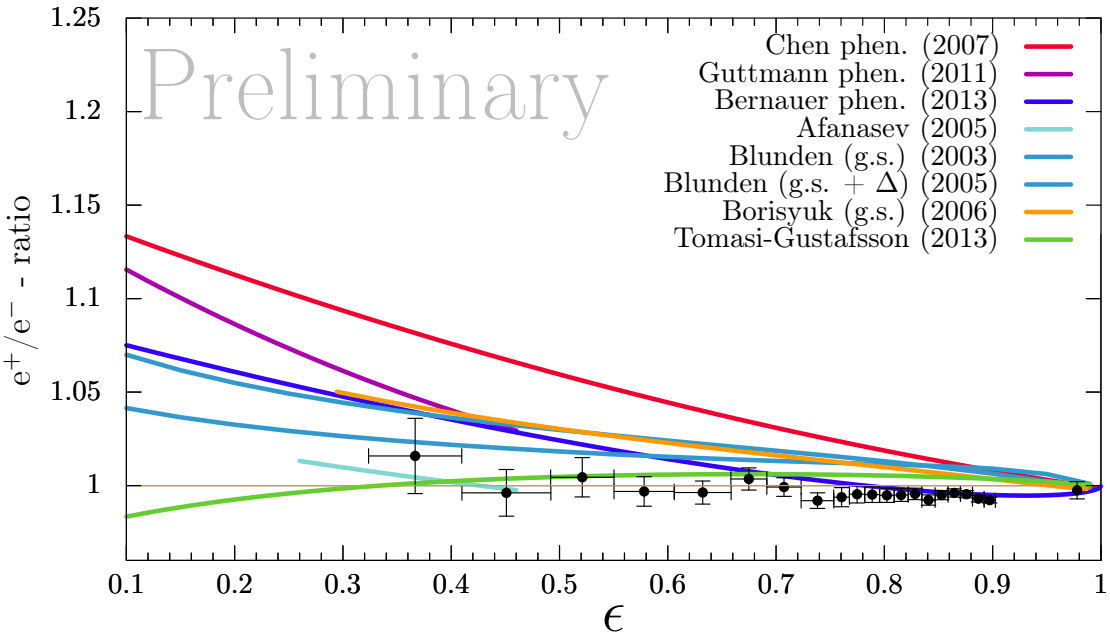

Figure 6.3: The cross section ratio as a function of ϵ plotted with theory curves from Afanasev *et al.* (2005), Blunden *et al.* (2003), Blunden *et al.* (2005), Borisyuk and Kobushkin (2006), and Tomasi-Gustafsson *et al.* (2013). Also shown are phenomenological models from Chen *et al.* (2007), Guttmann *et al.* (2011), and Bernauer *et al.* (2014b).

6.2 Systematic Uncertainties

The study of the systematic uncertainties that contribute to the calculation of $R_{2\gamma}$ is extremely important, as the systematic uncertainty is expected to be larger than the statistical uncertainty at most points. At low Q^2, the elastic electron-proton and positron-proton cross sections are large, corresponding to high rates and low statistical uncertainty in the measurement. However, the elastic cross section declines quickly with Q^2, resulting in high statistical uncertainty in the last few bins in Q^2. Sources and approximate magnitudes of the systematic uncertainties discussed in this section are listed in Table 6.1. The estimated systematic uncertainty in the cross section measurement is calculated to be $\pm 1.53\%$, but a more realistic estimate

Uncertainty	Estimated Uncertainty
Track and detector efficiency	1%
Reconstructed beam energy cut	0.5%
$\Delta\varphi$ cut	0.1%
MIE Luminosity	0.27%
Radiative correction	1%
Total	1.53%

Table 6.1: The systematic uncertainties in $R_{2\gamma}$ discussed in this section.

is ±2%. The estimate of ±1.53% is based on this analysis only, and many potential sources of uncertainty are not included in this estimate. A more thorough study of the systematic uncertainties will be produced for the final OLYMPUS result. This will include comparisons of several independent analyses of the data and a thorough study of the radiative correction effect on the ratio.

The first source of the systematic uncertainty is in the luminosity determination, as discussed in Section 4.4.3. The luminosity normalization was determined by the Multi-Interaction Event analysis to be 1.006 ± 0.003, (Schmidt, 2016). This is consistent with the 12° luminosity determination, which was calculated as 1.001 ± 0.005. The uncertainties from the MIE analysis has been included in Figures 6.2 and 6.5 as a gray bar along the bottom of the figures.

Several other sources of uncertainty stem from tracking and detector inefficiencies, which can be estimated with the ratio of left and right yields, as shown in Figure 6.4. That figure reveals inefficient regions in both sectors of the detector, and the attempt to simulate the inefficient regions with the Monte Carlo techniques. The increase at $Q^2 = 1$ $(\mathrm{GeV/c})^2$ and the slight decrease at $Q^2 < 1.4$ $(\mathrm{GeV/c})^2$ are a

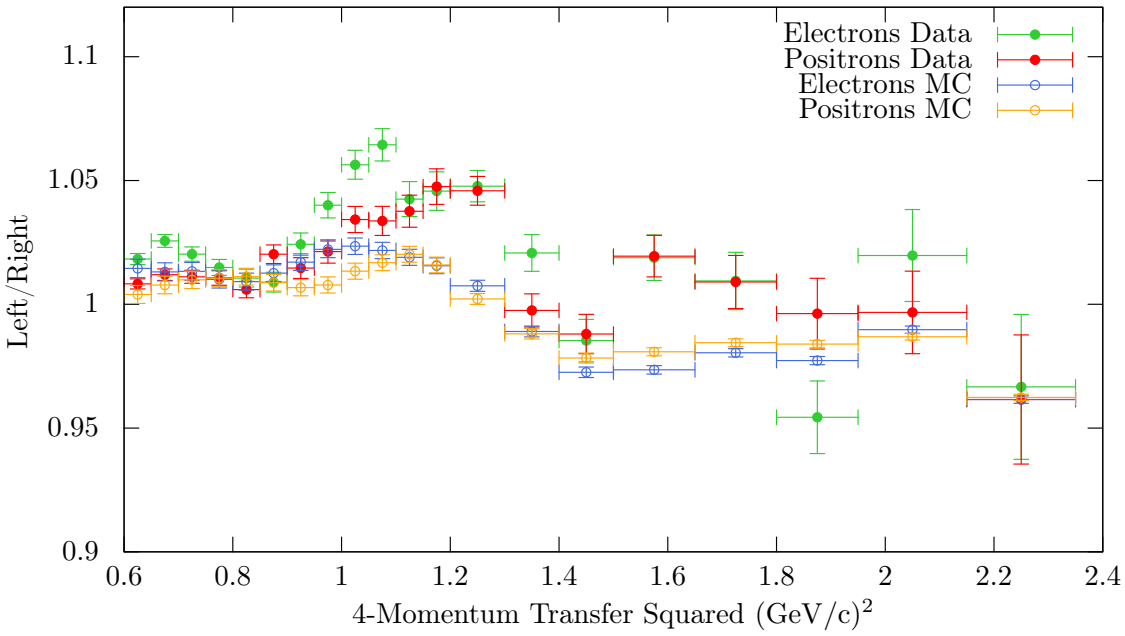

Figure 6.4: The ratio of yields from leptons scattered into the left sector to leptons scattered in the right sector of the detector.

result of the lepton or proton, respectively, scattering into a region of the left sector with a large inefficient region in one of the drift chambers. The efficiency maps (as discussed in Section 5.1.3) and the method of determination (as described in Henderson (2016)) attempt to reproduce these features in the Monte Carlo simulation. While the simulation shows the same trend as the data, the simulation does not fully reproduce the inefficient region. By measuring the ratio where the lepton scattered into the left sector and the right sector separately, the effect of the inefficient region can be seen in the result, as shown in Figure 6.5.

There is some deviation between the ratio as measured from the left and right sectors of the detector, but overall the results are statistically consistent for most points. The right sector tended to have a larger ratio at low Q^2, as shown in Figure 6.5. While this does not completely cover the uncertainties from track reconstruction and

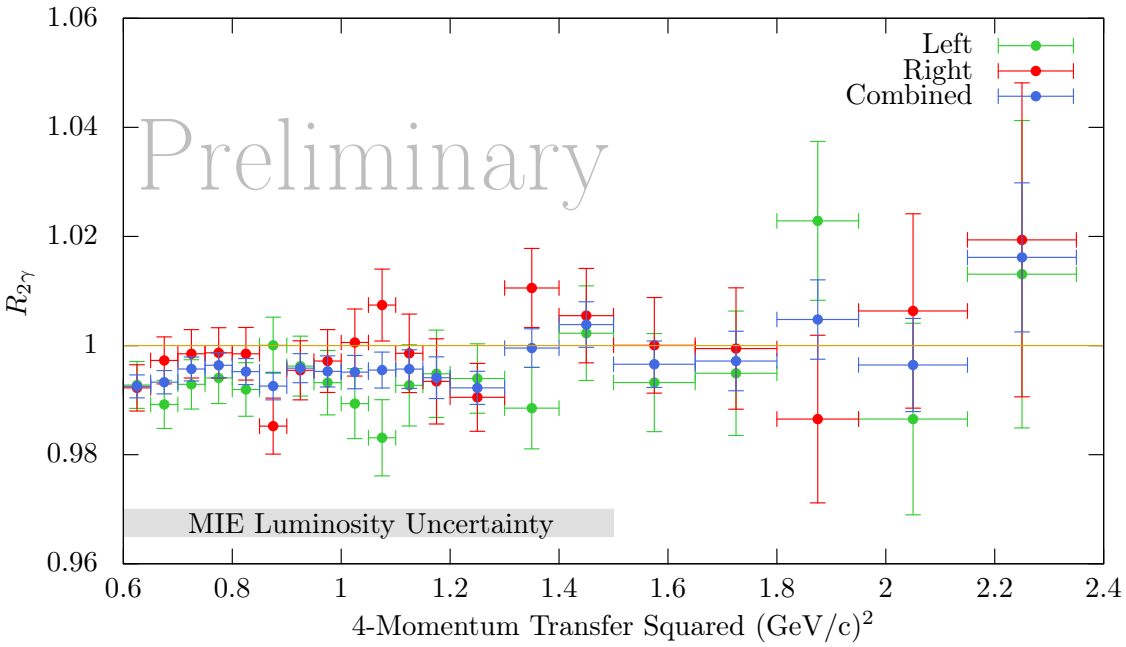

Figure 6.5: The cross section ratio, $R_{2\gamma}$ as determined where the lepton is scattered into the left, green, or right, red, sector of the detector. The combined left and right result is also shown in blue.

the detector efficiency, the comparison provides a reasonable estimate. The deviation between the left and right sectors of the detector is approximately 1% for most Q^2 values.

Several methods are available to understand the effect of the analysis and background subtraction. The best approach is to compare with the independent analyses of Henderson (2016), Schmidt (2016), and Russell (2016) with the analysis presented in this thesis. These analyses for the track selection, PID, and background subtraction were developed independently and therefore, provide a better estimate of the systematic uncertainties due to the analysis method. A comparison of these analyses will be produced for the final result. In this thesis, the analysis and background subtraction effect on the ratio is estimated by repeating the analysis with different cuts and background subtraction methods. By varying the cuts made on the reconstructed beam

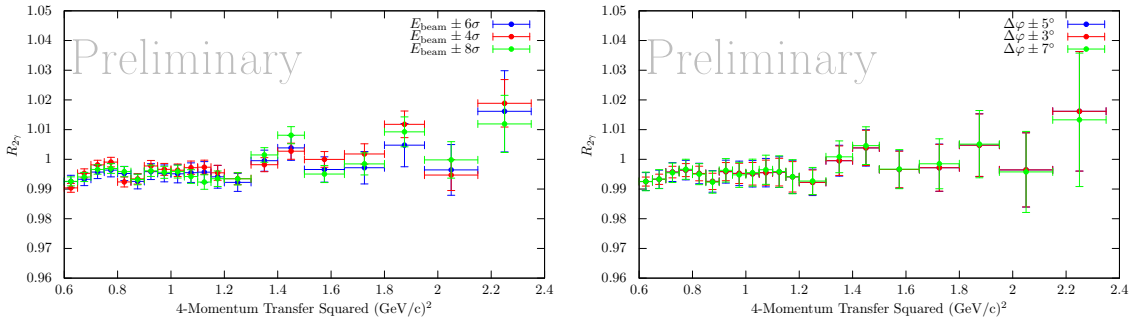

(a) φ range

(b) Reconstructed beam energy cuts

Figure 6.6: The cross section ratio with several different analysis cuts. The first shows a variation on the range of $\Delta\varphi$ included in the yields. The second shows how the cuts on the reconstructed beam energy change the ratio.

energy, described in Section 5.2.3, the results shown in Figure 6.6b were produced, which indicates the variation in the beam energy cut corresponded to shifts in the ratio by approximately 0.5%. Another variable in the background subtraction was the $\Delta\varphi$ range, as shown in Figure 5.18, over which events were summed to produce the yield. By varying this range and reproducing the result, an estimate of this effect on the cross section ratio is produced, as shown in Figure 6.6a. The ratio proved robust to the variation of the $\Delta\varphi$ cuts, and the observed change was on order a tenth of percent. Generally, as shown in Figure 6.6, $R_{2\gamma}$ did not have a strong dependence on those cuts.

While both these variations had a significant effect on the cross section ratio, the underlying background subtraction procedure used was the same. To better estimate the uncertainty from the PID, track selection, and background subtraction steps, a comparison of the independent analyses is required.

For this analysis, a conservative additional 1% systematic uncertainty from the radiative corrections was estimated. Adding the uncertainties in quadrature, the overall systematic uncertainty was brought to 1.5%. This result is very preliminary.

Further studies on the systematic errors for the final result will include a comparison of independent track selection and background subtraction algorithms. Also, a thorough study of the effect of the radiative corrections on the ratio needs to be carried out.

6.3 Discussion

While this analysis shows a slight upward trend in $R_{2\gamma}$ at larger Q^2, the results are consistent with unity. These results reveal a smaller two-photon contribution than what was revealed with the other two modern experiments, (Rachek *et al.*, 2015), (Rimal *et al.*, 2016) and (Adikaram *et al.*, 2015). However because of the large uncertainties at high Q^2 and the limited range of the experiment, the results are generally consistent within the uncertainty bounds. The results agree with several theory curves, as shown in Figure 6.3. While these results do not provide evidence for a large two-photon exchange contribution, the results do not rule out the possibility that two-photon exchange is the cause of the form factor ratio discrepancy.

The results shown in this thesis are preliminary and at this time, the studies on the systematic uncertainties are ongoing. Before a final result of the cross section ratio can be published, a full systematic uncertainty study comparing the several independent analyses of the data needs to be produced. The effect of the radiative corrections on the cross section ratio also needs to be studied in detail.

Chapter 7

CONCLUSION

In 2000, new measurements using polarized electron-proton scattering at Jefferson Lab showed a large decrease in the electric-to-magnetic form factor ratio of the proton at large four-momentum transfer Q^2. This result revealed a significant deviation from the form factor measurements made with the Rosenbluth separation technique on data from unpolarized electron-proton scattering. The results from Jefferson Lab were reproduced by several independent experiments and continued to show the decreasing trend in the form factor ratio. New experiments using the Rosenbluth technique proved consistent with the old measurements, and the discrepancy between the two methods persisted. This discrepancy threw into question the validity of the one-photon exchange assumption made in both experimental techniques. A significant two-photon exchange amplitude to the electron-proton scattering cross section could resolve the discrepancy. However, the exact size of the contribution from two-photon exchange was unknown.

A method to experimentally determine the size of the two-photon exchange correction to electron-proton scattering was needed. The OLYMPUS experiment was designed to measure the two-photon exchange contribution to elastic electron-proton scattering, was achieved by measuring the positron-proton to electron-proton elastic scattering cross section ratio $R_{2\gamma} = \frac{d\sigma_{e+p}}{d\sigma_{e^-p}}$ as a function of Q^2. In addition to the OLYMPUS experiment, the cross section ratio was also measured by CLAS and the VEPP3 experiments.

The OLYMPUS experiment measured the cross section ratio $R_{2\gamma}$ over a range of $0.6 < Q^2 < 2.2$ (GeV/c)^2. The preliminary result presented in this thesis shows a

slight rise in $R_{2\gamma}$ of 1%-2% over the range of Q^2 covered by OLYMPUS. While this result does not provide strong evidence for a two-photon exchange contribution to elastic lepton-proton scattering, the result does not completely rule out two-photon exchange as the culprit for the electric-to-magnetic form factor discrepancy. An experiment to a higher value of Q^2 could determine if the two-photon exchange is the cause of the discrepancy. The analysis for the final OLYMPUS result, and the studies of the systematic uncertainties in the result, are ongoing at this time.

REFERENCES

Actis, S., A. Arbuzov, G. Balossini, P. Beltrame, C. Bignamini, R. Bonciani, C. C. Calame, V. Cherepanov, M. Czakon, H. Czyż *et al.*, "Quest for precision in hadronic cross sections at low energy: Monte carlo tools vs. experimental data", The European Physical Journal C **66**, 3-4, 585–686 (2010).

Adikaram, D., D. Rimal, L. Weinstein, B. Raue, P. Khetarpal, R. Bennett, J. Arrington, W. Brooks, K. Adhikari, A. Afanasev *et al.*, "Towards a resolution of the proton form factor problem: new electron and positron scattering data", Physical review letters **114**, 6, 062003 (2015).

Afanasev, A. V., S. J. Brodsky, C. E. Carlson, Y.-C. Chen and M. Vanderhaeghen, "Two-photon exchange contribution to elastic electron-nucleon scattering at large momentum transfer", Physical Review D **72**, 1, 013008 (2005).

Agostinelli, S., J. Allison, K. a. Amako, J. Apostolakis, H. Araujo, P. Arce, M. Asai, D. Axen, S. Banerjee, G. Barrand *et al.*, "Geant4a simulation toolkit", Nuclear instruments and methods in physics research section A: Accelerators, Spectrometers, Detectors and Associated Equipment **506**, 3, 250–303 (2003).

Akhiezer, A. and M. Rekalo, "Polarization phenomena in electron scattering by protons in the high-energy region", in "Soviet Physics Doklady", vol. 13, p. 572 (1968).

Akhiezer, A. and M. Rekalo, "Polarization effects in the scattering of leptons by hadrons", Tech. rep., Physicotechnical Institute, Academy of Sciences of the Ukrainian SSR, Khar'kov (1974).

Allison, J., K. Amako, J. e. a. Apostolakis, H. Araujo, P. A. Dubois, M. Asai, G. Barrand, R. Capra, S. Chauvie, R. Chytracek *et al.*, "Geant4 developments and applications", IEEE Transactions on Nuclear Science **53**, 1, 270–278 (2006).

Andivahis, L., P. Bosted, A. Lung, L. Stuart, J. Alster, R. Arnold, C. Chang, F. Dietrich, W. Dodge, R. Gearhart *et al.*, "Measurements of the electric and magnetic form factors of the proton from $Q^2 = 1.75$ to 8.83 $(\mathrm{GeV/c})^2$", Physical Review D **50**, 9, 5491 (1994).

Arnold, R., P. Bosted, C. Chang, J. Gomez, A. Katramatou, C. J. Martoff, G. Petratos, A. Rahbar, S. Rock, A. Sill *et al.*, "Measurement of elastic electron scattering from the proton at high momentum transfer", Physical Review Letters **57**, 2, 174 (1986).

Arnold, R. G., C. E. Carlson and F. Gross, "Polarization transfer in elastic electron scattering from nucleons and deuterons", Physical Review C **23**, 1, 363 (1981).

Arrington, J., "How well do we know the electromagnetic form factors of the proton?", Physical Review C **68**, 3, 034325 (2003).

Arrington, J., "Evidence for two-photon exchange contributions in electron-proton and positron-proton elastic scattering", Physical Review C **69**, 3, 032201 (2004).

Barkhuff, D., C. Armstrong, W. Bertozzi, J. Chen, D. Dale, G. Dodson, K. Dow, M. Epstein, M. Farkhondeh, J. Finn *et al.*, "Measurement of recoil proton polarizations in the electrodisintegration of deuterium by polarized electrons", Physics Letters B **470**, 1, 39–44 (1999).

Bartel, W., F.-W. Büsser, W.-R. Dix, R. Felst, D. Harms, H. Krehbiel, P. Kuhlmann, J. McElroy, J. Meyer and G. Weber, "Measurement of proton and neutron electromagnetic form factors at squared four-momentum transfers up to 3 $(\mathrm{GeV/c})^2$", Nuclear Physics B **58**, 2, 429–475 (1973).

Berger, C., V. Burkert, G. Knop, B. Langenbeck and K. Rith, "Electromagnetic form factors of the proton at squared four-momentum transfers between 10 and 50 fm^{-2}", Physics Letters B **35**, 1, 87–89 (1971).

Bernauer, J., V. Carassiti, G. Ciullo, B. Henderson, E. Ihloff, J. Kelsey, P. Lenisa, R. Milner, A. Schmidt and M. Statera, "The olympus internal hydrogen target", Nuclear Instruments and Methods in Physics Research Section A: Accelerators, Spectrometers, Detectors and Associated Equipment **755**, 20–27 (2014a).

Bernauer, J., J. Diefenbach, G. Elbakian, G. Gavrilov, N. Goerrissen, D. Hasell, B. Henderson, Y. Holler, G. Karyan, J. Ludwig *et al.*, "Measurement and tricubic interpolation of the magnetic field for the olympus experiment", Nuclear Instruments and Methods in Physics Research Section A: Accelerators, Spectrometers, Detectors and Associated Equipment **823**, 9–14 (2016).

Bernauer, J., M. Distler, J. Friedrich, T. Walcher, P. Achenbach, C. A. Gayoso, R. Böhm, D. Bosnar, L. Debenjak, L. Doria *et al.*, "Electric and magnetic form factors of the proton", Physical Review C **90**, 1, 015206 (2014b).

Bernauer, J. C., *Measurement of the elastic electron-proton cross section and separation of the electric and magnetic form factor in the Q 2 range from 0.004 to 1 (GeV/c) 2*, Ph.D. thesis, Johannes Gutenberg-Universität Mainz, Institut für Kernphysik, Diss (2010).

Blunden, P., W. Melnitchouk and J. Tjon, "Two-photon exchange and elastic electron-proton scattering", Physical review letters **91**, 14, 142304 (2003).

Blunden, P., W. Melnitchouk and J. Tjon, "Two-photon exchange in elastic electron-nucleon scattering", Physical Review C **72**, 3, 034612 (2005).

Borisyuk, D. and A. Kobushkin, "Box diagram in the elastic electron-proton scattering", Physical Review C **74**, 6, 065203 (2006).

Borkowski, F., P. Peuser, G. Simon, V. Walther and R. Wendling, "Electromagnetic form factors of the proton at low four-momentum transfer", Nuclear Physics A **222**, 2, 269–275 (1974).

Bosted, P., L. Andivahis, A. Lung, L. Stuart, J. Alster, R. Arnold, C. Chang, F. Dietrich, W. Dodge, R. Gearhart *et al.*, "Measurements of the electric and magnetic form factors of the proton from $Q^2 = 1.75$ to 8.83 $(\mathrm{GeV/c})^2$", Physical review letters **68**, 26, 3841 (1992).

Bouquet, B., D. Benaksas, B. Grossetete, B. Jean-Marie, G. Parrour, J. Poux and R. Tchapoutian, "Backward scattering of positrons and electrons on protons", Physics Letters B **26**, 3, 178–180 (1968).

Browman, A., F. Liu and C. Schaerf, "Positron-proton scattering", Physical Review Letters **12**, 7, 183 (1964).

Browman, A., F. Liu and C. Schaerf, "Positron-proton scattering", Physical Review **139**, 4B, B1079 (1965).

Bumiller, F., M. Croissiaux and R. Hofstadter, "Electron scattering from the proton", Physical Review Letters **5**, 6, 261 (1960).

Bystritskiy, Y. M., E. A. Kuraev and E. Tomasi-Gustafsson, "Structure function method applied to polarized and unpolarized electron-proton scattering: A solution of the G_{Ep}/G_{Mp} discrepancy", Phys. Rev. C **75**, 015207, URL `http://link.aps.org/doi/10.1103/PhysRevC.75.015207` (2007).

Chen, Y.-C., A. Afanasev, S. Brodsky, C. Carlson and M. Vanderhaeghen, "Partonic calculation of the two-photon exchange contribution to elastic electron-proton scattering at large momentum transfer", Physical review letters **93**, 12, 122301 (2004).

Chen, Y. C., C. W. Kao and S. N. Yang, "Is there model-independent evidence of the two-photon-exchange effect in the electron-proton elastic scattering cross section?", Physics Letters B **652**, 5, 269–274 (2007).

Christy, M., A. Ahmidouch, C. Armstrong, J. Arrington, R. Asaturyan, S. Avery, O. Baker, D. Beck, H. Blok, C. Bochna *et al.*, "Measurements of electron-proton elastic cross sections for $0.4 < Q^2 < 5.$ $(GeV/c)^2$", Physical Review C **70**, 1, 015206 (2004).

Chytracek, R., J. McCormick, W. Pokorski and G. Santin, "Geometry description markup language for physics simulation and analysis applications", IEEE Transactions on Nuclear Science **53**, 5, 2892–2896 (2006).

Coward, D. H., H. DeStaebler, R. Early, J. Litt, A. Minten, L. Mo, W. Panofsky, R. Taylor, M. Breidenbach, J. Friedman *et al.*, "Electron-proton elastic scattering at high momentum transfers", Physical Review Letters **20**, 6, 292 (1968).

Crawford, C. B., A. Sindile, T. Akdogan, R. Alarcon, W. Bertozzi, E. Booth, T. Botto, J. Calarco, B. Clasie, A. DeGrush *et al.*, "Measurement of the protons electric to magnetic form factor ratio from $^1\vec{H}(\vec{e}, ep)$", Physical review letters **98**, 5, 052301 (2007).

Dell'Orso, M. and L. Ristori, "A highly parallel algorithm for track finding", Nuclear Instruments and Methods in Physics Research Section A: Accelerators, Spectrometers, Detectors and Associated Equipment **287**, 3, 436–438 (1990).

Dombey, N., "Scattering of polarized leptons at high energy", Reviews of Modern Physics **41**, 1, 236 (1969).

Donnelly, T. W. and A. S. Raskin, "Considerations of polarization in inclusive electron scattering from nuclei", Annals of Physics **169**, 2, 247–351 (1986).

Epstein, C. S. and R. G. Milner, "Qed radiative corrections to low-energy møller and bhabha scattering", Phys. Rev. D **94**, 033004, URL `http://link.aps.org/doi/10.1103/PhysRevD.94.033004` (2016).

Ernst, F., R. Sachs and K. Wali, "Electromagnetic form factors of the nucleon", Physical Review **119**, 3, 1105 (1960).

Foldy, L., "The electromagnetic properties of dirac particles", Physical Review **87**, 5, 688 (1952).

Gayou, O., K. Aniol, T. Averett, F. Benmokhtar, W. Bertozzi, L. Bimbot, E. Brash, J. Calarco, C. Cavata, Z. Chai *et al.*, "Measurement of G_{Ep}/G_{Mp} in $\vec{e}p \rightarrow e\vec{p}$ to $Q^2 = 5.6$ GeV^2", Physical review letters **88**, 9, 092301 (2002).

Gorchtein, M., "Dispersive contributions to e^+p/e^-p cross section ratio in forward regime", Physics Letters B **644**, 5, 322–330 (2007).

Gramolin, A. and D. Nikolenko, "Reanalysis of rosenbluth measurements of the proton form factors", Physical Review C **93**, 5, 055201 (2016).

Guichon, P. A. and M. Vanderhaeghen, "How to reconcile the rosenbluth and the polarization transfer methods in the measurement of the proton form factors", Physical review letters **91**, 14, 142303 (2003).

Guttmann, J., N. Kivel, M. Meziane and M. Vanderhaeghen, "Determination of two-photon exchange amplitudes from elastic electron-proton scattering data", The European Physical Journal A **47**, 6, 1–5 (2011).

Hand, L., D. G. Miller and R. Wilson, "Electric and magnetic form factors of the nucleon", Reviews of Modern Physics **35**, 2, 335 (1963).

Hanson, K., J. Dunning Jr, M. Goitein, T. Kirk, L. Price and R. Wilson, "Large-angle quasielastic electron-deuteron scattering", Physical Review D **8**, 3, 753 (1973).

Hasell, D., T. Akdogan, R. Alarcon, W. Bertozzi, E. Booth, T. Botto, J. Calarco, B. Clasie, C. Crawford, A. DeGrush *et al.*, "The blast experiment", Nuclear Instruments and Methods in Physics Research Section A: Accelerators, Spectrometers, Detectors and Associated Equipment **603**, 3, 247–262 (2009).

Henderson, B., *A Precision Measurement of the e^+p/e^-p Elastic Scattering Cross Section Ratio at the OLYMPUS Experiment*, Ph.D. thesis, Massachusetts Institute of Technology (2016).

Hofstadter, R., "Electron scattering and nuclear structure", Reviews of Modern Physics **28**, 3, 214 (1956).

Hofstadter, R., F. Bumiller and M. Croissiaux, "Splitting of the proton form factors and diffraction in the proton", Physical Review Letters **5**, 6, 263 (1960).

Hofstadter, R., F. Bumiller and M. Yearian, "Electromagnetic structure of the proton and neutron", Reviews of Modern Physics **30**, 2, 482 (1958).

Hofstadter, R., H. Fechter and J. McIntyre, "High-energy electron scattering and nuclear structure determinations", Physical Review **92**, 4, 978 (1953a).

Hofstadter, R., H. Fechter and J. McIntyre, "Scattering of high-energy electrons and the method of nuclear recoil", Physical Review **91**, 2, 422 (1953b).

Hu, B., M. Jones, P. Ulmer, H. Arenhövel, O. Baker, W. Bertozzi, E. Brash, J. Calarco, J.-P. Chen, E. Chudakov *et al.*, "Polarization transfer in the $^2\mathrm{H}(\vec{\mathrm{e}},\mathrm{e}\vec{\mathrm{p}})\mathrm{n}$ reaction up to $\mathrm{Q}^2 = 1.61(\mathrm{GeV/c})^2$", Physical Review C **73**, 6, 064004 (2006).

Janssens, T., R. Hofstadter, E. Hughes and M. Yearian, "Proton form factors from elastic electron-proton scattering", Physical Review **142**, 4, 922 (1966).

JJ Murphy, I., Y. Shin and D. Skopik, "Proton form factor from 0.15 to 0.79 fm^{-2}", Physical Review C **9**, 6, 2125 (1974).

Jones, M., A. Aghalaryan, A. Ahmidouch, R. Asaturyan, F. Bloch, W. Boeglin, P. Bosted, C. Carasco, R. Carlini, J. Cha *et al.*, "Proton $\mathrm{G_E/G_M}$ from beam-target asymmetry", Physical Review C **74**, 3, 035201 (2006).

Jones, M. K., K. A. Aniol, F. Baker, J. Berthot, P. Bertin, W. Bertozzi, A. Besson, L. Bimbot, W. Boeglin, E. Brash *et al.*, "$\mathrm{G_{Ep}/G_{Mp}}$ ratio by polarization transfer in $\vec{\mathrm{e}}\mathrm{p} \rightarrow \mathrm{e}\vec{\mathrm{p}}$", Physical review letters **84**, 7, 1398 (2000).

Kelly, J., "Simple parametrization of nucleon form factors", Physical Review C **70**, 6, 068202 (2004).

Kelly, J. J., "Nucleon charge and magnetization densities from sachs form factors", Physical review C **66**, 6, 065203 (2002).

Kondratyuk, S., P. Blunden, W. Melnitchouk and J. Tjon, "Δ resonance contribution to two-photon exchange in electron-proton scattering", Physical review letters **95**, 17, 172503 (2005).

Litt, J., G. Buschhorn, D. Coward, H. Destaebler, L. W. Mo, R. E. Taylor, B. C. Barish, S. Loken, J. Pine, J. I. Friedman *et al.*, "Measurement of the ratio of the proton form factors, $\mathrm{G_E/G_M}$, at high momentum transfers and the question of scaling", Physics Letters B **31**, 1, 40–44 (1970).

MacLachlan, G., A. Aghalaryan, A. Ahmidouch, B. Anderson, R. Asaturyan, O. Baker, A. Baldwin, D. Barkhuff, H. Breuer, R. Carlini *et al.*, "The ratio of proton electromagnetic form factors via recoil polarimetry at $\mathrm{Q}^2 = 1.13\ (\mathrm{GeV/c})^2$", Nuclear Physics A **764**, 261–273 (2006).

Magboltz, C., "transport of electrons in gas mixtures computation program written by sf biagi", (2002).

Mar, J., B. C. Barish, J. Pine, D. H. Coward, H. DeStaebler, J. Litt, A. Minten, R. E. Taylor and M. Breidenbach, "Comparison of electron-proton and positron-proton elastic scattering at four-momentum transfers up to 5.0 $(\mathrm{GeV/c})^2$", Physical Review Letters **21**, 7, 482 (1968).

Maximon, L. and J. Tjon, "Radiative corrections to electron-proton scattering", Physical Review C **62**, 5, 054320 (2000).

McAllister, R. and R. Hofstadter, "Elastic scattering of 188-MeV electrons from the proton and the alpha particle", Physical Review **102**, 3, 851 (1956).

Meister, N. and D. Yennie, "Radiative corrections to high-energy scattering processes", Physical Review **130**, 3, 1210 (1963).

Milbrath, B., J. McIntyre, C. Armstrong, D. Barkhuff, W. Bertozzi, J. Chen, D. Dale, G. Dodson, K. Dow, M. Epstein *et al.*, "Comparison of polarization observables in electron scattering from the proton and deuteron", Physical review letters **80**, 3, 452 (1998).

Milner, R., D. Hasell, M. Kohl, U. Schneekloth, N. Akopov, R. Alarcon, V. Andreev, O. Ates, A. Avetisyan, D. Bayadilov *et al.*, "The olympus experiment", Nuclear Instruments and Methods in Physics Research Section A: Accelerators, Spectrometers, Detectors and Associated Equipment **741**, 1–17 (2014).

Mo, L. W. and Y.-S. Tsai, "Radiative corrections to elastic and inelastic ep and up scattering", Reviews of Modern Physics **41**, 1, 205 (1969).

Moteabbed, M., M. Niroula, B. A. Raue, L. B. Weinstein, D. Adikaram, J. Arrington, W. Brooks, J. Lachniet, D. Rimal, M. Ungaro *et al.*, "Demonstration of a novel technique to measure two-photon exchange effects in elastic e±p scattering", Physical Review C **88**, 2, 025210 (2013).

O'Connor, C., *The Contribution of Two Photon Exchange is Elastic Lepton-Proton Scattering*, Ph.D. thesis, Massachusetts Institute of Technology (2017).

Ohlsson, M., "Extensions and explorations of the elastic arms algorithm", Computer Physics Communications **77**, 1, 19–32 (1993).

Ohlsson, M., C. Peterson and A. L. Yuille, "Track finding with deformable templatesthe elastic arms approach", Computer Physics Communications **71**, 1, 77–98 (1992).

Pospischil, T., P. Bartsch, D. Baumann, R. Böhm, K. Bohinc, M. Ding, S. Derber, M. Distler, D. Elsner, I. Ewald *et al.*, "Measurement of G_{Ep}/G_{Mp} via polarization transfer at $Q^2 = 0.4$ $\mathrm{GeV/c^2}$", The European Physical Journal A-Hadrons and Nuclei **12**, 1, 125–127 (2001).

Price, L., J. Dunning Jr, M. Goitein, K. Hanson, T. Kirk and R. Wilson, "Backward-angle electron-proton elastic scattering and proton electromagnetic form factors", Physical Review D **4**, 1, 45 (1971).

Punjabi, V., C. F. Perdrisat, K. Aniol, F. Baker, J. Berthot, P. Bertin, W. Bertozzi, A. Besson, L. Bimbot, W. Boeglin *et al.*, "Proton elastic form factor ratios to $Q^2 = 3.5$ GeV^2 by polarization transfer", Physical Review C **71**, 5, 055202 (2005).

Qattan, I., J. Arrington, R. Segel, X. Zheng, K. Aniol, O. Baker, R. Beams, E. Brash, J. Calarco, A. Camsonne *et al.*, "Precision rosenbluth measurement of the proton elastic form factors", Physical review letters **94**, 14, 142301 (2005).

Rachek, I., J. Arrington, V. Dmitriev, V. V. Gauzshtein, R. Gerasimov, A. Gramolin, R. Holt, V. Kaminskiy, B. Lazarenko, S. Mishnev *et al.*, "Measurement of the two-photon exchange contribution to the elastic e±p scattering cross sections at the vepp-3 storage ring", Physical review letters **114**, 6, 062005 (2015).

Raskin, A. S. and T. W. Donnelly, "Polarization in coincidence electron scattering from nuclei", Annals of Physics **191**, 1, 78–142 (1989).

Rimal, D., D. Adikaram, B. Raue, L. Weinstein, J. Arrington, W. Brooks, M. Ungaro, K. Adhikari, Z. Akbar, S. A. Pereira *et al.*, "Measurement of two-photon exchange effect by comparing elastic $e^{\pm}p$ cross sections", arXiv preprint arXiv:1603.00315 (2016).

Rose, M., "The charge distribution in nuclei and the scattering of high energy electrons", Physical Review **73**, 4, 279 (1948).

Rosenbluth, M., "High energy elastic scattering of electrons on protons", Physical Review **79**, 4, 615 (1950).

Russell, R., *A Measurement of the Two-Photon Exchange Effect in Elastic Electron-Proton Scattering with OLYMPUS*, Ph.D. thesis, Massachusetts Institute of Technology (2016).

Schmidt, A., *Measuring the lepton sign asymmetry in elastic electron-proton scattering with OLYMPUS*, Ph.D. thesis, Massachusetts Institute of Technology (2016).

Sill, A., R. Arnold, P. E. Bosted, C. Chang, J. Gomez, A. Katramatou, C. J. Martoff, G. Petratos, A. Rahbar, S. Rock *et al.*, "Measurements of elastic electron-proton scattering at large momentum transfer", Physical Review D **48**, 1, 29 (1993).

Simon, G., C. Schmitt, F. Borkowski and V. Walther, "Absolute electron-proton cross sections at low momentum transfer measured with a high pressure gas target system", Nuclear Physics A **333**, 3, 381–391 (1980).

Steckelmacher, W., "Knudsen flow 75 years on: the current state of the art for flow of rarefied gases in tubes and systems", Reports on Progress in Physics **49**, 10, 1083 (1986).

Stern, O., R. Frisch and I. Estermann, "Magnetic moment of the proton", Nature **132**, 103 (1933).

Strauch, S., S. Dieterich, K. Aniol, J. Annand, O. Baker, W. Bertozzi, M. Boswell, E. Brash, Z. Chai, J.-P. Chen *et al.*, "Polarization transfer in the $^4\mathrm{He}(\vec{e},e\vec{p})^3\mathrm{H}$ reaction up to $Q^2 = 2.6$ $(\mathrm{GeV/c})^2$", Physical review letters **91**, 5, 052301 (2003).

Tomasi-Gustafsson, E. and G. Gakh, "Search for evidence of two-photon contribution in elastic electron-proton data", Physical Review C **72**, 1, 015209 (2005).

Tomasi-Gustafsson, E., M. Osipenko, E. Kuraev and Y. M. Bystritskiy, "Compilation and analysis of charge asymmetry measurements from electron and positron scattering on nucleon and nuclei", Physics of Atomic Nuclei **76**, 8, 937–946 (2013).

Veenhof, R. *et al.*, "Garfield, a drift chamber simulation program", in "Prepared for International Conference on Programming and Mathematical Methods for Solving Physical Problems, Dubna, Russia", pp. 14–19 (1993).

Walker, R., B. Filippone, J. Jourdan, R. Milner, R. McKeown, D. Potterveld, L. Andivahis, R. Arnold, D. Benton, P. Bosted *et al.*, "Measurements of the proton elastic form factors for $1 \leq Q^2 \leq 3$ $(\mathrm{GeV/c})^2$ at SLAC", Physical Review D **49**, 11, 5671 (1994).

Yennie, D., M. Levy and D. Ravenhall, "Electromagnetic structure of nucleons", Reviews of Modern Physics **29**, 1, 144 (1957).

Yount, D. and J. Pine, "Scattering of high-energy positrons from protons", Physical Review **128**, 4, 1842 (1962).

APPENDIX A

TABLE OF CROSS SECTION RESULTS

$\langle Q^2 \rangle$ $(\mathrm{GeV/c^2})^2$	ΔQ^2 $(\mathrm{GeV/c^2})^2$	$\langle \epsilon \rangle$	$\Delta\epsilon$	Ratio, $R_{2\gamma}$	Statistical Uncertainty (%)	Estimated Systematic Uncertainty (%)
0.625	0.05	0.897239	1.79448	0.987086	0.149536	1.5
0.675	0.05	0.886677	1.77335	0.987848	0.170832	1.5
0.725	0.05	0.875748	1.7515	0.99026	0.193219	1.5
0.775	0.05	0.864448	1.7289	0.990924	0.2173	1.5
0.825	0.05	0.852773	1.70555	0.989787	0.243009	1.5
0.875	0.05	0.840723	1.68145	0.987141	0.27097	1.5
0.925	0.05	0.828295	1.65659	0.990413	0.303551	1.5
0.975	0.05	0.815487	1.63097	0.989816	0.337548	1.5
1.025	0.05	0.802297	1.60459	0.989688	0.375946	1.5
1.075	0.05	0.788726	1.57745	0.990067	0.417937	1.5
1.125	0.05	0.774772	1.54954	0.990242	0.461016	1.5
1.175	0.05	0.760437	1.52087	0.988677	0.506287	1.5
1.25	0.1	0.738076	1.47615	0.986819	0.410787	1.5
1.35	0.1	0.707127	1.41425	0.994073	0.494151	1.5
1.45	0.1	0.67468	1.34936	0.99836	0.593266	1.5
1.575	0.15	0.631837	1.26367	0.991132	0.610642	1.5
1.725	0.15	0.57778	1.15556	0.991715	0.781503	1.5
1.875	0.15	0.520707	1.04141	0.999276	1.05036	1.5
2.05	0.2	0.450374	0.900749	0.990989	1.23592	1.5
2.25	0.2	0.366243	0.732486	1.01061	2.03246	1.5

Table A.1: The results for the cross section ratio as a function of Q^2 and ϵ.